# Nanoscale organic electronics: Experimental and theoretical studies on alkyl thiophene and rotaxane

*Kin-Yip Phoa*
*Vivek Subramanian*

Electrical Engineering and Computer Sciences
University of California at Berkeley

Technical Report No. UCB/EECS-2008-66

http://www.eecs.berkeley.edu/Pubs/TechRpts/2008/EECS-2008-66.html

May 21, 2008

# Nanoscale organic electronics:
# Experimental and theoretical studies on alkyl thiophene and rotaxane

by

Kinyip Phoa

B.S. (University of California, Los Angeles) 2003
M.S. (University of California, Berkeley) 2007

A dissertation submitted in partial satisfaction of the

requirements for the degree of

Doctor of Philosophy

in

Engineering-Electrical Engineering and Computer Sciences

in the

Graduate Division

of the

University of California, Berkeley

Committee in charge:

Professor Vivek Subramanian, Chair
Professor Tsu-Jae King Liu
Professor Steven G. Louie

Spring 2008

The dissertation of Kinyip Phoa is approved:

Chair ________________________________________________ Date ______________

________________________________________________ Date ______________

________________________________________________ Date ______________

University of California, Berkeley
Spring 2008

# Nanoscale organic electronics:

## Experimental and theoretical studies on alkyl thiophene and rotaxane

by

Kinyip Phoa

# Abstract

## Nanoscale organic electronics:

## Experimental and theoretical studies on alkyl thiophene and rotaxane

by

Kinyip Phoa

Doctor of Philosophy in Electrical Engineering and Computer Sciences

University of California, Berkeley

Professor Vivek Subramanian, Chair

As the end of the International Technology Roadmap for Semiconductors (ITRS) is approaching, supplements to the existing silicon technology are sought. Molecular electronics presents itself as one of the most promising candidates in terms of projected device dimensions. This thesis is devoted to advance the current technology towards the ultimate paradigm of single molecule transistors.

Firstly, we demonstrate field effect transistors with complete FET functionality formed within a self-assembled monolayer integrating both dielectric and semiconductor functionality within the same molecule. This is an attractive structure due to the potentially idealized characteristics that are achievable due to the intra-molecular semiconductor-dielectric interface. Grazing incidence X-ray diffraction (GIXD) is used to further study the morphology and the crystallinity of the monolayer deposited on different substrates. Furthermore, first-principle calculations are employed to

provide additional physical understanding of this system, as well as to model the monolayer. Initial demonstration of dielectric-integrated monolayer FETs is achieved based on the proposed monolayer system, albeit with poor characteristics.

Moreover, to complete the picture of nanoscale organic electronics, we investigate the feasibility of the [2]rotaxane molecular memory reported by Heath and Stoddart in 2002. In particular, its switching performance is probed theoretically through the evaluation and estimation of the energy landscape, the ionization potentials and the dielectric constants. However, it is found that the switching time of this molecule is greatly limited by an intrinsic “shuttling” reaction to merely 3.7μs under most conditions. Additionally, an alternative switching mechanism is proposed based on the new theoretical findings.

With the successful deciphering of the information hidden behind the GIXD and the lucrative enhancement in physical understanding of the [2]rotaxane molecule using first principles calculations, further effort is invested in exploiting this computational technique to predict candidate molecules that display desirable functionalities. Several halogenated acene molecules are expected to pack in the face-to-face motif, in contrast to the commonly observed herringbone packing motif. This is believed to enhance the mobility. Synthesis of these candidate molecules is underway to allow experimental verification, with the goal of dramatically improving device performance to fully exploit the idealized electrostatics of these structures.

# Acknowledgements

Within the five years of graduate student life in University of California, Berkeley, I owe my gratitude to a long list of people. I will start from my research advisor, Professor Vivek Subramanian. I still remember about 3 years ago, I talked to him about joining the group. Although I did not performed as well as expected in my first two years, he did not hesitate and courteously let me start working in his lab right away. This began the route leading to this thesis work. Throughout these 3 years, he guided me through the qualifying exam and various research struggles with his supporting spirit and vast knowledge.

Another person who helped me tremendously throughout my graduate work is Dr. Jeff Neaton. I can fairly say that Dr. Neaton served as my informal advisor in the last two years. I approached him seeking for advices on performing first principles study on the switching performance of the [2]rotaxane molecule. Although I did not have any prior experience in theoretical study, with his resourceful guidance and tolerance of my repeating questions, I have learnt the basics. A large portion of this thesis is consisted of the topics I worked on within this collaboration.

I would like to devote another paragraph thanking the two people I worked extensively with. Dr. Kanan Puntambekar was a postdoc joining with an expertise in AFM and GIXD characterization. She initially led the project and had come up with plenty of interesting ideas. She also characterized the monolayer we used in the DI-mFET with GIXD through the collaboration with Dr. Mike Toney from Stanford Synchrotron Radiation Laboratory (SSRL). The modeling of that monolayer under the constraints of the GIXD data ended up forming a chapter in this thesis, as well as the precursor to another chapter. However, all these wonderful work would not have been possible if Clayton Mauldin, our collaborator in Professor Frechet's group in the Department of Chemistry, had not made all the fantastic molecules for us. At this moment, Clayton and I are still working closely on the unfinished projects.

In general, I thank all members in the organics electronics (or printed electronics) group. These wonderful people are Paul Chang, Dave Redinger, Steve Molesa, Brian Mattis, Josie Chang, Qintao Zhang, Alejandro de la Fuente, Daniel Huang, Frank Liao, Dan Soltman, Shong Yin, Tim Bakhishev, Lakshmi Jagannathan, Michael Tseng. And then there are the staffs, undergraduate students and visiting scholars: Steve Volkman, Ben Weil, Tiffany Cheng, and James Ding. Brian, Alejandro, Dan H., Tim and Steve V. had helped me very much to ramp up in my early days in this group. Also, the fun football time during the last 3 summers were memorable (and thanks for knocking me down purposely, Vivek).

Another group of people I would like to acknowledge is the device group member working in 373 Cory, especially Hei Kam, Cheuk Chi Lo, Yu-Chih Tseng, Drew Carlson, and Pankaj Kalra. They are my good friends, peers and mentors. I enjoyed talking, playing, taking classes and learning with them. They have been supporting me since my day one in UC Berkeley. Other device group members that I would like to thank include Shiying Xiong, Hiu-Yung Wong, Sriram Balasubramanian, Kyoungsub Shin, Vidya Varadarajan, Chung-Hsun Lin, Dan Good, Blake Lin, Marie-ange Eyoum, Mohan Dunga, Alvaro Padilla, Joanna Lai, Donovan Lee, Anupama Bowonder, Pratik Patel, Darsen Lu, Dave Carlton, Hideki Takeuchi, Yuri Yasuda-Masuoka, Koichi Fukuda, Akira Hokazono, Takuro Matsutoya, Woo-Young Choi, and Nathan Emley.

In addition, I would like to thanks the staff in Cory Hall, in particular, Ruth Gjerde, Charlotte Jones, Linda Manly, Sia Parsa, Joe Donnelly, Xiaofan Meng, Kim Chan, Jimmy Chang and many other who had helped me on various aspects over the last 5 years.

Lastly, I thank Professor Tsu-Jae King Liu (chair), Professor Vivek Subramanian, Professor Andrew R. Neurether and Professor Steven G. Louie for being in my qualifying exam committee. I appreciate the insightful comments and suggestions they made during the exam, and also during their edition of my master thesis and this Ph.D. thesis.

Kinyip Phoa, Ph.D. Candidate

University of California, Berkeley

May 22, 2008

# Table of Contents

# List of Figures

## Chapter 1 – Introduction

## Chapter 2 – Introduction

## Chapter 3 – Characterization of alkyl-thiophene monolayer

## Chapter 4 – Theoretical study of [2]rotaxane

## Chapter 5 – Molecular engineering

## Chapter 6 – Recommended future work and conclusions

# List of Tables

# Chapter 1

# Introduction

As the end of the International Technology Roadmap for Semiconductors (ITRS) is approaching, in conjunction with the exploration of advanced transistor structures, supplements to traditional field effect transistors (FET) are being intensely sought. Holding the promise of the smallest transistor possible [1, 2], molecular electronics is one of the many promising candidates outlined in the “Emerging Research Devices” section of the ITRS and will be investigated in depth in this thesis.

On the other hand, as a low-cost alternative to silicon-based FETs, organic semiconductors are gaining increasing interest for their properties and performance, and are being developed for practical commercial products in printed radio frequency identification (RFID) tags and bio-chemical sensors. This thesis will also discuss the work on systematic design of molecules with enhanced electronic performance. Before delving into the core of this thesis, brief introductions on the topics related to this thesis and the techniques employed are given.

## 1.1 Organic transistors

The field of organic electronics has flourished as synthetic chemistry progresses forward. Liquid crystals, invented in the 19th century and first demonstrated as display materials in the 1960s, are now ubiquitous. Organic light emitting diodes (OLEDs), which promise to enhance the visual quality of the future displays, are also at the verge of commercialization. Also, having been investigated intensively for over two decades after the first reported demonstration [3], organic thin film transistors (OTFT) are on par with the widely applied amorphous silicon ($\alpha$-Si) thin film transistors (TFT) in terms of performance at present. The definition of a suitable low-cost large-area application will entail the success of this exciting technology.

In the meantime, OTFTs have continued to be studied to approach the molecular limit. The demonstration of the first monolayer transistor by Chang et al. [4] has sprung up interest in its next incarnation, the dielectric integrated monolayer FET (DI-mFET), which will be discussed in detail in chapter 2. This section discusses the progresses made through the decades of research and the widely accepted transport models of the organic semiconductors.

### 1.1.1 Organic thin film transistors (OTFTs)

Organic materials have been playing a crucial role in the exploding advances in the silicon industry. Being photosensitive, photoresists have enabled the shrinking of the critical dimension down to the submicron regime, together with other breakthroughs in photolithography. Additionally, low-cost polymeric materials like epoxy have allowed reliable packaging of semiconductor chips. Aside from these assisting roles, intense research efforts in academia and industrial research laboratories in the 1970s and early 1980s on active semiconducting organic materials finally bore fruit in the late 1980s when Koezuka et al. demonstrated the first organic thin film transistor (OTFT) [3]. Although the calculated mobility was merely $10^{-5}cm^2/Vs$, over the last twenty years of diligent work, a 5-order of magnitude increase in the mobility has been achieved. Mobilities on the order of $1cm^2/Vs$ are now commonly reported. This subsection will briefly outline the exciting progress made in the last two decades. [5, 6, 7] are excellent reviews on this technology.

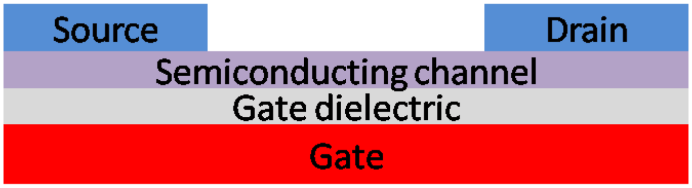

Figure 1.1, schematic of a bottom-gated top-contacted OTFT

To appreciate the hurdles that have been overcome, it is essential to understand how an OTFT operates. A cross-sectional schematic of a bottom-gated top-contacted OTFT is shown in figure 1.1, where the source/drain electrodes are in contact with the organic semiconducting channel while the gate electrode is separated from the channel by a thin gate dielectric. When the gate is sufficiently negatively biased, positive mobile charge carriers, holes, are induced along the semiconductor/dielectric interface, filling up the trap states and forming a conducting channel connecting the source/drain electrodes. This is the on-state. When a gate bias larger (less negative or more positive) than the threshold voltage is applied, a conducting channel is not formed; thus corresponds to the off-state. The transport mechanism in organic thin film will soon be covered below.

As mentioned above, the first demonstrated OTFT suffered from a low mobility of $10^{-5}$cm$^2$/Vs, which was an intrinsic property of the polythiophene [3]. Throughout the years, researchers migrated away from amorphous films [8] to micropolycrystalline poly(3-hexylthiophene) (P3HT) films [9]. Noticeable improvement in terms of mobility was attained through the formation of anisotropic lamellar microstructure with strong $\pi$-$\pi$ inter-chain interactions in these P3HT films. Furthermore, to facilitate low-cost printing fabrication, solution processable organic semiconductors like pentacene precursor were developed. At the same time, the mobilities of these OTFTs were among the highest reported, reaching 0.1 – 1cm$^2$/Vs. To facilitate further improvements, efforts were made to modify the side groups of different organic semiconductors. Being a modified tetracene with four benzene rings attached as side groups, rubrene stood out to be an exceptional organic semiconductor with the highest mobility, 10cm$^2$/Vs, reported to date [10]. However, the lack of a thin-film phase of this fantastic material to process into an OTFT hindered its applicability. Figure 1.2, after [5], displays the progress made since the first OTFT demonstration through 2000.

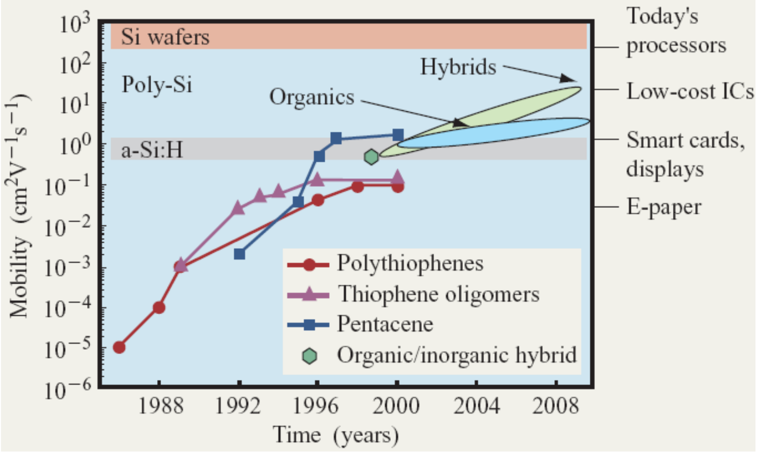

Figure 1.2, performance of various organic semiconductors over time, after [2].

Besides the active semiconducting material, the gate dielectric in the OTFT also critically affects the performance. As $I_D \propto C_{ox}$, researchers attempted to boost the capacitance of the gate dielectric by using silicon dioxide directly thermally grown on silicon substrate or even metal oxide, including high-k dielectrics like $Ta_2O_5$, deposited either by chemical vapor deposition (CVD), sputtering or anodization. High mobilities and large on/off ratios were achieved [11, 12]. However, considering that all-printed OTFT on low-cost substrates is the ultimate goal, the use of metal oxides having melting points that are much higher than most of the substrate materials, is hard to be justified. More importantly, as the surfaces of metal oxides are mostly hydrophilic, the hydrophobic nature of the organic semiconductors to be deposited, either by spin-casting or printing, would result in a poorly formed thin film. Surface treatment with hexamethyldisiloxane (HMDS) or octadecyltrichlorosilane (OTS) was widely employed to improve the quality of the thin film [13]. As an alternative, solution processable organic dielectrics were used and comparable performance to devices with inorganic dielectrics was achieved. Notable recent work includes references [14, 15, 16]. Organic dielectrics further extended from the form of thin film to self-assembled monolayer (SAM). The advantages of using SAM as a dielectric include comparable smoothness to the underlying substrate and well-defined dielectric thickness. The operating voltage of the OTFT could also be reduced as the capacitance from the SAM dielectric increased. OTS and various multi-layer SAM were employed in [17, 18]. Yet, significant gate leakage current and reproducibility plagued this exciting innovation.

As the performance of the organic semiconductor improves, contact resistance effects become more pronounced. The effects from contacts are noticeable in the concavities of the $I_D V_D$ curves in the linear region, which are characteristics of contact barriers. The energy band diagram in figure 1.3 reveals the origin of this contact barrier when the source/drain electrodes are made of metals like titanium. This also unveils the p-FET nature of most of the OTFTs as the work function of the source/drain electrodes are closer to the highest occupied molecular orbital (HOMO) that allows efficient hole injection. Figure 1.3 also shows that gold aligns well with the HOMO of pentacene and thus results in significantly lower contact resistance.

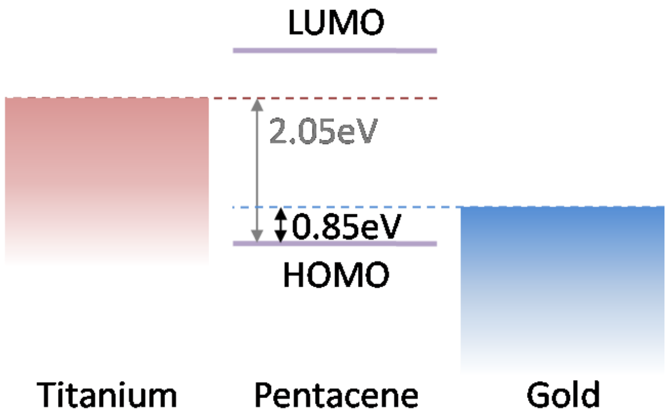

Figure 1.3, energy band diagram revealing the origin of the contact resistance between the metal source/drain electrodes to the organic semiconductor channel.

Furthermore, the effect of the thickness of the organic semiconductor layer on the current-voltage (I-V) characteristics has been explored. As in silicon FETs, the conducting layer in the channel is only the first few nanometers from the semiconductor/dielectric interface, which is essentially the first layer of the deposited thin film [6]. The rest of the deposited film adversely contributes to the on/off ratio as it provides leakage path for the off-state current. Additionally, thicker films translate to more total traps and therefore a stronger bias stress effect is observed [19]. With all these undesirable effects, researchers strive to thin down the semiconducting layer. Scaling down to the ultimate limit, Chang et al. demonstrated the first monolayer FET [4]. This carries the discussion over to the next subsection.

### 1.1.2 Monolayer and molecular transistors

The adverse consequences of large off-state leakage current and strong bias stress effect due to thick semiconductor films are the major motivations to investigate into monolayer transistors. Figure 1.4 contrasts the subthreshold region of the $I_DV_G$ between conventional OTFTs and a monolayer transistor [20]. An immediate observation would be the 2-order of magnitude reduction in off-state current in the latter measurement. Reference [20], in addition, showed the insignificance of the bias-stress effect on the monolayer transistors.

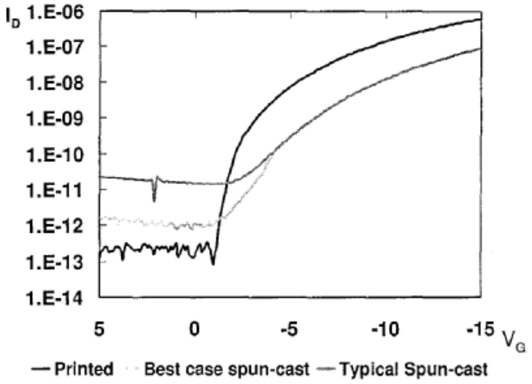

Figure 1.4, subthreshold region of the $I_DV_G$ of conventional OTFTs and a monolayer transistor, after reference [20]. The legend “Printed” refers to the monolayer transistor while “Spun-cast” refers to conventional OTFT.

By shrinking the length of a monolayer transistor down to the limit of a single molecule, one would realize a single molecule transistor. Molecular devices were first envisioned by Aviram and Ratner in the 1960s [21]. Since then, many reports followed on proposing new devices [22] and many argued the feasibility [23]. Recently, researchers began to probe the carrier transport through single molecules via different techniques, including AFM and break-junctions [24, 25]. Collaborating with theorists, Venkataraman et al. reported trends of reduction in current through alkanes as the length of the molecule increased [25].

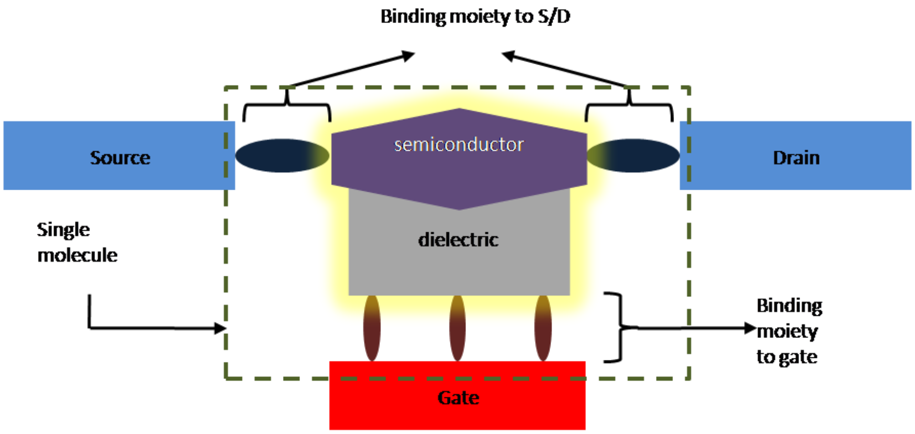

Figure 1.5, schematic of an idealized single molecule transistor, where the components enclosed by the dashed box, the semiconductor, the dielectric and the binding moieties, make up a single molecule bridging the source, drain and gate contacts.

Although these were exciting findings and confirmations, the realization of a molecular transistor is still formidable. Figure 1.5 presents a schematic of an idealized molecular transistor. From the chemists' bottom-up point of view, large molecules are difficult to synthesize; on the other hand, from the engineers' top-down standpoint, it would be an arduous task to fabricate structures smaller than 10nm due to current lithographical limits. As a result, transistors made of a single molecule have not been reported to date, except for carbon nanotube FETs [26]. The monolayer transistor then positions itself as an intermediate step towards the paradigm of single molecule transistors for both chemists and engineers since challenging but reachable molecules and structures are involved. With the successful demonstration of the first monolayer transistor, the next sensible step forward was integrating a dielectric layer within the semiconducting molecule, as shown in figure 1.5. Chapter 2 and 3 will mainly focus on this particular topic.

### 1.1.3 Transport in organic semiconductors

While the band transport model is a commonly adopted transport model in inorganic solid-state crystals, it is widely accepted that variable-range hopping (VRH) and multiple trapping and release (MTR) are the dominant transport mechanisms in organic semiconductors. The lack of both the delocalization of the wavefunctions of the charge carriers in real space and the long range periodicity in organic semiconductors makes band transport model inapplicable to describe these systems.

Within the band transport model, a charge carrier travels through the crystal as if it were traveling in free space, with a modified effective mass, m*,

$$m^* = \frac{\hbar^2}{\delta^2 E/\delta k^2} \qquad \text{(Eq 1.1)}$$

accounting for the periodic crystal potential, until it encounters imperfection in the crystal at which point it would scatter. The imperfections in this context include crystal defects, impurities, lattice vibrations and any perturbations from the perfectly periodic crystal itself. The electrical conductivity, σ, of a material is then given by

$$\sigma = \frac{q^2 n \tau}{m^*} \qquad \text{(Eq 1.2)}$$

where q is the charge of an electron, n is the carrier density and $\tau$ is the mean free time, defined as the time the charge carrier travels freely between scattering events.

On the contrary, similar to $\alpha$-Si TFT, the channels of OTFTs are mostly amorphous or nanocrystalline. Developed to treat poorly ordered and amorphous organic semiconductor film, VRH models hopping between sites. Based on the mutual coupling between localized states, Ambegaokar et al. derived the hopping rate, $\Gamma_{\mathrm{ij}}^{0}$, as

$$\Gamma_{\mathrm{ij}}^{0} \propto \exp\left[-2\alpha R_{ij} - \frac{\left(|E_i|+|E_j|+|E_i-E_j|\right)}{2kT}\right] \qquad \text{(Eq 1.3)}$$

where the first term in the exponent represents the tunneling process, that depends on the wavefunction overlap factor, $\alpha$, and the second term represents the transition between two energy levels, $E_i$ and $E_j$, with reference to the Fermi level [27]. The pioneering work in references [27] assumed a constant density of state (DOS) and predicted the temperature dependence of the conductivity, $\sigma(T)$, to be of the form

$$\sigma(T) \propto exp\left[-(T/T_0)^{1/n}\right] \qquad \text{(Eq 1.4)}$$

However, in organic semiconductors, there exist exponential band tails. Significant deviation from equation 1.4 can be observed and $\sigma(\delta, T)$ is derived to be

$$\sigma(\delta, T) \propto \left[\frac{\pi N_t \delta (T_0/T)^3}{(2\alpha)^3 B_c \Gamma(1-T/T_0)\Gamma(1+T/T_0)}\right]^{T_0/T} \qquad \text{(Eq 1.5)}$$

where $\delta$ is the occupation [28]. Analytically, this formula resembles the Arrhenius relation,

$$\sigma \propto e^{-E_a/kT} \qquad \text{(Eq 1.8)}$$

One can then interpret that charge carriers are thermally activated to a transport level [29]. The carrier transport in organic semiconductors, for example, pentacene, was well-modeled under this formalism [30].

Originally developed for $\alpha$-Si [31] and later employed to describe transport in relatively well-ordered organic semiconductors [32], MTR differs from VRH in that a band transport flavor is mixed together with the hopping mechanism. In MTR, charge carriers are assumed to be trapped in a localized state, thermally released to some extended states where carriers enjoy band transport before being trapped in another localized state. The thermal activation process in this framework lent a Arrhenius relation to the mobility, $\mu$,

$$\mu \propto e^{-(E_c - E)/kT} \quad \text{(Eq 1.9)}$$

In general, the MTR model describes high mobility materials better than VRH, while VRH works better for the low mobility ones.

As the applied voltage increases, before reaching the contact limited current regime, the ohmic current transitions into space charge limited current (SCLC). In this regime, the charge carrier required to sustain an ohmic current is far beyond the available carriers, resulting in increased differential resistance.

Qualitatively, the above mathematical framework can be expressed in terms of the packing structure and the molecular orbitals of the organic semiconductors. Figure 1.6 shows (a) the face-to-face (f2f) and (b) the edge-to-face (e2f) packing motifs and some hypothetical molecular orbitals of the respective structures. According to both the VRH and MTR models, carriers jump from one available site to another in real space.

Hence, the stronger π-orbital interactions in the f2f packing structure are believed to lead to higher carrier mobilities.

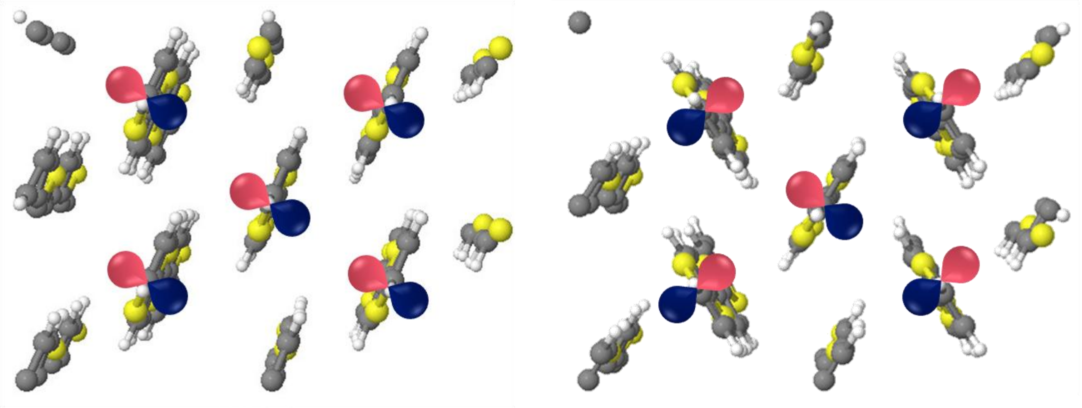

Figure 1.6, (a) face-to-face (f2f) and (b) edge-to-face (e2f) packing structures and their hypothetical molecular orbitals.

## 1.2 Molecular memory

It is the combination of logic and memory that makes powerful computers possible today. In the previous section, transistors, the fundamental building blocks of logic, have been introduced in detail. The background of molecular memory will now be discussed.

The type of the molecule used in Heath and Stoddart's seminal demonstration of [2]rotaxane as molecular memory in Luo et al. [33] consisted of two mechanically interlocking molecular structures, as shown in figure 1.7. These special molecules were first synthesized by Wasserman [34] as catenane (Latin: *catena*, chain) and by Harrison [35] as rotaxane (Latin: *rota*, wheel; *axis*, axle). These names figuratively described catenane as two interlocking rings (figure 1.7a) and rotaxane as a ring interlocked with a backbone (figure 1.7b, c and d). Since then, there were multiple reports discussing the synthesis details of these molecules [36, 37]. It was not until the early 1990s that researchers started realizing the mechanical shuttling of the ring [38, 39, 40, 41] as a form of molecular machine.

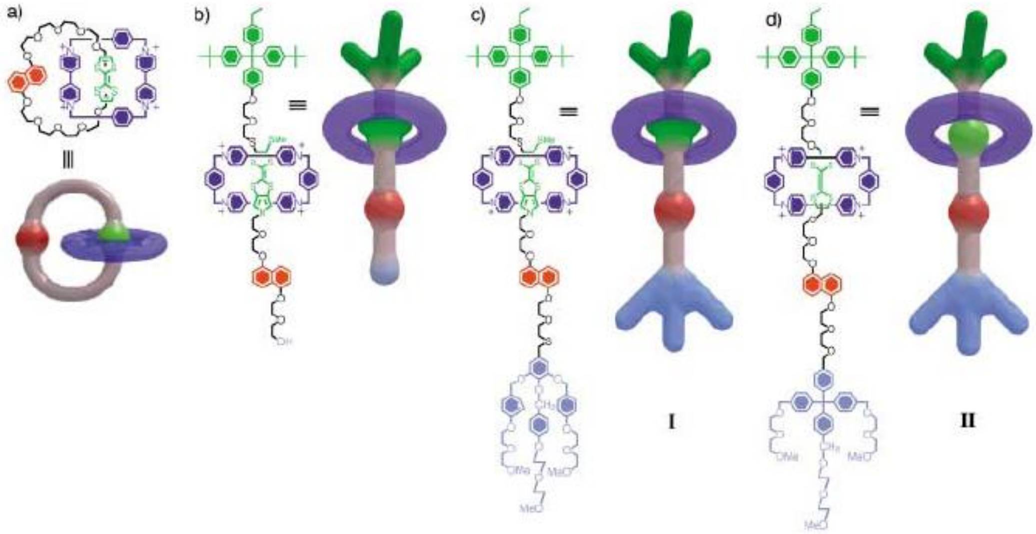

Figure 1.7, cartoon representations of a) a bistable [2]catenane, b) an amphiphilic, bistable [2]pseudorotaxane, c) and d) two versions of amphiphilic bistable [2]rotaxane, as molecular mechanical, after [33].

Stoddart and the co-workers perfected the synthesis of bistable catenanes and rotaxanes that could be switched electrochemically [42]. Furthermore, the same group demonstrated catenane-based electronically reconfigurable switches in 2000 [43]. These eventually led to the molecular memory device based on monolayer of [2]rotaxane [33]. Recently a 160k-bit molecular memory circuit at a density of 100G-bit/cm$^2$ was fabricated [44], although only with poor yield.

A series of experiments, accompanied by theoretical studies, were then performed to gain understanding and insight into the switching mechanism as well as to verify the experimental findings. It was revealed that the switching properties of the

[2]rotaxane molecules were significantly affected by their environment: in solution, in polymer, and as a monolayer [45, 46]. Direct structural evidence of the shuttling of the ring was provided by an X-ray reflectometry study where X-rays were incident onto amphiphilic, bistable [2]rotaxane air/water interface and the reflected beam provided electron density information [47]. DeIonno et al. employed infrared spectroscopy to verify that thermal evaporation of titanium onto monolayers of [2]rotaxane would not induce damage to the functional parts of the molecules, although the optimum surface density for switching deduced from this report was questionable [48]. Furthermore, initial first principles calculation studies were done on [2]rotaxane to rationalize the experimentally observed switching, to provide the electronic structure of the molecule and to further hint possible improvements on the molecular design [49]. This was followed by two molecular dynamics simulations of how the [2]rotaxane molecules assembled on air/water interfaces for Langmuir-Blodgett (LB) film deposition and on gold (111) surfaces for actual device fabrication [50, 51]. Lastly, Jang YH et al. attempted to confirm the proposed switching mechanism of

$$TTF \rightarrow TTF^{+} \rightarrow CBPQT^{4+}\text{ring shuttle } \rightarrow TTF^{2+}$$

with density functional theory (DFT) [52]. A comprehensive review on the current status of research on rotaxane was provided by Dichtel et al. [53].

In spite of the wide range of experiments and calculations performed by various researchers, there were still unanswered questions regarding the switching of the demonstrated memory devices, both experimentally and theoretically. For example, the entitlements of the [2]rotaxane memory in terms of switching performance and long term endurance had not been explored. Moreover, as the energy landscape of the ring shuttling reaction had not been mapped out, the mechanism leading to the switching is still unclear. This thesis attempts to address some of these concerns.

## 1.3 X-ray diffraction

In this thesis, X-ray diffraction is employed to study the monolayers used in the FETs to be described in chapter 2. As discussed above, crystallinity is tightly associated with the carrier transport and hence the performance of the fabricated device. X-ray diffraction is the perfect characterization technique to extract the rich information about the crystal structure of the studied subject through the diffraction patterns. William H. Bragg and William L. Bragg were awarded the Nobel Prize in physics "for their services in the analysis of crystal structure by means of X-rays" [54]. Fundamental theoretical background of X-ray diffraction is given first and the particulars about grazing incidence X-ray diffraction (GIXD) will then be outlined in this section.

### 1.3.1 Theoretical background of X-ray diffraction

X-ray diffraction patterns contain rich information about the materials being studied and there are many subtleties that cannot be summarized in just a few pages. As deciphering an X-ray diffraction pattern is a field of science by itself, many authors have written excellent reviews and books on this subject. Chapter 5 of reference [55] is recommended for motivated readers. In this subsection, only the basics will be discussed.

Perhaps the most intuitive way of understanding the bright spots and dark regions in a diffraction pattern is the famous Bragg's law, which mathematically can be written as

$$2d\sin\theta = n\lambda \qquad \text{(Eq 1.10)}$$

where n is an integer. Suppose the inter-planar distance between two layers of atoms is d, and the wavelength of the incident X-ray is $\lambda$, if the above condition is met, a constructive interference will result in a bright spot in the diffraction pattern. The entire field of X-ray diffraction is built upon this equation.

While the Bragg's law in its "2d sin$\theta$ = n$\lambda$" form is as elegant as it is, it can be difficult to use to analyze diffraction pattern from compounds where more than one atomic species are present. An alternative is to portray a diffraction pattern as a sum of wavelets from atoms. As the incident X-ray is scattered from an atom, a phase factor is added. A constructive interference will result if the scattered waves with these different phase factors add to one another. Mathematically, the scattered wave can be written as

$$\psi(\mathbf{k}) = \sum_{j=1}^{N} f_j e^{-i\mathbf{k}\cdot\mathbf{r_j}} \qquad \text{(Eq 1.11)}$$

where $f_j$ is the atomic form factor. Ideally, the brightness of the spots in a diffraction pattern is the intensity of the scattered wave, which is proportional to the square of the amplitude,

$$I(\mathbf{k},\mathbf{r}) \propto |\psi(\mathbf{k})|^2 \qquad \text{(Eq 1.12)}$$

And the proportionality constant includes Lorentz factor, polarization factor and several other correction factors. The discussion on these secondary effects will be skipped in this thesis, but they are well-covered in the recommended reading.

One should readily notice that the picture of the diffraction pattern as a sum of wavelets from atoms is no different from a discrete Fourier transform of the atomic coordinates in a primitive unit cell, weighted by the atomic form factors. This bears close resemblance to the analysis in Fourier optics, where the diffraction pattern from a plane wave through an aperture is the Fourier transform of the aperture itself. In an X-ray diffraction experiment, the incident X-ray is the “plane wave” and the crystal is the “aperture”. Therefore, there should be no surprise that an X-ray diffraction experiment is capturing the unique fingerprint of the sample in its reciprocal lattice form.

### 1.3.2 Grazing incidence X-ray diffraction (GIXD)

Due to the special circumstances of the samples studied in this thesis, GIXD, instead of conventional X-ray diffraction, was used. In the above discussion, the terms materials, samples and crystals are loosely used without proper definitions, and are referring to a perfect bulk crystal of infinite size in general. However, the effect of the crystallite size is important in understanding the rationale behind this technique and thus will be summarized here.

Consider the picture of Bragg’s law again. It is obvious that with an infinite number of layers of atoms, the diffraction pattern should have infinitely sharp peaks, just as predicted by the discrete Fourier transform of the primitive unit cell. However, when the number of layers decreases, more $\theta$ will satisfy the Bragg's law. This means that the peaks are broadened. As the number of layers approaches one, there will no longer be any constructive or destructive interferences, and hence no bright spots or dark regions in a diffraction pattern. This crystallite size broadening effect is well-known and can be captured as a one of the proportional constants in equation 1.12

$$I(s) = I_x(s_x)I_y(s_y)I_z(s_z) \qquad \text{(Eq 1.13)}$$

Each term corresponds to the size effect along that direction and they share the same functional form as

$$I_i(s_i) = \frac{\sin^2(\pi N_i a_i s_i)}{\sin^2(\pi a_i s_i)} \qquad \text{(Eq 1.14)}$$

where $a_i$ is the inter-planar spacing and $N_i$ is the number of planes in the crystal along the i direction.

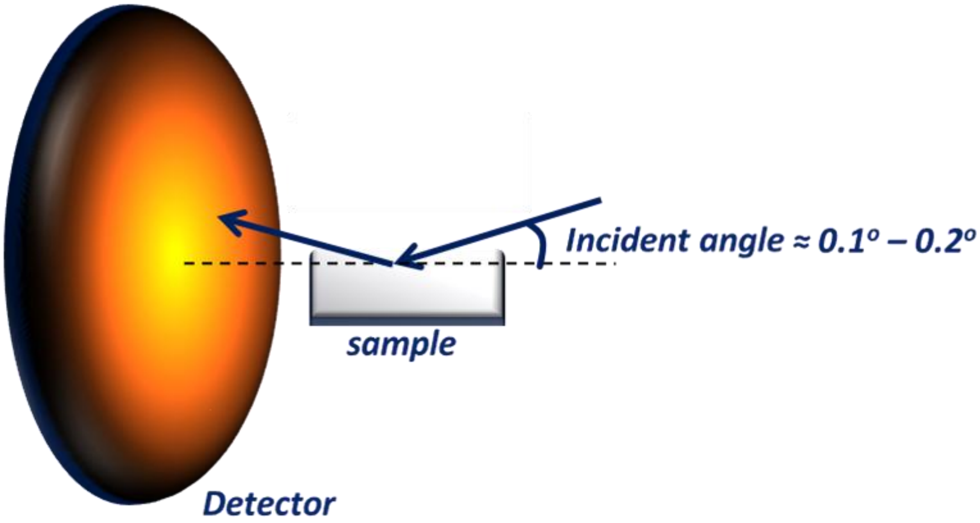

Figure 1.8, schematic of the setup of GIXD.

Knowing this fact, it should be obvious that conventional X-ray diffraction technique would yield very broad peaks, if any at all, when characterizing very thin films.

To circumvent this problem, incident X-rays at a very shallow angle are called for, maximizing the number of planes that the incident beam is diffracted from. This special kind of X-ray diffraction is called grazing incidence X-ray diffraction. A schematic of the setup is shown in Figure 1.8.

## 1.4 First principles calculations

In this thesis, computational experiments are extensively employed to supplement and to shed light on the physical experimental observations. The theoretical framework of the careful studies was formed by ab-initio total energy calculations based on quantum mechanics, which have been broadly applied to various other topics, from silicon [56] to carbon nanotubes [57]. In this subsection, a brief discussion on this method is presented to introduce the relevant terminologies that will be found in this thesis. Interested readers are referred to [58] and chapter 5 and 6 of reference [59] for detailed reviews on this technique.

As most of the physical properties of any given system can be related to its total energy or the differences between the total energies, the total energy is arguably the most important property to be computed. For example, lattice constant can be determined by inputting various possible lattice constant and finding the minimum in the calculated total energy. Indeed, all of the systems studied in this thesis have first gone through the so-called ion relaxation to attain their minimum equilibrium energies before further analysis are performed to ensure that the subjects are at their relaxed states. However, such a powerful technique comes at the cost of computational effort.

The size of the systems being studied had been limited to below 100 atoms until the recent advances in computer empowered by the famous Moore's Law.

The starting point of solving for the total energy of a system is the Schrodinger equation which models the physical world with quantum mechanics. References [60, 61] are both recommended textbooks for quantum mechanics. It is well-known that analytical solutions to the Schrodinger equation only exist for hydrogen and helium atom and only numerical solutions are available to any systems that are slightly more complex. A major difficulty in these problems is that the exact functional form of the exchange-correlation energy for many-electron interaction does not exist. Many different approaches are taken by famous physicists to obtain approximate solutions. Two widely applied methods, Hartree-Fock (HF) method and density functional theory (DFT), are discussed and contrasted.

The Hartree-Fock method can be viewed as a variational method in which the wavefunction, $\psi_k$, of a many-electron system is expressed in the form of a Slater determinant, which is an anti-symmetrized product of a one-electron wavefunction that accounts for the fermionic nature of the electrons. In this context, the Schrodinger equation is written as the Hartree-Fock equations. The Hamiltonian is expressed in the form of a Fock operator, $\mathcal{F}$,

$$\mathcal{F}\psi_k = \epsilon_k \psi_k \qquad \text{(Eq 1.15)}$$

with

$$\begin{aligned}\mathcal{F}\psi_k = &\left[-\frac{1}{2}\nabla^2 - \sum_n \frac{Z_n}{|\mathbf{r}-\mathbf{R_n}|}\right]\psi_k(\mathbf{r}) \\ &+\sum_{l=1}^{N}\int d\mathbf{r}'\,|\psi_l(\mathbf{r}')|^2\frac{1}{|\mathbf{r}-\mathbf{r}'|}\psi_k(\mathbf{r}) \\ &-\sum_{l=1}^{N}\int d\mathbf{r}'\,\psi_l^*(\mathbf{r}')\frac{1}{|\mathbf{r}-\mathbf{r}'|}\psi_k(\mathbf{r}')\psi_l(\mathbf{r}) \qquad \text{(Eq 1.16)}\end{aligned}$$

where the first three terms in equation 1.16 are the kinetic energy operator of the electrons, the electron-ion interactions, and the electron-electron interactions in a mean-field flavor, respectively, and the last term accounts for the exchange energy arising from the Pauli exclusion principle. As one can notice, $\mathcal{F}$ depends on $\psi_k$ and therefore the Hartree-Fock equations must be solved self-consistently by 1) constructing a Fock operator from an initial guess, 2) diagonalizing the Fock operator to yield a new Slater determinant, and 3) iterating the procedure with the new guess if self-consistency is not reached. At the end of the self-consistent iteration, the Slater determinant would correspond to the electronic wavefunction of the system being studied. Although being an elegant approach to solve the formidable Schrodinger equation, the HF method obviously lacks the inclusion of the correlation energy, leading to an over-estimation in the calculated total energy.

The second approach to be outlined is the density functional theory (DFT) introduced in the seminal work by Hohenberg and Kohn [62], and Kohn and Sham [63]. The Hohenberg and Kohn theorems state that 1) there is a one-to-one relationship between the ground state electron density and the external potential, and 2) the ground state electron density minimizes the total energy of the system. Kohn and Sham took the theorems a step further and developed a set of self-consistent equations

$$n(\mathbf{r}) = \sum_{k=1}^{N} |\psi_k(\mathbf{r})|^2 \qquad \text{(Eq 1.17)}$$

$$V_{\text{eff}}(\mathbf{r}) = V(\mathbf{r}) + \frac{\delta E_{XC}[n]}{\delta n(\mathbf{r})} + \int d^3r\,' n(\mathbf{r}') \frac{1}{\mathbf{r}-\mathbf{r}'} \qquad \text{(Eq 1.18)}$$

$$\left[-\frac{1}{2}\nabla^2 + V_{\text{eff}}(\mathbf{r})\right] \psi_k(\mathbf{r}) = \epsilon_k \psi_k(\mathbf{r}) \qquad \text{(Eq 1.19)}$$

$$E = \sum_{k=1}^{N} \epsilon_k - \frac{1}{2} \int d^3r d^3r'\, n(\mathbf{r}) \frac{1}{\mathbf{r}-\mathbf{r}'} n(\mathbf{r}') + E_{XC}[n] - \int d^3r\, V_{XC}[n(\mathbf{r})] n(\mathbf{r}) \qquad \text{(Eq 1.20)}$$

where the exchange and correlation energies appear as additional terms in the effective potentials as shown in the equation 1.18. The self-consistent iteration starts with an initial guess of the electron density, which is used to calculate the effective potentials with equation 1.18. The Hamiltonian is then diagonalized to solve for a new wavefunction in equation 1.19, which in turn yields a new electron density. This process is continued until self-consistency is reached and the total energy is at last calculated with equation 1.20.

The initial work by Kohn and Sham assumed electron density as a slowly varying function. This was called local density approximation (LDA) and was successful in predicting many physical properties [56]. However, a homogeneous electron gas cannot be assumed in a molecular system. Researchers in the early 1990s developed the generalized gradient approximation (GGA) [64]. This further improves the already successful LDA by remedying the overestimation of the correlation energy and underestimation of the exchange energy to some extent. As DFT offers a more accurate evaluation of the total energy than HF method, all reported calculations in this thesis are based on DFT.

The above discussions deal with the electron-electron interaction terms in the Schrodinger equation. The pseudopotential approximation allows a simplified electronic wavefunction by replacing the strong ionic potential by a weaker pseudopotential. As a result, the true, but rapidly oscillating, portion of the valence electron wavefunction in the core region can be substituted by a set of smoother wavefunctions, as shown in figure 1.9. As the spatial frequency of the pseudo-wavefunctions is lower, the pseudopotential approximation reduces the size of the basis set, which is proportional to the wavevector, k. In addition, it reduces the number of electrons involved in the calculation as the core electrons are not accounted for explicitly. One of the many ways the pseudopotentials are generated is described in reference [65], which covers a wide range of elements including the transition metals. At the same time, this scheme requires a smaller cut-off energy compare to other methods. This translates to less expensive calculations.

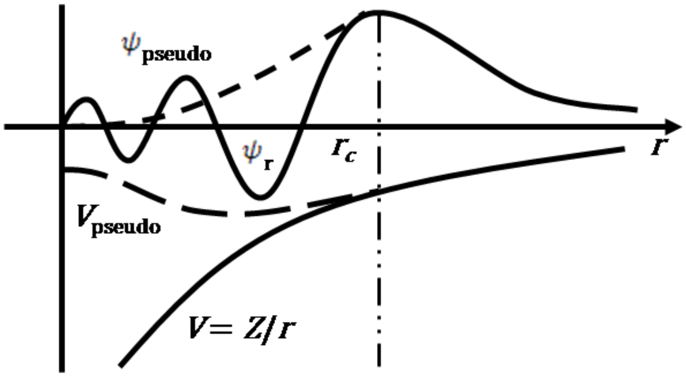

Figure 1.9, schematic illustration of the all electron (solid line) and pseudoelectron (dashed line) potentials and their corresponding wavefunctions.

One last component in the total energy calculation is the ion-ion interaction in the Schrodinger equation. As the Coulomb interaction between the ions is long-range in both real space and reciprocal space, the Coulomb energy is extremely difficult to compute. Ewald in the early 1900s developed a rapidly converging method to calculate the Coulomb energy over periodic lattices [66]. Further corrections were introduced in [56]. The total contribution from the ion-ion interaction is then

$$E_{\mathrm{ion}} = \frac{1}{2}\sum_{I,J} Z_I Z_J e^2 \left\{\sum_l \frac{\mathrm{erfc}(\eta|\mathbf{R}_1+l-\mathbf{R}_2|)}{|\mathbf{R}_1+l-\mathbf{R}_2|}\right\} - \frac{2\eta}{\sqrt{\rho}}\delta_{IJ} + \frac{4\pi}{\Omega}\sum_{\mathrm{G}\neq 0} \frac{e^{-\frac{|\mathrm{G}|^2}{4\eta^2}\cos\,[(\mathbf{R}_1-\mathbf{R}_2)\cdot\mathrm{G}]-\frac{\pi}{\eta^2\Omega}}}{|\mathrm{G}|^2}$$

(Eq 1.21)

In addition, one should be aware of the scaling of the calculations. What the above discusses is the theoretical backbone of the first principles calculations for any given system, regardless of the practicality. The cost of conventional matrix diagonalization increases as the third power of the number of basis states. What this means is that doubling the number of electrons in the calculation approximately increases the computational time eight-fold. As a result, the number of electrons, and hence atoms, included in a system being studied is limited to only about tens of atoms.

Besides improving the algorithm of the matrix diagonalization and switching to more powerful computers, localized basis sets allows less expensive calculations compared to plane-wave basis sets. A localized basis set comprises of basis functions that resembles the *s*, *p*, *d* and *f* atomic orbitals. Hence basis functions are needed. However, there is no systematic way to improve the accuracy with localized basis sets, unlike plane-waves which can gradually increase the cut-off energy to include more plane-wave basis functions to approach better accuracy. Furthermore, localized basis sets are susceptible to basis set superposition error as neighboring basis functions overlap with each other.

## 1.5 Structure of this thesis

After the brief introductions and motivations of the topics covered and techniques used in this thesis, chapter 2 will report the experimental realization of the dielectric integrated monolayer field effect transistor (DI-mFET). This is followed by a GIXD characterization and a first principles calculations based modeling of the monolayer in chapter 3. Chapter 4 changes the topic to investigate molecular memory theoretically. Inspired by the successful work, a protocol of determining packing structure of organic crystals is under development in chapter 5. Finally, future work is recommended in the last chapter, which also draws conclusions for this thesis.

# References

[1] *ITRS 2005*, Emerging Research Devices, 2005

[2] *ITRS 2007*, Emerging Research Devices, 2007

[3] Tsumura, A.; Koezuka, H.; Ando, T., "Macromolecular electronic device: Field-effect transistor with a polythiophene thin film," *Appl. Phys. Lett.*, *49*, **1986**, 1210-1212

[4] Chang, P. C.; Molesa, S. E.; Murphy, A. R.; Frechet, J. M. J.; Subramanian, V., "Inkjetted crystalline single monolayer oligothiophene OTFTs," *IEEE T. Electron Dev.*, *53*, **2006**, 594-600

[5] Shaw, J. M.; Seidler, P. F., "Organic electronics: Introduction," *IBM J. Res. & Dev.*, *45*, **2001**, 3-9

[6] Horowitz, G., "Organic thin film transistors: From theory to real devices," *J. Mater. Res.*, *19*, **2004**, 1946-1962

[7] Sirringhaus, H., "Device physics of solution-processed organic field-effect transistors," *Adv. Mater.*, *17*, **2005**, 2411-2425

[8] Koezuka, H.; Tsumura, A.; Ando, T., "Field-effect transistor with polythiophene thin film," *Synthetic Met.*, *18*, **1987**, 699-704

[9] Sirringhaus, H., "Integrated optoelectronic devices based on conjugated polymers," *Science*, *280*, **1998**, 1741-1744

[10] Podzorov, V.; Pudalov, V. M.; Gershenson, M. E., "Light-induced switching in back-gated organic transistors with built-in conduction channel," *Appl. Phys. Lett.*, *85*, **2004**, 6039-6041

[11] Ha, W. H.; Choo, M. H.; Im, S., "Electrical properties of $Al_2O_3$ film deposited at low temperature," *J. Non-Cryst. Solids*, *303*, **2002**, 78-82

[12] Lee, J.; Kim, J. H.; Im, S., "Pentacene thin-film transistors with $Al_2O_{3+x}$ gate dielectric films deposited on indium-tin-oxide glass," *Appl. Phys. Lett.*, *83*, **2003**, 2689-2691

[13] Majewski, L. A.; Schroeder, R.; Grell, M.; Glarvey, P. A.; Turner, M. L., "High capacitance organic field-effect transistors with modified gate insulator surface," *J. Appl. Phys*., *96*, **2004**, 5781-5787

[14] Rutenberg, I. M.; Scherman, O. A.; Grubbs, R. H.; Jiang, W.; Garfunkel, E.; Bao, Z. N., "Synthesis of polymer dielectric layers for organic thin film transistors via surface-initiated ring-opening metathesis polymerization," *J. Am. Chem. Soc.*, *126*, **2004**, 4062-4063

[15] Chua, L. L.; Ho, P. K. H.; Sirringhaus, H.; Friend, R. H., "High-stability ultrathin spin-on benzocyclobutene gate dielectric for polymer field-effect transistor," *Appl. Phys. Lett.*, *84*, **2004**, 3400-3402

[16] Yan, H.; Yoon, M. H.; Facchetti, A.; Marks, T. J., "Organic field-effect transistors based on a crosslinkable polymer blend as the semiconducting layer," *Appl. Phys. Lett.*, *87*, **2005**, 183501

[17] Fontaine, P.; Goguenheim, D.; Deresmes, D.; Vuillaume, D., "Octadecyltrichlorosilane monolayers as ultrathin gate insulating films in metal-insulator-semiconductor devices," *Appl. Phys. Lett.*, *62*, **1993**, 2256-2258

[18] Yoon, M. H.; Facchetti, A.; Marks, T. J., "σ-π molecular dielectric multilayers for low-voltage organic thin-film transistors," *P. Natl. Acad. Sci. USA*, *102*, **2005**, 4578-4682

[19] Zilker, S. J.; Detcheverry, C.; Cantatore, E.; de Leeuw D. M., "Bias Stress in organic thin-film transistors and logic gates," *Appl. Phys. Lett.*, *79*, **2001**, 1124-1126

[20] Chang, P. C., "Improving performance in oligothiophene based semiconductor devices via functionality," PhD thesis, University of California, Berkeley, **2005**

[21] Aviram, A.; Ratner, M. A., "Molecular rectifiers," *Chem. Phys. Lett.*, *29*, **1974**, 277-283

[22] Joachim, C.; Gimzewski, J. K.; Avriam, A., "Electronics using hybrid-molecular and mono-molecular devices," *Nature*, *408*, **2000**, 541-548

[23] Stokbro, K.; Taylor, J.; Brandbyge, M., "Do Aviram-Ratner diodes rectify?", *J. Am. Chem. Soc.*, *125*, **2003**, 3674-3675

[24] Wold, D. J.; Frisbie, C. D., "Fabrication and characterization of metal-molecule-metal junctions by conducting probe atomic force microscopy," *J. Am. Chem. Soc.*, *123*, **2001**, 5549-5556

[25] Venkataraman, L.; Klare, J. E.; Tam, I. W.; Nuckolls, C.; Hybertsen, M. S., Steigerwald, M. L., "Single-molecule circuits with well-defined molecular conductance," *Nano Lett.*, *6*, **2006**, 458-462

[26] Tans, S. J.; Verschueren, A. R. M.; Dekker, C., "Room-temperature transistor based on a single carbon nanotube," *Nature*, *393*, **1998**, 49-52

[27] Ambegaokar, V.; Halperin, B. I.; Langer, J. S., "Hopping conductivity in disordered systems," *Phys. Rev. B.*, *4*, **1971**, 2612-2620

[28] Vissenberg, M. C. J. M.; Matters, M., "Theory of the field-effect mobility in amorphous organic transistors," *Phys. Rev. B.*, *57*, **1998**, 12964-12967

[29] Mott, N. F., "Conduction in non-crystalline materials – 3. Localized states in a pseudogap and near extremities of conduction and valence bands," Philos. Mag., 19, 1969, 835-852

[30] Brown, A. R.; Jarrett, C. P.; de Leeuw, D. M.; Matters, M., "Field-effect transistors made from solution-processed organic semiconductors," *Synthetic Met.*, *88*, **1997**, 37-55

[31] Le Comber, P. G.; Spear, W. E., "Electronic transport in amorphous silicon films," *Phys. Rev. Lett.*, *24*, **1970**, 509-511

[32] Horowitz, G.; Hajlaoui, R.; Delannoy P., "Temperature dependence of the field-effect mobility of sexithiophene: Determination of the density of traps," *J. Phys. III*, *5*, **1995**, 355-371

[33] Luo, Y.; Collier, C. P.; Jeppesen, J. O.; Nielsen, K. A.; DeIonno, E.; Ho, G.; Perkins, J.; Tseng, H. R.; Yamamoto, T.; Stoddart, J. F.; Heath, J. R., "Two-dimensional molecular electronics circuits," *ChemPhysChem*, *3*, **2002**, 519-525

[34] Wasserman, E., "The preparation of interlocking rings: A catenane," *J. Am. Chem. Soc.*, *82*, **1960**, 4433-4434

[35] Harrison, I. T.; Harrison, S., "The synthesis of a stable complex of a macrocycle and a threaded chain," *J. Am. Chem. Soc.*, *89*, **1967**, 5723-5724

[36] Ashton, P. R.; Goodnow, T. T.; Kaifer, A. E.; Reddington, M. V.; Slawin, A. M. Z.; Spencer, N.; Stoddart, J. F.; Vicent, C.; Williams, D. J., "A [2]catenane made to order," *Angew. Chem. Int. Ed. Engl.*, *28*, **1989**, 1396-1399

[37] Hunter, C. A., "Synthesis and structure elucidation of a new [2]catenane," *J. Am. Chem. Soc.*, *114*, **1992**, 5303-5311

[38] Anelli, P. L.; Ashton, P. R.; Ballardini, R.; Balzani, V.; Delgado, M.; Gandolfi, M. T.; Goodnow, T. T.; Kaifer, A. E.; Philp, D.; Pietraszkiewwicz, M.; Prodi, L.; Reddington, M. V.; Slawin, A. M. Z.; Spencer, N.; Stoddart, J. F.; Vicent, C.; Williams, D. J., "Molecular meccano 1 [2]rotaxanes and a [2]catenane made to order," *J. Am. Chem. Soc.*, *114*, **1992**, 193-218

[39] Gunter, M. J.; Johnston, M. R., "Towards molecular scale mechano-electronic devices: Porphyrin catenanes," *J. Am. Chem. Soc. Commun.*, *17*, **1992**, 1163-1165

[40] Vogtle, F.; Muller, W. M.; Muller, U.; Bauer, M.; Rissanen, K., "Photoswitchable catenanes," *Angew. Chem. Int. Ed. Engl.*, *32*, **1993**, 1295-1297

[41] Benniston, A. C.; Harriman, A., "A light-induced molecular shuttle based on a [2]rotaxane-derived triad," *Angew. Chem. Int. Ed. Engl.*, *32*, **1993**, 1459-1461

[42] Bissell, R. A.; Cordova, E.; Kaifer, A. E.; Stoddart, J. F., "A chemically and electrochemically switchable molecular shuttle," *Nature*, *369*, **1994**, 133-137

[43] Collier, C. P.; Mattersteig, G.; Wong, E. W.; Luo, Y.; Beverly, K.; Sampaio, J.; Raymo, F. M.; Stoddart, J. F.; Heath, J. R., "A [2]catenane-based solid state electronically reconfigurable switch," *Science*, *289*, **2000**, 1172-1175

[44] Green, J. E.; Choi, J. W.; Boukai, A.; Bunimovich, Y.; Johnston-Halperin, E.; DeIonno, E.; Luo, Y.; Sheriff, B. A.; Xu, K.; Shin, Y. S.; Tseng, H. R.; Stoddart, J. F.; Heath, J. R., "A 160-kilobit molecular electronic memory patterned at $10^{11}$ bits per square centimetre," *Nature*, *445*, **2007**, 414-417

[45] Flood, A. H.; Peters, A. J.; Vignon, S. A.; Steuerman, D. W.; Tseng, H. R.; Kang, S.; Heath, J. R.; Stoddart, J. F., "The role of physical environment on molecular electromechanical switching," *Chem. Eur. J.*, *10*, **2004**, 6558-6564

[46] Choi, J. W.; Flood, A. H.; Steuerman, D. W.; Nygaard, S.; Braunschweig, A. B.; Moonen, N. N. P.; Laursen, B. W.; Luo, Y.; DeIonno, E.; Peters, A. J.; Jeppesen, J. O.; Xu, K.; Stoddart, J. F.; Heath, J. R., "Ground-state equilibrium thermodynamics and switching kinetics of bistable [2]rotaxanes switched in solution, polymer gels, and molecular electronic devices," *Chem. Eur. J.*, *12*, **2006**, 261-279

[47] Norgaard, K.; Laursen, B. W.; Nygaard, S.; Kjaer, K.; Tseng, H. R.; Flood, A. H.; Stoddart, J. F.; Bjornholm, T., "Structural evidence of mechanical shuttling in condensed monolayers of bistable rotaxane molecules," *Angew. Chem. Int. Ed.*, *44*, **2005**, 7035-7039

[48] DeIonno, E.; Tseng, H. R.; Harvey, D. D.; Stoddart, J. F.; Heath, J. R., "Infrared spectroscopic characterization of [2]rotaxane molecular switch tunnel junction devices," *J. Phys. Chem. B.*, *110*, **2006**, 7609-7612

[49] Deng, W. Q.; Muller, R. P.; Goddard, W. A., "Mechanism of the Stoddart-Heath bistable rotaxane molecular switch," *J. Am. Chem. Soc.*, *126*, **2004**, 13562-13563

[50] Jang, S. S.; Jang, Y. H.; Kim, Y. H.; Goddard, W. A.; Choi, J. W.; Heath, J. R.; Laursen, B. W.; Flood, A. H.; Stoddart, J. F.; Norgaard, K.; Bjornholm, T., "Molecular dynamics simulation of amphiphilic bistable [2]rotaxane Langmuir monolayers at the air/water interface," *J. Am. Chem. Soc.*, *127*, **2005**, 14804-14816

[51] Jang, S. S.; Jang, Y. H.; Kim, Y. H.; Goddard, W. A.; Flood, A. H.; Laursen, B. W.; Tseng, H. R.; Stoddart, J. F.; Jeppesen, J. O.; Choi, J. W.; Steueman, D. W.; DeIonno, E.; Heath, J. R., "Structures and properties of self-assembled monolayers of bistable [2]rotaxanes on Au (111) surfaces from molecular dynamics simulations validated with experiment," *J. Am. Chem. Soc.*, *127*, **2005**, 1563-1575

[52] Jang, Y. H.; Goddard, W. A., "Mechanism of oxidative shuttling for [2]rotaxane in a Stoddart-Heath molecular switch: Density functional theory study with continuum-solvation model," *J. Phys. Chem. B*, *110*, **2006**, 7660-7665

[53] Dichtel, W. R.; Heath, J. R.; Stoddart, J. F., "Designing bistable [2]rotaxanes for molecular electronic devices," *Philos. T. R. Soc. A*, *365*, **2007**, 1607-1625

[54] The Nobel Foundation, The Nobel Prize in Physics 1915, accessed on January 22, 2008, <http://nobelprize.org/nobel_prizes/physics/laureates/1915/index.html>

[55] Fultz, B.; Howe, J. M., <u>Transmission electron microscopy and diffractometry of materials</u>. Springer-Verlag, **2001**

[56] Yin, M. T.; Cohen, M. L., “Theory of static structural properties, crystal stability, and phase-transformations: Applications to Si and Ge,” *Phys Rev. B*, *26*, **1982**, 5668-5687

[57] Krotov, Y. A.; Lee, D. H.; Louie, S. G., “Low energy properties of (n,n) carbon nanotubes,” *Phys. Rev. Lett.*, *78*, **1997**, 4245-4248

[58] Payne, M. C.; Teter, M. P.; Allan, D. C.; Arias, T. A.; Joannopoulos, J. D., “Iterative minimization techniques for ab inito total-energy calculations: Molecular dynamics and conjugate gradients,” *Rev. Mod. Phys.*, *64*, **1992**, 1045-1097

[59] Thijssen, J. M., Computational Physics, 2nd edition. Cambridge University Press, **2007**

[60] Griffiths, D. J., Introduction to Quantum Mechanics. Prentice-Hall, **1995**

[61] Merzbacher, E., Quantum Mechanics, 3rd edition. John Wiley & Sons, **1998**

[62] Hohenberg, P.; Kohn, W., “Inhomogeneous electron gas,” *Phys. Rev. B*, *136*, **1994**, B864-B871

[63] Kohn, W.; Sham, L. J., “Self-consistent equations including exchange and correlation effects,” *Phys. Rev.*, *140*, **1965**, A1133-A1138

[64] Perdew, J. P.; Burke, K.; Wang, Y., “Generalized gradient approximation for the exchange-correlation hole of a many-electron system,” *Phys. Rev. B*, *54*, **1996**, 16533-16539

[65] Troullier, N.; Martins, J. L., “Efficient pseudopotentials for plane-wave calculations,” *Phys. Rev. B*, *43*, **1991**, 1993-2006

[66] Ewald, P. P., "The calculation of optical and electrostatic grid potential," *Ann. Phys. Berlin*, *64*, **1921**, 253-287

# Chapter 2

# Monolayer transistors

The term “self-assembly” has been used to describe a variety of phenomena governing systems where molecules organize into well-ordered films or macromolecules. The chemical bonding that mediate self-assembly are surface selective, therefore film formation typically stops after the deposition of the first assembled layer. Such a mechanism is a common method for forming self-assembled monolayers (SAM) [1]. In this chapter, the channel material and the gate dielectric of the transistors studied are exclusively deposited as SAM. The unique experimental procedures are first outlined, followed by the transistor characteristics and analysis, and finally discussions on challenges faced and possible improvements.

## 2.1 Motivations and background information

In section 1.1, the motivations to investigate monolayer transistor have been outlined. The reduction in the off-state current and the subthreshold slope, together with the improvement in the bias-stress effect were readily obvious in the monolayer field effect transistor (mFET) demonstrated. Furthermore, mFET can be viewed as another step towards the paradigm of molecular transistor where a single molecule bridges the source, drain and gate electrodes.

Previous work by Chang et al. successfully demonstrated the first mFET using a hexa-thiophene ($T_6$) based molecule as shown in figure 2.1a. Figure 2.1b shows the structure of the fabricated device, wherein a monolayer of $T_6$ served as the channel of the transistor and the gate dielectric was a 100nm thermal oxide grown on the heavily-doped silicon back-gate. This device exhibited superior characteristics compared to traditional organic thin film transistors (OTFTs), in terms of off-state current, subthreshold slope and bias-stress effect [2]. These improvements, attributed to the monolayer-thick semiconducting channel, were achieved without degrading the on-state performance.

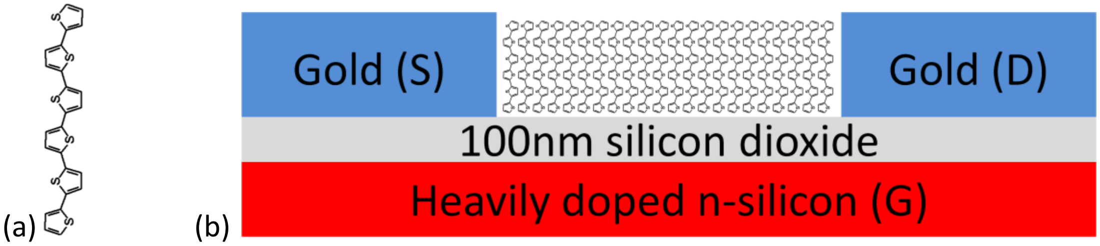

Figure 2.1, monolayer FET demonstrated in previous work. (a) the hexa-thiophene molecule and (b) the device structure of the monolayer FET demonstrated where a monolayer of the molecule shown in (a) forms the channel and the gate dielectric is a 100nm thick silicon dioxide

Towards the paradigm of single molecule transistors, the next obvious step was to integrate the gate dielectric into the molecules to replace the thick silicon dioxide. Through the reduced dielectric thickness, the electrostatics could further be improved. At the same time, a higher drive current could be attained. Furthermore, as shown in figure 2.2, there existed covalent bonds between the dielectric (alkane) and the semiconductor (quarter-thiophene, $T_4$) in the molecules synthesized for the integration. These bonds guaranteed a perfect semiconductor-dielectric interface. In this regard, a dielectric-integrated monolayer field effect transistor (DI-mFET) would be a better system than the silicon-based MOSFET, which had a non-zero interface trap density.

Before fabricating a three-terminal device, a simple two-terminal capacitor structure was built to evaluate the quality of the integrated dielectric. This revealed that a novel "zero-overlap" structure was necessary for a minimally functioning device. Challenges, solutions and future outlook are discussed afterwards.

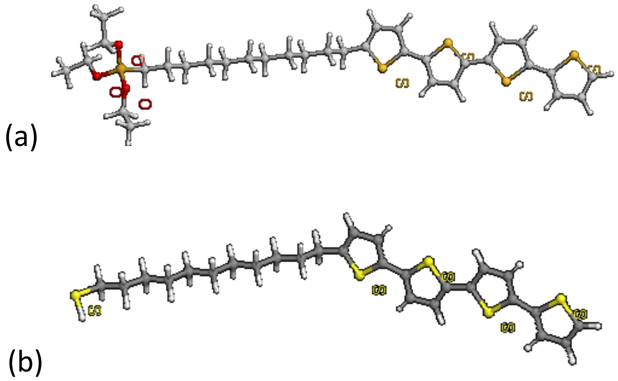

Figure 2.2, the different versions of alkyl-thiophene molecules synthesized for this work, (a) $T_4C_{11}Si(EtO)_3$, (b) $T_4C_{11}SH$

## 2.2 Capacitor structure

This section outlines the experimental procedures of fabricating the capacitor structure where a $T_4C_{11}$ monolayer was sandwiched between two electrodes. The two-terminal current-voltage (I-V) measurements presented an evaluation of the leakage property of the integrated dielectrics of the molecules shown in figure 2.2.

### 2.2.1 Experimental procedures

Capacitor structures using Langmuir-Blodgett (LB) monolayer of $T_4C_{11}Si(EtO)_3$, as shown in figure 2.2b, were fabricated on heavily doped silicon wafers. About 75μL of $T_4C_{11}Si(EtO)_3$ solution in chloroform was added to acidified nanopure water in an LB trough. After allowing sufficient time for the molecules to organize on the water surface, the film was collected by slowly pulling the substrate out from the LB trough. This resulted in a monolayer of $T_4C_{11}Si(EtO)_3$ depositing on the silicon substrate. While the heavily doped silicon wafer served as the bottom electrode, the top electrode was formed by evaporating patterned gold electrodes through a shadow mask. Other studies in literature have shown that thermal evaporation can potentially damage monolayer and results in shorts between the top and bottom electrodes. Hence, liquid nitrogen ($LN_2$) was used to cool the substrate down to around 100K during the evaporation in order to minimize the damage.

### 2.2.2 Two-terminal I-V characteristics

Figure 2.3 shows a two-terminal I-V measurement of the capacitor structure of a $T_4C_{11}Si(EtO)_3$ monolayer film fabricated as described. Even after a voltage bias as large as 10V, the forward and backward sweeps overlapped each other closely. This suggested that the monolayer did not breakdown electrically within the swept voltage range. A typical example of a dielectric breakdown I-V characteristic in log scale is included as an inset in figure 2.3. A distinct jump in current and the disparity between the forward and backward sweeps were featured.

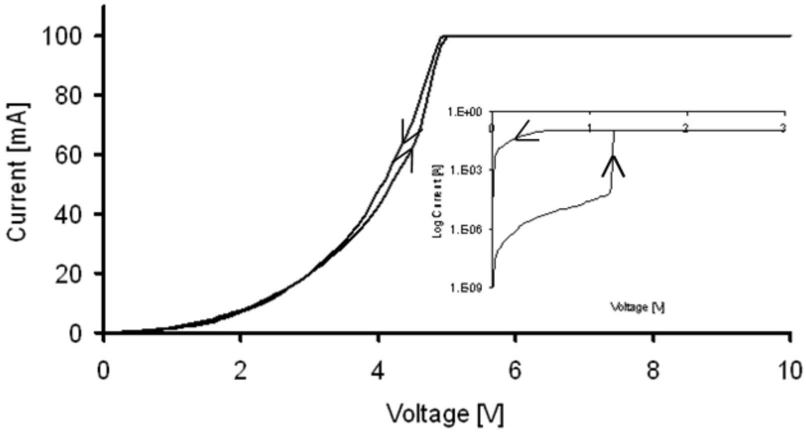

Figure 2.3, I-V characteristic of a typical capacitor structure. Inset shows a typical I-V characteristic that exhibits breakdown of the dielectric. Area = 50μm×100μm.

Using the current measured at 0.5V and the area of the top gold electrode (50μm by 100μm), the current through a single molecule of $T_4C_{11}SH$ could be estimated to be 0.2pA, which fell within the range of published literature [3]. Taking the on-state current to be on the order of 100nA from the previous work [2] and setting a minimum required on/off ratio to be 100, i.e. the maximum gate leakage current allowed equaled 1nA, one could compute that the maximum area the source/drain electrode were allowed to overlap with the gate was merely 800nm$^2$. This implied that simply replacing the 100nm silicon dioxide in the conventional OTFT structure shown in figure 2.1b with the integrated dielectric would yield too much gate leakage current. Therefore, the novel fabrication process flow outlined in the following section was necessary to minimize, if not completely eliminate, the overlap area problem.

## 2.3 Dielectric integrated mFET (DI-mFET)

As illustrated above, the integrated dielectric was not very insulating. As a result, any overlap between the source/drain and the gate electrodes would constitute a gate leakage current that inevitably masked the modulation of the source-drain current due to the gate biasing. A unique experimental procedure of fabricating the novel dielectric integrated monolayer field effect transistor (DI-mFET) yielding virtually “zero overlap” was devised and is presented in this section. The 3-terminal I-V characteristics of the fabricated device are shown. This is the first demonstration of a DI-mFET.

### 2.3.1 Experimental procedures

The DI-mFET was fabricated as shown in figure 2.4. Undoped silicon wafers were oxidized, followed by photolithography which defined the oxide islands where the source and drain electrodes of the transistor would be formed. The exposed oxide regions were then dry-etched to produce straight sidewalls. Another photolithography step defined liftoff patterns through which gold sources, drains, and gates were evaporated simultaneously and in a self-aligned fashion. Layer-by-layer gold evaporations were performed at 0.02nm/s. After every deposition step, an average height difference between the oxide islands and evaporated gold islands was accurately measured with atomic force microscope (AFM). This process was repeated until the target thickness was reached. At this point, a screening process was carried out. Two-terminal I-V curves were measured across the source-drain (S-D), source-gate (S-G) and drain-gate (D-G) terminals. Sites with all three measurements resulted in open circuits were recorded for future three-terminal measurements. These would be the devices to be tested for FET behavior. The formation of the monolayer was done by soaking the samples in $T_4C_{11}SH$ solutions ($T_4C_{11}SH$ dissolved in tetrahydrofuran (THF)) for 40+ hours. The long soaking period ensured the formation of high quality monolayer on the evaporated gold surface. The dies were withdrawn from the solution afterwards, rinsed with THF and blown dry with dry nitrogen ($N_2$).

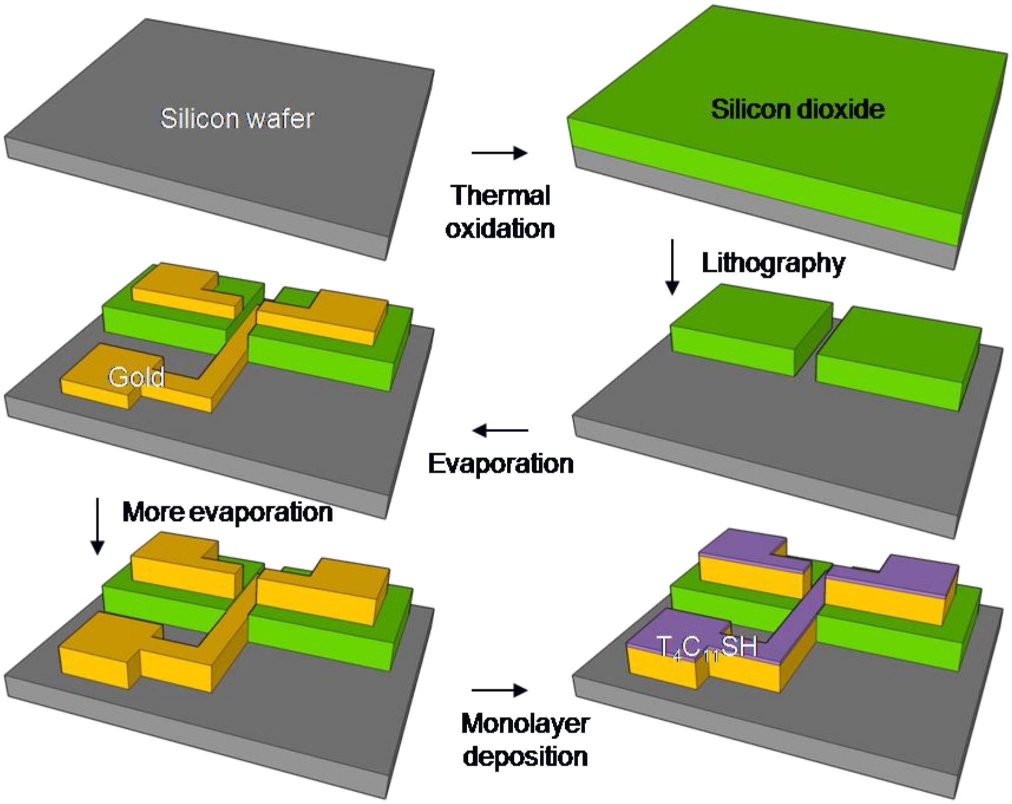

Figure 2.4, graphical illustration of the fabrication process of the first generation monolayer FET with integrated dielectric. Starting with a silicon wafer, a layer of 60nm silicon dioxide is thermally grown. It is then patterned and dry-etched. Layer-by-layer evaporation of gold is carried out to form the source, drain and gate terminals in a self-aligned fashion. At the end, the die is soaked in $T_4C_{11}SH$ solution for 40+hours for the monolayer deposition.

After the dies were withdrawn from the solution, rinsed and dried, three-terminal I-V characteristics were measured at the previously screened sites. They were compared against the two-terminal measurements to reveal changes due to the presence of the deposited monolayer.

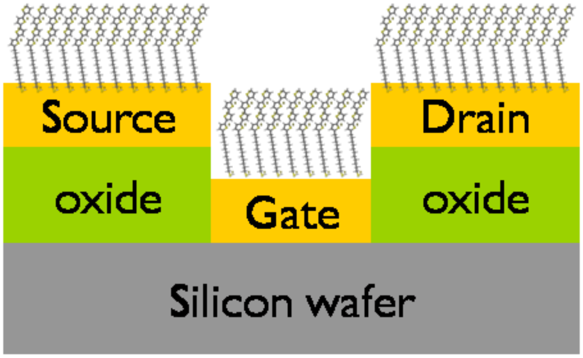

Figure 2.5, a cartoon schematic showing the cross section of an idealized DI-mFET.

Figure 2.5 shows an idealized finished product of the process described above. It should be emphasized that this was an arduous process. The challenges and difficulties would be discussed below. Note that due to the limited number of working devices and the nature of the material, the performance of the device shown was not optimized. For example, the samples were not baked under vacuum to drive out the residual solvent in order to minimize variations due to additional process steps. Furthermore, the I-V characteristics presented were measured in air, where the presence of oxygen and moisture were not excluded.

### 2.3.2 I-V characteristics of DI-mFET

Figure 2.6 shows a set of $I_DV_D$ curves successfully measured from one of the working DI-mFET fabricated with the process flow described in previous section. The non-idealities displayed includes 1) the concavity at the low $V_{DS}$ region, indicating the presence of a contact barrier, and 2) the large $I_D$ even under large positive gate bias, signifying the existence of residual field that does not emanate from the gate electrode.

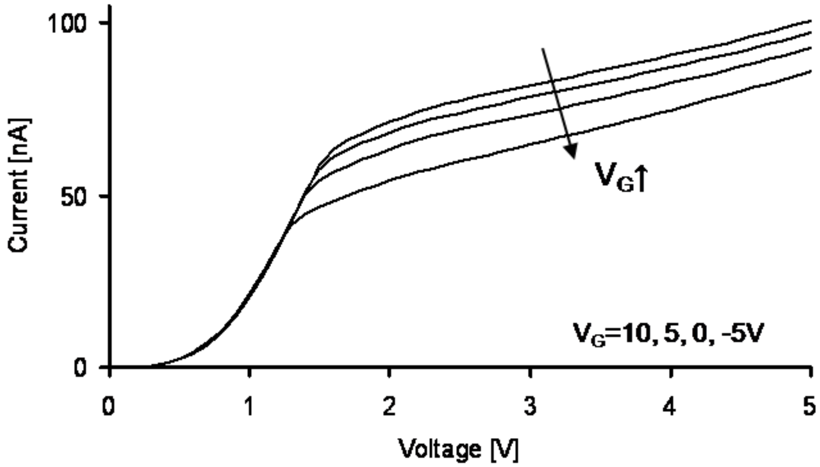

Figure 2.6, $I_DV_D$ curves measured from a first generation dielectric integrated monolayer FET, with W = 20μm and L = 2μm.

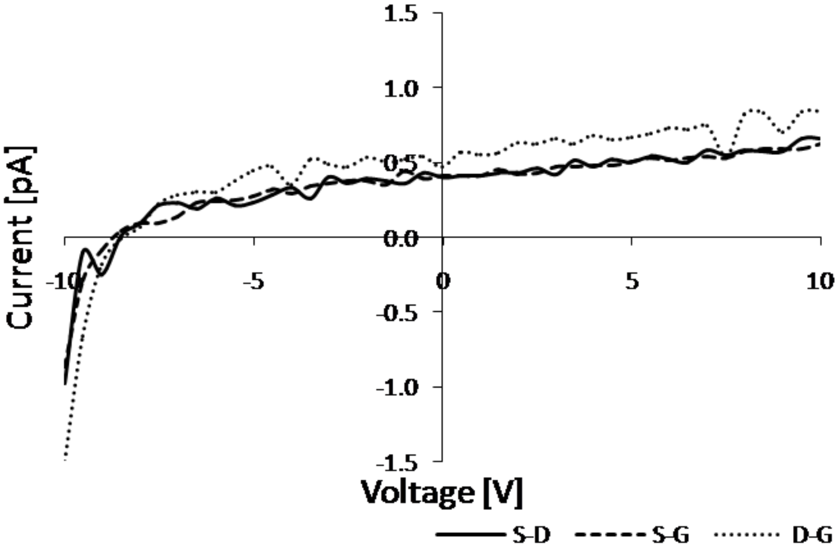

Figure 2.7, two-terminal measurement of the dielectric integrated monolayer FET, which yields the above $I_DV_D$ measurement, before soaking in $T_4C_{11}SH$ solution.

Figure 2.7 is the two-terminal S-D, S-G and D-G screening measurements taken before the sample was soaked in the $T_4C_{11}SH$ solution. The difference between the two was clear. Contrasting the measurements, the current must have flowed from the source terminal, through the semiconducting channel of $T_4$, to the drain terminal after the monolayer was deposited. In addition, figure 2.6 also shows that gate bias was modulating the drain currents. To the best knowledge of the author, this was the first demonstration of a DI-mFET to-date. Although measurement of $I_DV_G$ was attempted, it was believed that the fragile device was destroyed by the current flowing through it after the initial $I_DV_D$ sweeps.

## 2.4 Analysis

This section focuses on analyzing the $I_DV_D$ shown in figure 2.6. The contact barrier is modeled as an air-gap; the parasitic resistive path is explained; and carrier mobility is extracted.

### 2.4.1 Contact barrier modeling

The concavity in the $I_DV_D$ curves at low $V_{DS}$ region hinted the presence of contact barriers at the source/drain contacts. It will be shown later that a thin layer of vacuum is believed to be the origin of this concavity. A modified version of the Simmons tunneling equation [4]

$$I(V) = \left(\frac{qA}{2\pi h d^2}\right)\left\{\left(\phi_b - \frac{qV}{2}\right) e^{\left[-\frac{2d}{\hbar}\sqrt{2m\left(\phi_b - \frac{\boldsymbol{N}qV}{2}\right)}\right]} - \left(\phi_b + \frac{qV}{2}\right) e^{\left[-\frac{2d}{\hbar}\sqrt{2m\left(\phi_b + \frac{\boldsymbol{N}qV}{2}\right)}\right]}\right\}$$

(Eq 2.1)

was used to model this barrier. In the above equation, $\phi_b$ = 5.1eV, the barrier height, equaled the work function of gold. The area, A, and the thickness of the tunneling barrier, d, were parameters to be estimated. An additional fitting parameter. ***N*,** was introduced and its significance will be discussed later.

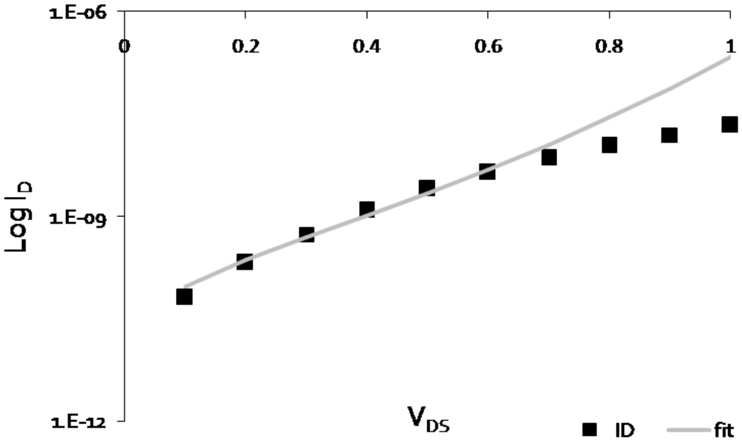

Figure 2.8, the low $V_{DS}$ region of the $I_DV_D$ shown in figure 2.6. The grey line is the calculated $I_D$ according to the modified Simmons tunneling equation.

Figure 2.8 presents an extract of the low $V_{DS}$ region from the $I_DV_D$ shown in figure 2.6 and the modeled curve from the above equation with A, d, and ***N*** equal to 70nm$^2$, 0.8nm and 7, respectively. Rather than simply being a set of correction factors, each has its physical meaning. A = 70nm$^2$ was the area through which the current flows. This corresponded to the area the $T_4$ segment of the molecule touched the source/drain electrodes. This area could also be written as A = $W_{eff}$×overlap. Since the $T_4$ segment touching the source/drain electrodes was about as long as 1nm, $W_{eff}$ =70nm. This was the effective width of the device. The difference between $W_{eff}$ and the physical W = 2μm would be discussed later.

The value of d = 0.8nm and ***N*** = 7 should be considered together. In the original Simmons tunneling equation, *d* was the width of the tunneling barrier. The introduction of ***N*** was similar to the ideality factor, $\eta$, in the diode equation. Being in the denominator in the diode equation, $\eta > 1$ could be translated to less-than-ideal injection of the minority carriers. ***N*** in the numerator of the modified Simmons tunneling equation with ***N*** = 7 meant a more efficient injection through the 0.8nm thick tunneling barrier.

### 2.4.2 Parasitic resistive path

Another obvious deviation of the $I_DV_D$ shown in figure 2.6 from the square-law MOSFET equation, and the conventional OTFT, was that the device did not turn off even at large positive bias. This was attributed to the presence of charged impurities and contaminants located in the vicinity of the monolayer semiconducting channel.

Figure 2.9 further elaborates this argument. In figure 2.9a, the operation of a conventional OTFT is shown. As a negative bias was applied, holes were attracted to the semiconductor-dielectric interface. They filled up the traps and allowed charge carriers to traverse the channel through the multiple trapping and release model (MTR) discussed in chapter 1. When the bias was removed, as shown in figure 2.9b, traps were emptied and charge carriers would be trapped instead of traversing through the channel. Figure 2.9c considers charged impurities/contaminants being placed in the vicinity of the channel. Upon negatively biasing the gate, traps were filled similar to that shown in figure 2.9a. However, when the bias was removed, the traps were not completely emptied as prevented by the charged impurities/contaminants. Even under a strong positive bias, the channel still remained conducting. This hypothesis was further supported by the relatively minor modulation of the drive current, relative to a large range of applied gate bias.

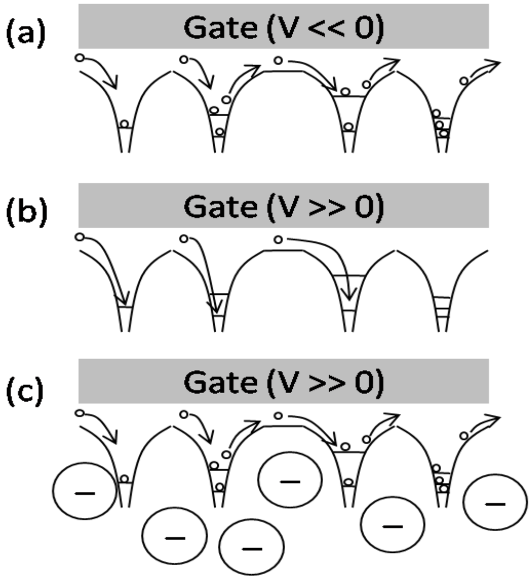

Figure 2.9, (a) when the gate is negatively biased, holes are attracted towards the surface and filled the traps. (b) When the gate is positively biased, holes are repelled from the surface, hence the traps are empty. Incoming charge carrier then will not be able to traverse through. (c) The gate is positively biased, but there are negatively charged impurities/contaminants on top of the monolayer. As a result, holes are still attracted to the surface to fill the traps. Thus, carriers can still pass through the channel.

### 2.4.3 Mobility extraction

Since the $I_DV_G$ could not be measured, $V_T$ was obtained by scaling the previous work to extract the mobility from the square law equation. Figure 2.10 shows the $I_DV_G$ measured from the monolayer FET illustrated in figure 2.1b, with the only difference being the monolayer was $T_4C_{11}Si(EtO)_3$, instead of $T_6$. A $V_T$ of -22V was found by extrapolating a straight line to the horizontal axis.

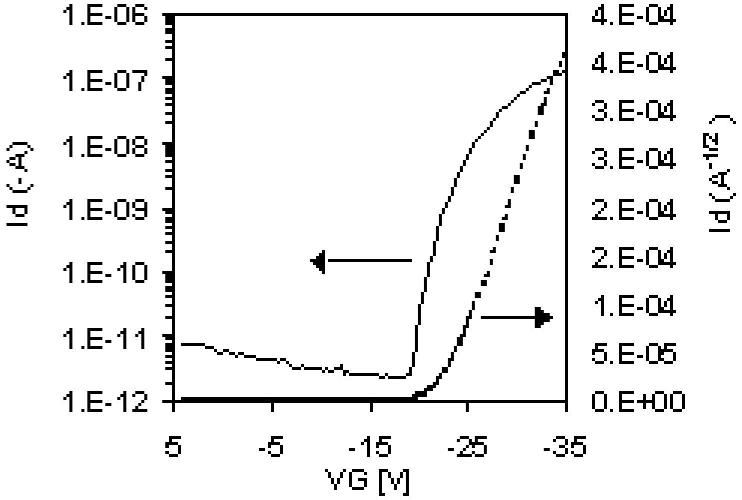

Figure 2.10, $I_D V_G$ measured from the monolayer FET in the previous work.

In the equation for threshold voltage, $V_T = V_{FB} - V_{OX}$. Since the first term was usually only on the order of volts, the large $V_T$ obtained was mainly attributed to the second term, $V_{OX}$. Directly scaling $t_{ox}$ from 100nm silicon dioxide in the previous work to approximately 1nm of alkane chain in this study reduced $V_{OX}$ by a factor of 100, and thus lowering $V_T$ to $V_{FB}$ – 0.22V. In this case, although the value of $V_{FB}$ could no longer be neglected, as only an order of magnitude estimation on mobility was attempted, $V_T$ was taken as 0V.

Using $V_T$ = 0V and the current at the onset of saturation, by applying the square law equation,

$$\mu = \frac{I_D}{\frac{W}{2L} C_{ox} (V_{GS} - V_T)^2} \qquad \text{(Eq 2.2)}$$

the mobility was approximated to be $2\times10^{-4}$cm$^2$/Vs. It was true that, gauged against the state-of-the-art and fully optimized OTFT, this extracted mobility was very low. However, the mobility observed in this study was quite inspiring if compared to the first

OTFT demonstrated [5] as discussed in section 1.1. Furthermore, typical mobilities exhibited by transistors made with $T_4$ ranged from $1\times10^{-4}cm^2/Vs$ to $6\times10^{-3}cm^2/Vs$. The fact that the extracted mobility fell to the lower end could also be explained through the MTR model discussed in chapter 1. AFM images revealing the granular nature of the gold surface will be shown in the following section. Such surface roughness caused disorder in the monolayer, hence more grain boundaries and trap states and a reduced mobility.

## 2.5 Discussions

This section discusses the challenges faced in the DI-mFET process flow and several probable solutions. The challenges were the roughness of the evaporated gold surface, molecules sticking to the sidewall of the source/drain electrodes and poor dielectric.

### 2.5.1 Challenges

Figure 2.11 shows an AFM image of an evaporated gold surface. The roughness of this surface was on the order of tens of nanometers, while the length of the $T_4C_{11}SH$ molecule was only approximately 2nm. Figure 2.12 portrays a disordered monolayer as a result of the roughness of the substrate. The disorder further led to incomplete coverage of the monolayer, especially at the abrupt troughs.

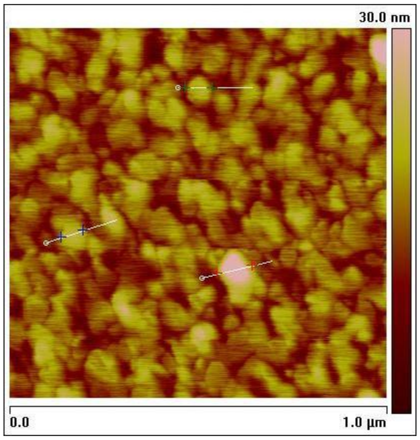

Figure 2.11, AFM image of an evaporated gold surface. The roughness of this representative sample is on the order of 10nm.

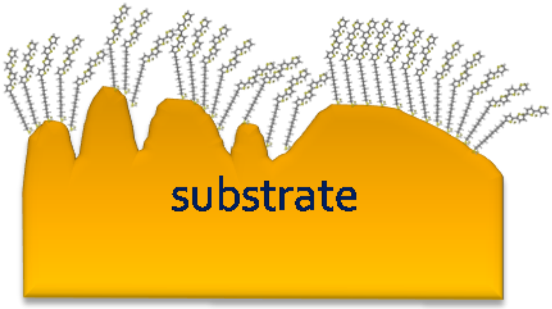

Figure 2.12, cartoon illustration of disordered monolayer deposited on top of rough substrate. Incomplete coverage of the monolayer can result, especially at the abrupt troughs.

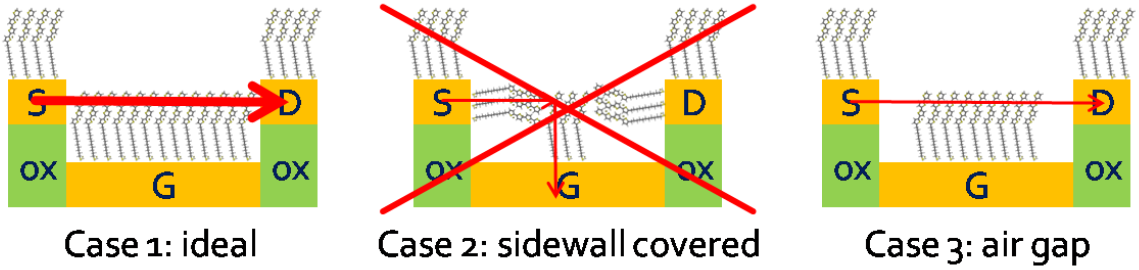

Figure 2.13, cartoon illustration of the 3 possible scenarios for conduction. Case 1 shows an ideal case that the source/drain electrodes touch the channel directly. In case 2, molecules stick to the sidewall of the source/drain electrodes, result in gate leakage current. And lastly, the air-gap scenario, which allows $I_{DS}$ to be measured, is depicted in case 3.

Figure 2.13 illustrates how a disordered monolayer may affect the current flow. In case 1, an ideal case is shown. The source/drain electrodes touch the semiconducting $T_4$ channel without any barrier. However, since the sidewall of the source/drain electrodes were the very same gold surface as that on top of the gate electrode, the condition depicted in case 2, should happen. Yet, an $I_DV_D$ similar to figure 2.6 could not be measured in this scenario. This was because when the current passed through the molecule at the source electrode into the semiconducting channel, it would preferably leak through the less resistive path to the gate electrode. Due to the incomplete monolayer coverage resulted from surface roughness, along the entire width of the device, a certain portion of the source electrode, corresponding to $W_{eff}$ introduced previously, would have been separated from the channel by an air-gap, as shown in case 3. As long as the resistance of the air-gap was smaller than that of the $C_{11}$ alkane tail, current would flow from the source electrode, through the channel to the drain, resulting in the $I_DV_D$ shown.

Although the roughness of the evaporated gold surface inevitably led to figure 2.6, it had also brought forth multiple problems. Firstly, according to the MTR model, the more the number of the grain boundaries, the more the traps and hence the lower the carrier mobility. To some extent, the reduced mobility adversely affected the yield. What caused a drastic decrease in term of yield was the combination of rough surface and small targeted gap size. The poor control of the metal deposition rate and the inaccurate crystal monitor readout both further augmented this problem. Moreover, AFM could no longer be used to characterize the morphology of the $T_4C_{11}SH$. Therefore, other techniques were utilized to understand this system in chapter 3.

In addition, a more fundamental challenge came from the molecule itself. The only reason that the unique process flow was adopted was because the poor dielectric property of the $C_{11}$ alkane tail did not support large overlap area between the source/drain electrodes and the gate.

## 2.5.2 Probable solutions

To avoid the sidewall coverage problem illustrated in figure 2.13, a simple modification to the described process flow could be devised. Instead of evaporating a single species of metal, a two-metal evaporation process could be attempted. However, one should be aware of the work function of the metal used. Using a combination of low work function metal as the first layer could possibly result in large contact barrier simply due to work function mismatch. In an ideal case, one would like the molecule to selectively bind to surface other than gold, which matched the work function of $T_4$. A recently developed version of the alkyl thiophene molecule with phosphonic acid binding moiety that allowed monolayer deposition on top of aluminum oxide surface met this criterion. A two-metal gold-aluminum film could be used for the electrodes. A thin layer of gold simply serving as the contacting layer to the channel should first be deposited, followed by evaporating aluminum, which provided the surface for the alkyl thiophene molecules to form a monolayer. The proposed structure is shown in figure 2.14.

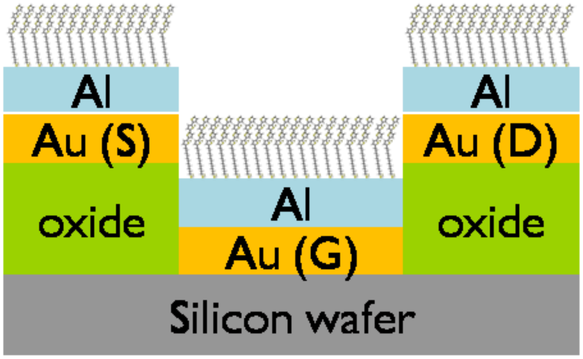

Figure 2.14, a schematic showing the cross section of the DI-mFET where the molecule would selective bind to aluminum oxide surface. A two-metal evaporation (gold first then aluminum) can then be used to prevent the sidewall coverage problem shown in figure 2.13.

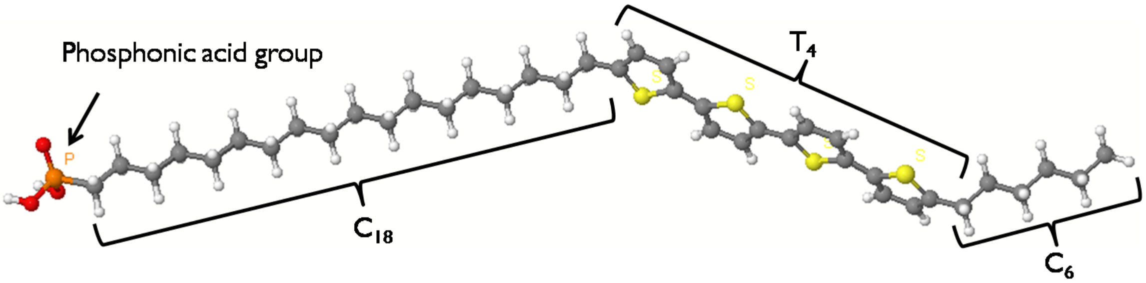

Figure 2.15, the hexyl-$T_4C_{18}PO(OH)_2$ molecule.

Since this process followed the previously described process flow, it inevitably suffered from the same roughness issue discussed. The foremost reason to adopt such an unconventional process and structure was the poor dielectric property in terms of leakage. To ameliorate this problem, a longer, more insulating dielectric should be incorporated in the alkyl thiophene molecule. Figure 2.15 shows a hexyl-$T_4C_{18}PO(OH)_2$ molecule. Apart from being much less soluble, this version offered three advantages over the original $T_4C_{11}SH$ molecule. Firstly, instead of $C_{11}$, the integrated dielectric was $C_{18}$. The lengthening of the alkane chain, according to reference [3], reduced the current through the molecule by 3 orders of magnitude. This directly translated to

1000X increase in allowed overlap area between the source/drain and the gate electrodes. Hence, a structure shown in figure 2.16 with well-controlled overlap area could be used. Since, the source/drain electrodes could be evaporated onto the monolayer, similar to the conventional OTFTs, air gap contact barriers could be eliminated.

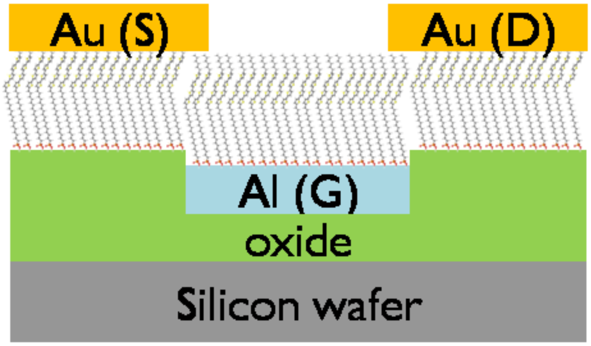

Figure 2.16, schematic showing the use of hexyl-$T_4C_{18}PO(OH)_2$ in DI-mFET, achieving a structure similar to conventional OTFT. CMP is employed to planarize the surface after aluminum deposition, resulting in that the roughness of the aluminum being comparable to that thermal oxide.

Additionally, as mentioned previously, the binding moiety of this molecule was phosphonic acid, allowing the monolayer to form on the surface of aluminum oxide. In order to construct the structure shown in figure 2.16, chemical-mechanical polishing (CMP) must be employed. While gold CMP could be difficult, aluminum CMP slurry was similar to that for polysilicon CMP. This reduced the roughness of the evaporated aluminum surface to a level comparable to an oxide surface. This is evidenced in figure 2.17, which shows the aluminum surface (a) before and (b) after CMP. Hence, the roughness problem that plagued the yield of the original process flow could be eradicated.

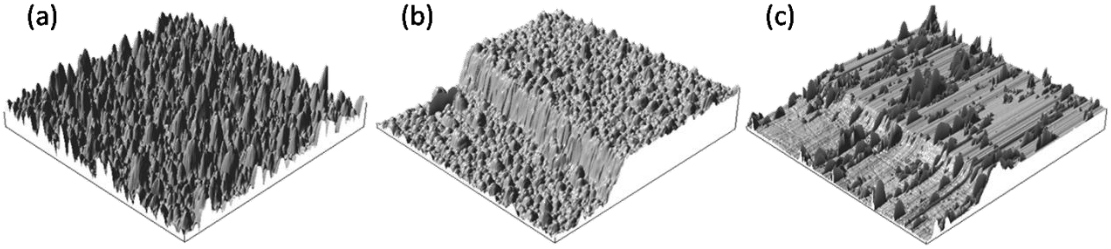

Figure 2.17, AFM image of an aluminum surface (a) right after evaporation, (b) being CMP-ed slightly and (c) when the entire CMP process finishes. In (c), the spikes are only AFM artifacts and do not correspond to any real features and the resulting surface roughness is comparable to that of a thermal oxide, hence eradicating the roughness problem plaguing the process flow described previously.

Lastly, it should be noticed that on the other end of the thiophenes, there was another alkyl group in this hexyl-$T_4C_{18}PO(OH)_2$ molecule. It allowed protection to the semiconducting thiophenes from the bombarding metal ions during metal evaporation. Furthermore, to some extent, the hexyl group functioned as another layer of insulator, additionally reducing the current flowing through the molecule.

## 2.6 Future outlook and summary

It was quite obvious that this work leapt ahead in the timeline and peeked at a future device with the current technologies. In addition to further improving the yield, it would be essential to take a step backward to better understand the monolayers that comprised of the DI-mFET, which will be presented in the next chapter.

In summary, the first demonstration of DI-mFET was reported. The current through the $T_4C_{11}SH$ molecule had been studied using a 2-terminal capacitor structure and the magnitude was found to be within the range reported in the literature. However, this translated to the necessity of using the “zero-overlap” structure with the process flow described. Despite low yield, $I_DV_D$ were measured from several DI-mFET. The non-idealities of the $I_DV_D$ included contact barrier and a parasitic resistive path. The disordered, incomplete coverage of the monolayer on the sidewall of the source/drain electrodes was the origin of the air gap contact barrier. This was modeled with a modified Simmons tunneling equation and reasonable agreement was achieved. Additionally, charged impurities and contaminants residing on the channel caused the parasitic resistive path. These charge induced field filled the traps without any the gate bias and caused the channel to remain conducting.

The main challenges of roughness of the evaporated gold surface and the poor dielectric were identified. Potential solutions, such as two-metal evaporation, the use of longer, more insulating hexyl-$T_4C_{18}PO(OH)_2$ molecule, and ultimately CMP-ing the surface to create a structure similar to the conventional OTFT, were proposed.

From the results presented in this chapter, the practicality of DI-mFET was questioned. Even with an improved yield, the mobility might at most be on-par with those of the conventional OTFTs. However, doubtlessly, this work presented a step towards the ultimate goal of single molecule transistors. As the transport through a single molecule was entirely different from that presented in chapter 1, the paradigm of single molecule transistors should still be pursued, but in a more careful manner.

# References

[1] Chang, P. C., “Improving performance in oligothiophene based semiconductor devices via functionality,” Ph.D. dissertation, University of California, Berkeley, **2005**

[2] Chang, P. C.; Molesa, S. E.; Murphy, A. R.; Frechet, J. M. J.; Subramanian, V., “Inkjetted crystalline single monolayer oligothiophene OTFTs,” *IEEE T. Electron Dev.*, *53*, **2006**, 594-600

[3] Salomon, A.; Cahen, D.; Lindsay, S.; Tomfohr, J.; Engelkes, V. B.; Frisbie, C. D., “Comparison of electronic transport measurements on organic molecules,” *Adv. Mater.*, *15*, **2003**, 1881-1890

[4] Simmons, J. G., “Generalized formula for the electric tunnel effect between similar electrodes separated by a thin insulating film,” *J. Appl. Phys*, *34*, **1963**, 1793-1803

[5] Tsumura, A.; Koezuka, H.; Ando, T., “Macromolecular electronic device: Field-effect transistor with a polythiophene thin film,” *Appl. Phys. Lett.*, *49*, **1986**, 1210-1212

# Chapter 3

# Structural study of alkyl-thiophene monolayers

Grazing incidence X-ray diffraction (GIXD) is a powerful technique to study the morphology of thin film systems. Distinct peaks recorded on the diffraction pattern form unique signatures to specific in-plane and out-of-plane structures. Combining with theoretical studies, in-depth understandings about the systems and accurate models can be derived. In this chapter, the alkyl-thiophene monolayers that formed the semiconducting channel in the dielectric integrated monolayer field effect transistors (DI-mFET) described in chapter 2 are analyzed with GIXD. At the same time, first principles calculations are carried out, under the constraints obtained experimentally, to generate insightful information regarding the monolayers.

## 3.1 Motivations

The demonstration of DI-mFET was reported in chapter 2. The observed low mobility in the device was attributed to the disorder [1] of the deposited monolayer. To improve the performance of future devices, it was essential to understand the packing structure of the monolayer forming the semiconducting channel. Since atomic force microscopy (AFM) could not be used to study the morphology of the $T_4C_{11}SH$ monolayer due to the surface roughness of the evaporated gold film, an alternative method was sought. Among the available techniques, GIXD was found to be a powerful tool to investigate the structure of films as thin as monolayers. The goal of this chapter is, therefore, to quantify the suggested disorder with GIXD. Additionally, the information hidden behind the peaks of the GIXD data is deciphered.

However, due to certain deficiencies of the experimental results to be further elaborated, first principles calculation based studies are used to further understand the system. The morphology of the $T_4C_{11}SH$ monolayer was simulated and explained. A model for the monolayer was developed, predicting additional peaks to be scrutinized in future studies.

## 3.2 Interpretation of the GIXD data

As discussed in chapter 1, X-ray diffraction (XRD) patterns are closely related to the structure factor of the material being studied. It is equivalent to the reciprocal lattice of the crystal being studied. To analyze these patterns, the peaks should first be labeled according to an expected structure. This results in a set of equations

$$\begin{cases} |k_1\mathbf{a_k} + l_1\mathbf{a_k} + m_1\mathbf{c_k}| = Q_1 \\ |k_2\mathbf{a_k} + l_2\mathbf{b_k} + m_2\mathbf{c_k}| = Q_2 \\ |k_3\mathbf{a_k} + l_3\mathbf{b_k} + m_3\mathbf{c_k}| = Q_3 \\ \qquad\qquad\vdots \end{cases} \qquad \text{(Eq 3.1)}$$

where $\mathbf{a_k}$, $\mathbf{b_k}$, and $\mathbf{c_k}$ are a set of reciprocal lattice vectors and $k_i$, $l_i$ and $m_i$ are the indices assigned to label the peaks measured at $Q_i$. This set of equations is then solved by a mean square minimization technique for the reciprocal lattice vectors, which in return yield the lattice parameters.

In the GIXD experiments conducted [2], only a monolayer-thick film covered the sample. This means that $\mathbf{c_k}$ approaches zero in equation 3.1, leaving $\mathbf{a_k}$ and $\mathbf{b_k}$ to be solved. Figure 3.1 shows a generic real space 2D lattice, specified by the lattice parameters $a$, $b$ and $\gamma$, requiring 3 equations for exact solutions. Usually, additional equations were required for peak assignment verification. Since this study did not enjoy the luxury of having large number of peaks, theoretical calculations were employed to overcome the deficiencies. In this section, the GIXD data are shown and briefly discussed.

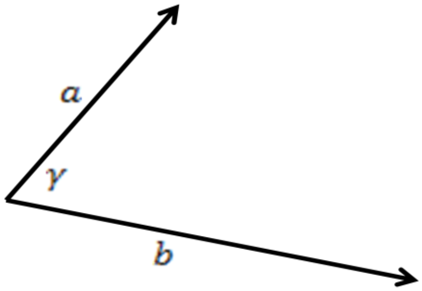

Figure 3.1, a generic real space 2D lattice.

### 3.2.1 $T_4C_{11}Si(EtO)_3$ monolayer on silicon

Figure 3.2 shows the GIXD pattern of a $T_4C_{11}Si(EtO)_3$ Langmuir Blodgett (LB) monolayer deposited on a silicon substrate. Relative peak intensities were color-coded. Sharp, distinct peaks could be visibly observed in this pattern, suggesting relatively large grains of crystals and a high degree of texturing.

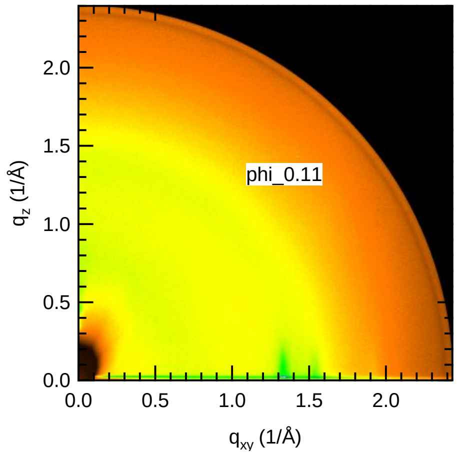

Figure 3.2, GIXD pattern of $T_4C_{11}Si(EtO)_3$ LB monolayer on a silicon substrate.

### 3.2.2 $T_4C_{11}SH$ monolayer on sputtered gold

Figure 3.3 shows the GIXD pattern of a $T_4C_{11}SH$ monolayer deposited on a sputtered gold surface. Peaks could again be observed, although with reduced distinctness as compared to those in figure 3.2.

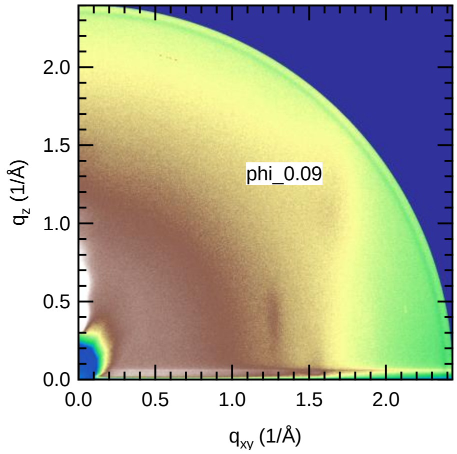

Figure 3.3, GIXD pattern of $T_4C_{11}SH$ monolayer on sputtered gold surface.

In addition, peak positions described the morphology of the monolayer being examined. Both the horizontal and the vertical axes were in reciprocal lattice space. By indexing the peaks according to an expected lattice structure, the lattice parameters could be extracted from equation 3.1. It was observed that, in figure 3.3, the peak at $Q_{xy} \approx 1.3$ was shifted to a nonzero $Q_z$ value. This suggested that the morphology of the $T_4C_{11}$ monolayer was dependent on the binding group as well as the substrate.

### 3.2.3 $T_4C_{11}SH$ monolayer on evaporated gold

Figure 3.4 shows the GIXD pattern of a $T_4C_{11}SH$ monolayer deposited on an evaporated gold surface. The roughness of this surface was studied through atomic force microscopy (AFM), as shown in the previous chapter, and was found to be significantly rougher than the sputtered gold surface. Peaks were nonetheless still visible in figure 3.4. The peak stayed at approximately the same positions as those found in figure 3.3. These suggested an attenuation in the crystallinity of the monolayer resulting from the increased substrate roughness, however the intrinsic crystal structure remained unchanged. Modeling the $T_4C_{11}SH$ monolayer formed in the demonstrated DI-mFET with the parameters extracted from the crisper, and hence more accurate, figure 3.3 would be valid.

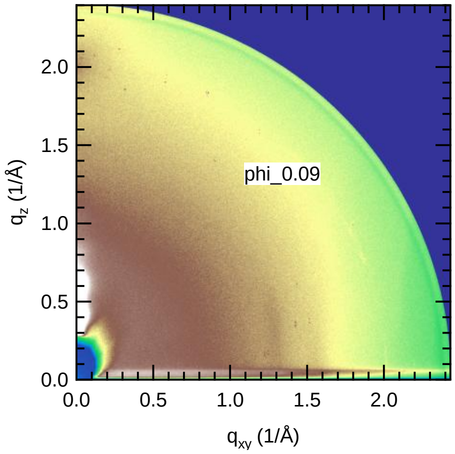

Figure 3.4, GIXD pattern of $T_4C_{11}SH$ monolayer on evaporated gold surface. The 11 and 02 peaks are barely visible while the 12 peak can not be resolved from this figure. However, sections of this plot reveal all 11, 02 and 12 peaks.

Just as in many organic crystals, the $T_4C_{11}SH$ monolayer was believed to be packed in the so-called herringbone packing motif [3]. Therefore, the first peak was labeled as 11, second as 02 and third as 12. After correcting for the background and solving equation 3.1 according to this labeling scheme using the least square error fit, the following in-plane lattice parameters were obtained.

$a$ = 5.933Å

$b$ = 7.874 Å

$\gamma = 89.93^o$

Furthermore, the 11 and 12 peaks strayed away from the $Q_z = 0$ axis. This suggested that the molecules tilted away from the normal perpendicular to the surface. By solving

$$Q_z = \overrightarrow{Q_{ab}} \cdot \hat{e} \tan(\theta_{\text{tilt}}) \qquad \text{(Eq 3.2)}$$

where $\overrightarrow{Q_{ab}}$ was the reciprocal lattice vector pointing in the $\mathbf{a_k}$ and $\mathbf{b_k}$ direction, the tilt angle was found to be about $15^o$ [4]. This agreed reasonably well with the tilt angle estimated from a near edge X-ray absorption fine structure (NEXAFS) study [5], which was $20^o$. However, it should be noted that the tilt angle extracted from GIXD only corresponded to the tilt of the molecule which contributed to the GIXD pattern, i.e. only the molecules in the small crystallites, whereas the estimate from NEXAFS was an average of all molecules interrogated within the spot-size.

## 3.3 Modeling and discussions

As mentioned, a major deficiency in the above analysis was that there were only 3 peaks providing 3 equations to solve for the 3 unknowns. Although a set of solutions was guaranteed, it was impossible to verify whether the labeling scheme was done correctly. Furthermore, although a tilt angle of $15^o$ was estimated from the GIXD data, it was not clear which part of the $T_4C_{11}SH$ molecule was tilting by this angle, due to the presence of a kink where the $T_4$ and $C_{11}$ connected. Additionally, the GIXD study did not inform why the $T_4C_{11}SH$ molecules tilted.

To support the hypothesis proposed and to model the monolayer better, a first principles study was carried out to answer the listed questions. This was done by packing two $T_4C_{11}SH$ molecules in a periodically repeating unit cell defined by *a*, *b*, and $\gamma$, as extracted from the above analysis. Although Van der Waal's (VdW) force was expected to significantly contribute to the total energy of these loosely bounded systems, total energy calculations were performed under the constraints that the lattice parameters were fixed at the extracted values. This helped mitigate the absence of VdW force in the DFT formalism [6] and allowed an investigation into how the total energy varied with different structures.

The calculations were performed with Vienna Ab-initio Software Package (VASP) [7,8] in which the wavefunctions were expanded in plane-wave basis sets and the core electroncs were replaced by projector augmented wave (PAW) pseudopotentials. The generalized gradient approximation (GGA) with Perdew-Burke Enzerhof (PBE) parameterization [9] for the exchange-correlation functional was chosen instead of local density approximation (LDA) to obtain more accurate results. For most of the calculations, $\Gamma$-point sampling was found to be sufficient to describe the system. Larger k-point samplings had been done to support this claim.

In the following, the $T_4C_{11}SH$ monolayer will be shown to pack in the so-called herringbone packing motif to support the experimental work presented above. The origin of the $15^o$ tilt of the molecule will also be explored. An appropriate model for the monolayer is developed and a prediction of additional peaks to be investigated in the future is made.

### 3.3.1 Face-to-face vs. edge-to-face packing scheme

The top views of face-to-face (f2f) and edge-to-face (e2f) packing scheme are shown in figure 3.5. In order for the molecules to pack as e2f, one of the two molecules in the unit cell must be rotated. However, complications arose when the molecule underwent rigid rotations as this inevitably resulted in the alkane tails crossing with its neighboring molecules. This could be avoided if only the thiophenes of the molecule were rotated while the alkane remained fixed. Therefore, for e2f to be more favorable than f2f, the energy barrier of this rotation must be small.

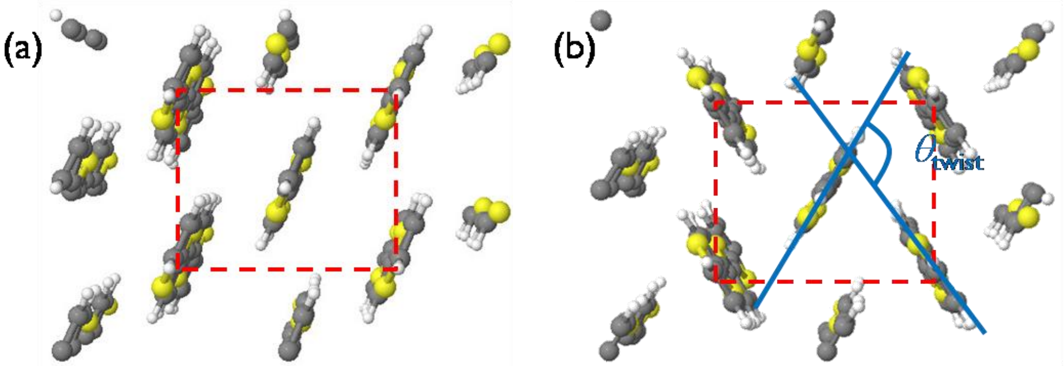

Figure 3.5, top views of (a) face-to-face (f2f) packing scheme and (b) edge-to-face (e2f) packing scheme. The red dotted rectangle designates a unit cell. The angle formed and defined in (b) is $\theta_{twist}$.

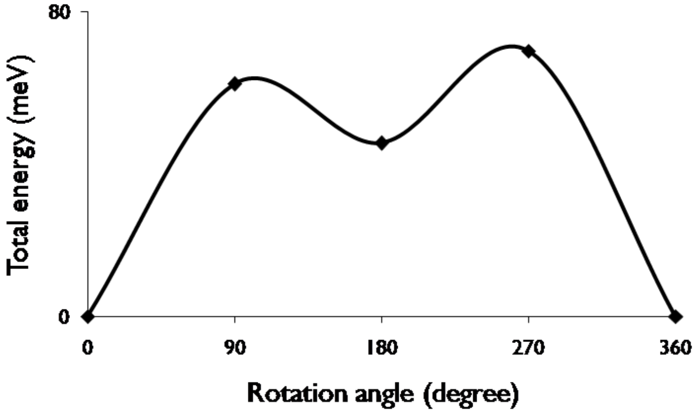

Figure 3.6, total energy versus rotation angle of the thiophenes about the long axis of the thiophenes, with the alkane tail frozen in an isolated molecule state.

Figure 3.6 shows the total energy versus the rotation of the thiophenes, with the alkane tail frozen in an isolated $T_4C_{11}SH$ molecule. The $0^o$ rotation angle corresponds to a starting configuration where an isolated $T_4C_{11}SH$ molecule had been fully relaxed. The thiophenes were rotated about the vector parallel to its long axis, in the clockwise direction. We can see from figure 3.6 that the total energy differences between the chosen configurations were only on the order of 10meV. This was approaching the energy resolution of the rough calculations performed. This meant that the energy barrier preventing the thiophenes from rotating was negligible and thus would not pose an obstacle to the e2f packing scheme.

To predict the packing scheme of the $T_4C_{11}SH$ monolayer, two $T_4C_{11}SH$ molecules were placed in a periodically repeating unit cell, with the previously defined constraints. The two molecules were placed at $(0,0)$ and $\left(\frac{1}{2},\frac{1}{2}\right)$ position for symmetry. As shown in figure 3.5, there was no obvious reason for the distance between neighbor molecules to be different. In addition, in figure 3.5, we further define $\theta_{twist}$ as the angle formed by the two thiophenes from the two molecules inside a unit cell. By definition, when $\theta_{twist}$ equaled $0^o$, the packing scheme was f2f; otherwise, the packing scheme was e2f of different angle.

Figure 3.7 presents the results of the ion relaxation process of the molecules in the constrained unit cells with different initial configurations. It shows how the total energy and $\theta_{twist}$ evolved as the ion relaxation process proceeded. It could be seen that the molecules favored the e2f packing scheme with a $\theta_{twist} \approx 120^o$, which yielded the lowest total energy. Interestingly, the calculations predicted that all initial configurations, except for the one setup as f2f at the beginning, would eventually converge to this lowest energy configuration if enough relaxation steps were given. From this, it could be concluded that the total energy differences between the $\theta_{twist} = 120^o$ configuration, as shown in figure 3.7, and other initial configurations were significant, resulting in large force pushing the ions to this global minimum.

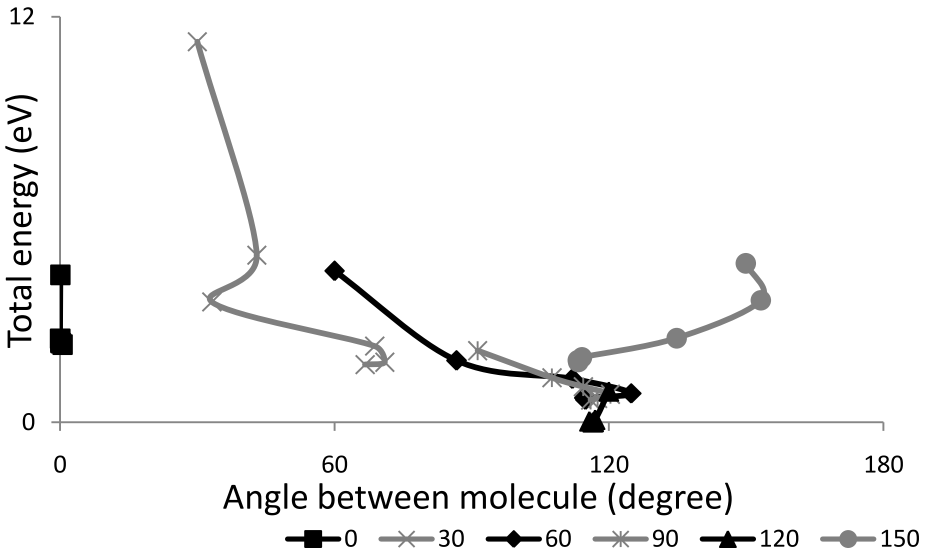

Figure 3.7, energy and $\theta_{twist}$ evolution as the ion relaxation process proceeds for different initial configurations.

The f2f configuration remained more or less unaltered during the entire relaxation process. This evidenced that the f2f configuration was a stable local minimum. However, if enough perturbations were given, the structure should probably fall towards the global minimum of the $\theta_{twist} = 120^o$ e2f packing scheme.

## 3.3.2 Tilt of the molecule

In addition to the lattice parameters extracted in the previous section, the GIXD data also provided further suggestions that the molecules tilted away from the normal of the substrate surface as explained above. Inspecting the GIXD data closer, it could be seen that among the three observed peaks, 11 and 12 strayed away from $Q_z = 0$, while 02 remained. This hinted that the molecule was tilting towards the short axis, *a*. By calculating the diffraction pattern, it could be confirmed as tilting the molecule towards the long axis, *b*, could not possibly match the GIXD pattern obtained experimentally, as the 02 peak would be driven to some non-zero $Q_z$ position.

In order to understand why the $T_4C_{11}SH$ molecules tilted, the total energies needed to be partitioned between the contributions from the thiophenes and the alkane tails. The changes in energies from these components are plotted in figure 3.8 against $\theta_{tilt}$. The plot shows that the energy contributing from the thiophenes increased when $\theta_{tilt}$ increased from zero while that from the alkane tails increased first and decreased eventually. This trend could be understood from the change in inter-planar distance of the two segments with the neighboring molecules. As $\theta_{tilt}$ increased from $0^o$, the inter-planar distance between the thiophenes decreased. This led to an increase in the total energy contributed from this segment, as the thiophenes were interacting stronger with their neighbors. Opposite trends were observed for the alkane tails.

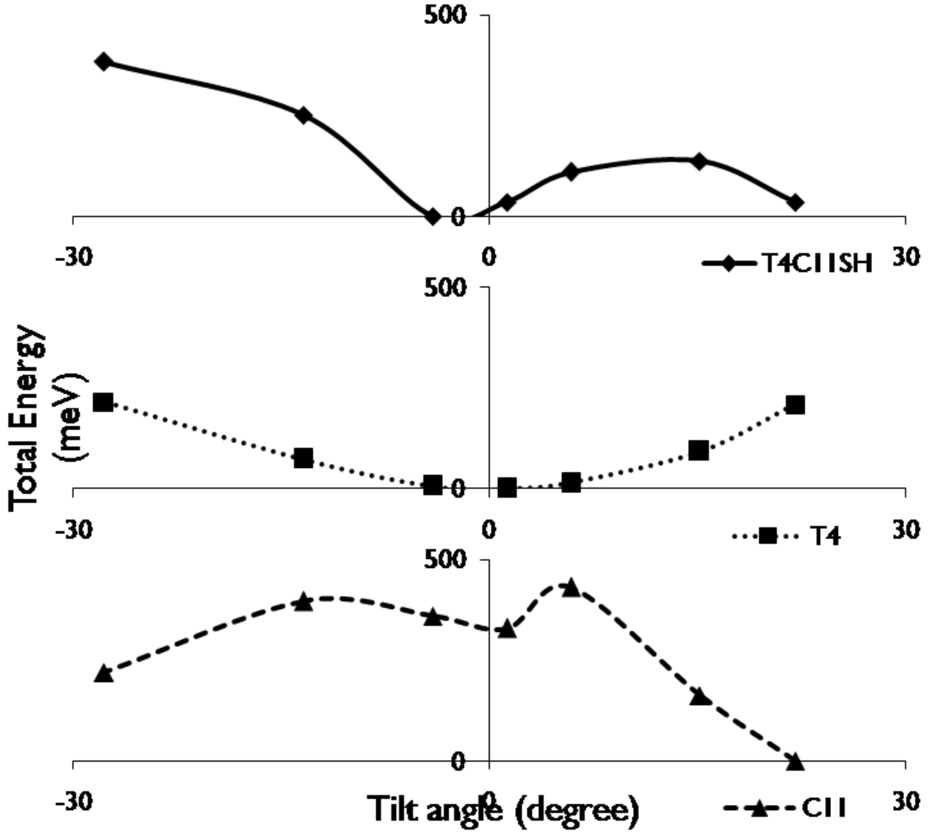

Figure 3.8, total energy of the (top) entire $T_4C_{11}SH$ molecule, (middle) contribution from the $T_4$ only and (bottom) from the $C_{11}SH$ only, as $\theta_{tilt}$ varies.

As shown in figure 3.2, figure 3.3 and figure 3.4, the morphology of the monolayer depended upon the binding group as well as the substrate. Without including the substrate in these calculations in order to reduce the computational complexity, the optimal $\theta_{tilt}$ was not predicted and compared to the experimentally obtained $15^{\circ}$. Nevertheless, this study explained the tilting of the molecules.

### 3.3.3 Calculated XRD patterns and the amorphosity of the monolayer

Given the atomic coordinates and the lattice parameters, the structure factor of a system could be calculated by simply taking a discrete Fourier transform [10],

$$S(k) = \sum_n^N f_n e^{-2\pi i \mathbf{k}\cdot\mathbf{r_n}} \qquad \text{(Eq 3.3)}$$

where $f_n$ was the atomic form factor and $r_n$ was the atomic coordinates. However, naively taking the Fourier transform in this straight forward manner would result in a diffraction pattern that does not match with the experimentally obtained GIXD pattern. By decomposing the calculated X-ray diffraction (XRD) pattern into one that was derived from the $T_4$ and another solely from $C_{11}$, figure 3.9 was obtained.

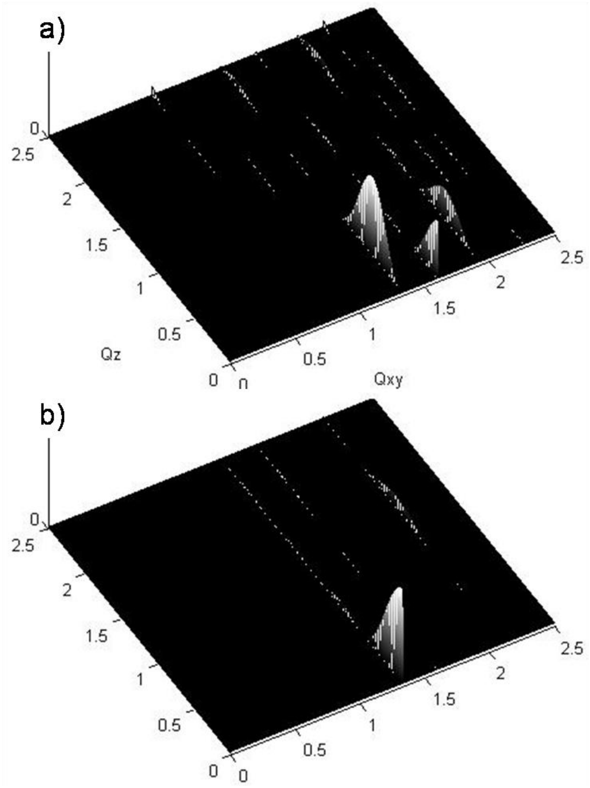

Figure 3.9, calculated XRD pattern from (a) thiophenes only and (b) alkane only.

While, as shown in figure 3.9b, a large peak at the 11 position was sitting on the $Q_z$ = 0 axis, this was not observed in the experimentally obtained GIXD data. This led to a hypothesis that the $C_{11}$ layer was amorphous, which was reinforced by the following observations. Firstly, while the lattice constants extracted were optimal for the thiophenes, they were too large for an alkane monolayer. This meant that the $C_{11}$ layer [11] was under substantial tensile stress if crystallinity was to be maintained. Additionally, the extracted in-plane lattice parameters could not fit with hollow sites on the gold (111) surface, which were the favorable sites for the alkyl-thiols to bind to as reported in reference [12].

### 3.3.4 A prediction of new peaks

As the evidence from previous experiments and calculations pointed out, the alkane tail layer was amorphous. Therefore attempting to model the $T_4C_{11}SH$ with a repeating unit cell was unreasonable. Although there had been reports of using first principles calculations to understand amorphous materials and defects [11], in general, these required constructions of large super-cells, containing hundreds or even thousands of replicas of the primitive unit cell. For inorganic crystals like silicon, this was still possible as a primitive unit cell contained only two silicon atoms, but for $T_4C_{11}SH$, the number of atoms to be included in a super-cell would be prohibitively large, leading to calculations that would be beyond the scope of this thesis.

As a result, XRD patterns were calculated with the alkane tail completely ignored. By varying $\theta_{tilt}$, an XRD pattern with good agreements in $Q_{xy}$ and $Q_z$ for all three observed peaks was obtained, as shown in figure 3.11. This was achieved by tilting the thiophene towards the short axis by 15°. Lorentz factor, polarization factor and the multiplicity [13] were all included in generating figure 3.11.

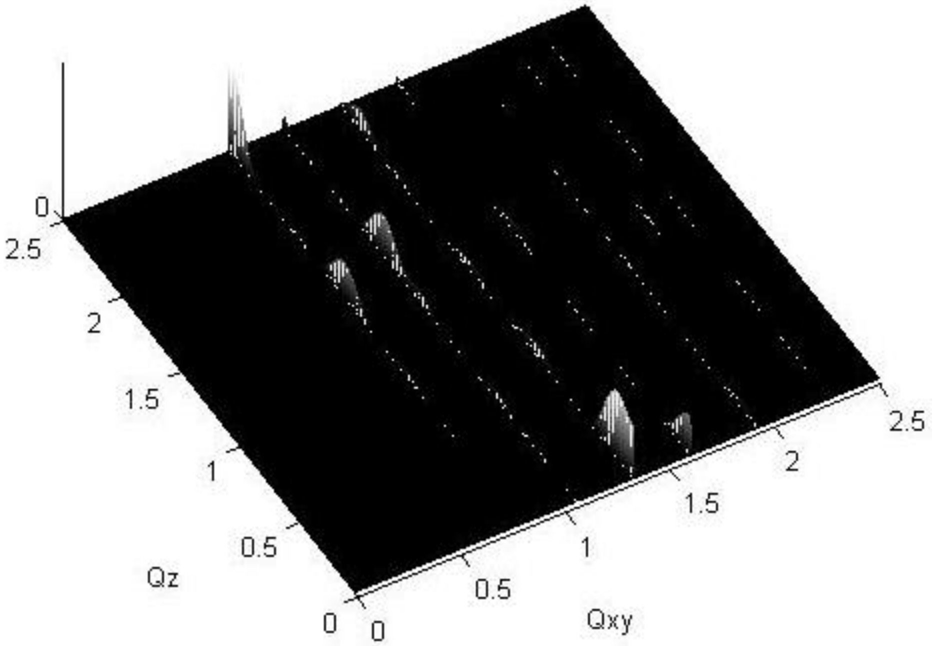

Figure 3.11, calculated XRD pattern from the atomic coordinates that is solely comprised of the thiophenes, tilted towards the short axis by 15°. Lorentz factor, polarization factor and the multiplicity are all included

This construct guaranteed an exact agreement in $Q_{xy}$ as the calculated XRD pattern used the extracted lattice parameters. However, the independent agreement in the $Q_z$ position and the relative intensities of the peaks suggested that this set of atomic coordinates modeled the experimentally probed $T_4C_{11}SH$ monolayer well. Furthermore, in addition to the 11, 02 and 12 peaks observed and predicted using GIXD and the calculated XRD pattern respectively, there were several additional peaks scattered throughout the calculated XRD pattern. They suggested where careful scans should be performed in future experiments. Lastly, the peaks in the calculated XRD pattern were infinitely sharp in $Q_{xy}$. This was because of the discrete Fourier transform taken, which implicitly implied an infinite periodic structure. A more realistic broadening of the peaks could be obtained by taking a continuous Fourier transform on a construct with a finite number of replicas of the unit cell. However, the complexity of the Fourier transform operation grows as a cubic function of the k-points involved and a linear function of the number of atoms in the construct, therefore, the calculation would become very resource-demanding. Furthermore, the broadening of the peaks in the GIXD data was approaching the resolution limit of the equipment. Hence, the width of the peaks experimentally observed in the GIXD data should only be taken qualitatively. As a result, there was no attempt matching the size of the crystallites in the monolayer.

## 3.4 Summary

In this chapter, alkyl-thiophene monolayers were examined thoroughly experimentally with GIXD and theoretically with first principles calculations based on DFT. Peaks from the GIXD data suggested the in-plane lattice parameters of the monolayer. However, with only three peaks solving for three unknowns, first principles calculations were called for to enrich the physical understanding of the $T_4C_{11}SH$ monolayer. Given the constraints on the lattice parameters, calculations performed revealed the e2f configuration, with a $\theta_{twist} = 120^o$. Additional calculations revealed that the tilt of the molecule away from the normal to the surface of the substrate originated from the competing trends in total energies of the two segments of the molecule. As the tilt angle, $\theta_{tilt}$, increased, the inter-planar distance between neighboring thiophenes decreased while that between alkane tails increased. This led to a change in total energies in opposite directions. However, due to the lack of a substrate and the amorphous nature of the layer of the alkane tail, which was hinted from the missing 11 peak at $Q_z = 0$, the model of crystalline $T_4C_{11}SH$ could not predict $\theta_{tilt}$ accurately. Nevertheless, a calculated diffraction pattern using only the thiophenes, with a $\theta_{tilt} = 15^o$, was generated and matched the experimentally obtained GIXD pattern very well. This calculated pattern could guide future experiments as to where to probe more carefully for additional peaks and also could serve as a benchmark for a monolayer with a perfectly crystalline thiophene layer.

# Supplemental information

The supplemental information provided in this section includes the MATLAB code used to compute the Fourier transform of the atomic coordinates to arrive at the calculated XRD pattern.

## S3.1 MATLAB code

The following code was used to obtain the calculated XRD pattern given a set of atomic coordinate, “A”. The input variable “dim” was the in-plane lattice constants [*a*, *b*] corrected for $\gamma$.

```
function [fA fAcorr]=XRD_Qxy(A,dim,kmax,kz,res)

qmax=kmax*res;                %max qxy
len=size(A);                  %number of atoms
ka=1/dim(1); kb=1/dim(2);     %reciprocal vectors
fA=zeros(1,kmax*res+1);       %zeroing the spectrum
fAcorr=zeros(1,kmax*res+1);   %zeroing polarization factor

% constant declarations
detector_dist=392.8;
pixel_width=0.150;
wavelength=0.9736;
center_x=1149;
center_y=1147;
ph=0.98;

for i=1:len(1)
    for k1=1:kmax+1
    for k2=1:kmax+1
    %checking out of range
        klen=(((k1-1)*ka)^2+((k2-1)*kb)^2)^0.5*2*pi*res;
       if (klen>qmax)
           continue;
       end;
        % k dot r
       kr=dot([(k1-1)*ka (k2-1)*kb],A(i,2:3))+kz*A(i,1);
        % summation of exponent of (2 pi i) times (k dot r)
        fA(floor(klen)+1)=fA(floor(klen)+1)+A(i,4)*
           exp(-2*pi*j*kr);
    end;
```

```
    end;
end;

for k1=1:kmax+1
for k2=1:kmax+1
    %checking out of range
    klen=(((k1-1)*ka)^2+((k2-1)*kb)^2)^0.5*2*pi*res;
    if (klen>qmax)
        continue;
    end;
    % multiplicity
    if (k1==k2)
        mul=2;
    else
        mul=1;
    end;

    % pcorr term
    rel_j=(klen+1)/((kmax*res)+1)*2300-center_x;
    rel_i=kz/((kmax*res)+1)*2300-center_y;
    leg1square=(rel_j*pixel_width)^2+detector_dist^2;
    singammasquare=((rel_j*pixel_width)^2)/(leg1square);
    leg2square=(rel_i*pixel_width)^2+leg1square;
    cosdeltasquare=leg1square/leg2square;
    sindeltasquare=((rel_i*pixel_width)^2)/(leg2square);
    pcorr=ph*(1-singammasquare*cosdeltasquare)+(1-ph)*
           (1-sindeltasquare);

    % Lorentz term
    if ((k1==1) && (k2==1))
        lorentz=1;
    else
        lorentz=1/((((k1-1)*ka)^2+((k2-1)*kb)^2+kz^2)^0.5*2*pi);
    end;

    %correction = Lorentz / Polarization * Multiplicity
    fAcorr(floor(klen)+1)=lorentz/pcorr*mul;
end;
end;
```

# References

[1] Le Comber, P. G.; Spear, W. E., "Electronic transport in amorphous silicon films," *Phys. Rev. Lett.*, *24*, **1970**, 509-511

[2] The grazing incidence X-ray diffraction work was performed by Dr. Kanan Puntambekar at Stanford Synchrotron Radiation Laboratory (SSRL) with the help of Dr. Mike Toney. The data was included in this thesis for completeness of the analysis.

[3] Campbell, R. B.; Trotter, J.; Monteath, J., "Crystal structure of hexacene, and a revision of crystallographic data for tetracene and pentacene," *Acta. Cryst.*, *15*, **1962**, 289-290

[4] Fritz, S. E., "Structure and transport in organic semiconductor thin films," Ph.D. Dissertation, University of Minnesota, **2006**

[5] The NEXAFS work was not discussed in this thesis.

[6] Dion, M.; Rydberg, H.; Schroder, E.; Langreth, D. C.; Lundqvist, B. I., "Van der Waals density functional for general geometries," *Phys. Rev. Lett.*, *92*, **2004**, 246401

[7] Kresse, G.; Furthmuller, J., "Efficiency of ab-initio total energy calculations for metals and semiconductors using a plane-wave basis set," *Comput. Mater. Sci., 6*, **1996**, 15

[8] Kresse, G.; Furthmuller, J., "Efficient iterative schemes for ab initio total-energy calculations using a plane-wave basis set," *Phys. Rev. B*, *54*, **1996**, 11169

[9] Perdew, J. P.; Burke, K.; Wang, Y., "Generalized gradient approximation for the exchange-correlation hole of a many-electron system," *Phys. Rev. B*, *54*, **1996**, 16533-16539

[10] Kittel, C., Introduction to solid state physics 7th edition, Wiley, **1995**

[11] Love, J. C.; Estroff, L. A.; Kriebel, J. K.; Nuzzo, R. G.; Whitesides, G. M., "Self-assembled monolayers of thiolates on metals as a form of nanotechnology," *Chem. Rev.*, *105*, **2005**, 1103-1169

[12] Justo, J. F.; Bazant, M. Z.; Kaxiras, E.; Bulatov, V. V.; Yip, S., "Interatomic potential for silicon defects and disordered phases," *Phys. Rev. B*, *58*, **1998**, 2539-2550

[13] Fultz, B.; Howe, J. M., Transmission electron microscopy and diffractometry of materials 2nd edition, Sprinter-Verlag, **2001**

# Chapter 4

# Theoretical study of [2]rotaxane

While the initial demonstration of the [2]rotaxane memory showed promising results, the underlying principles of how this complex molecule operated was still mostly unanswered. Topics like whether the cyclobis(paraquat-p-phenylene) tetra-cation (CBPQT) ring did shuttle between the tetrathiafulvalene (TTF) and the dioxynaphthalene (DNP) units and how this switching occurred were intensely debated. In this chapter, the technique of total energy calculation employed in previous chapters was used again to further our physical understandings of this molecular machine from the first principles.

## 4.1 Motivations

In 2002, Heath and Stoddart reported the demonstration of the first molecular memory in a crossbar molecular memory structure as shown schematically in figure 4.1 [1]. A monolayer of [2]rotaxane was sandwiched between a titanium/aluminum top electrode and a n-type silicon bottom electrode at each junction. Figure 4.2a shows the several versions of catenanes and rotaxanes used in their experiments. This work focused on the rightmost molecule in figure 4.2a. In particular, to simplify the calculations, the top sacrificial capping group and the bottom binding group were ignored. Figure 4.2b depicts a cartoon of the low-conductance OFF-state of the [2]rotaxane molecule, where the CBPQT-ring was at the TTF unit; figure 4.2c portrays the high-conductance ON-state, with the CBPQT-ring residing near the DNP unit. It had been hypothesized that the ring would traverse from the TTF site to the DNP site when a +2V bias was applied on the n-type silicon bottom electrode, switching the molecule from OFF- to ON-state [1]. Hysteresis curves and tens of cycles of repeated switching were measured. The interesting device prompted further investigation of this molecule. As probing this nano-structure was formidably challenging, theoretical approaches were taken. The performance of this molecule had been studied in terms of its conductance [2], packing density [3, 4], ionization potentials [5], and, the density of states (DOS) [5]. A mechanism of how this molecule would switch between its two stable co-conformations was proposed [5].

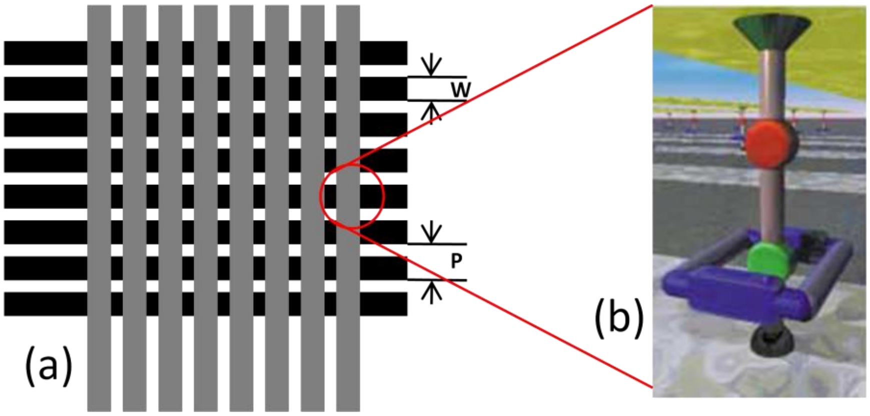

Figure 4.1, (a) a schematics of a crossbar molecular memory array. The width and pitch are defined as W and P shown in the figure. (b) A cartoon illustration of the [2]rotaxane molecule sandwiched between the two electrode (after [1]).

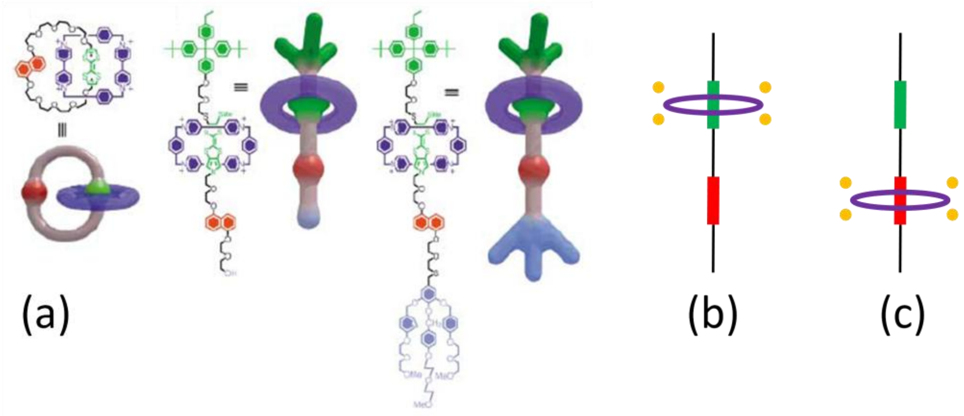

Figure 4.2, cartoon illustrations of the [2]rotaxane molecule. (a) Several different versions of the [2]catenanes and the [2]rotaxane molecules, after [1]. The [2]rotaxane molecule is mainly composed of a backbone and a encircling cyclobis(paraquat-*p*-phenylene) (CBPQT-) ring. The tetrathiafulvalene (TTF) unit is highlighted green and the dioxynaphthalene (DNP) unit red in this figure. In addition to these major components, the [2]rotaxane molecule also consists of a sacrificial segment (also highlighted in green in the figure) at the very top and a binding moiety (light blue) at the very bottom. (b) shows simplistic description of the OFF-state, where the CBPQT-ring is sitting at the TTF site, and (c) shows the ON-state, where the ring has moved to the DNP site. Notice that there are four orange dots in (b) and (c). They correspond to the four $PF_6^-$ counter-ions that reside in the vicinity of the [2]rotaxane molecule.

However, one of the most important figures of merit, the switching speed, had never been reported, experimentally nor theoretically. An estimation of this parameter, using information from first principles, is the main goal of this chapter. In addition, this work also reports a detailed study of the electronic and structural properties of the [2]rotaxane molecule that enhances the physical understanding known from the existing literature.

## 4.2 Methodology

First principles calculations were performed with Vienna Ab-initio Software Package (VASP) [6, 7]. The generalized gradient approximation (GGA) was used to better model the physics of the molecular structure with the Perdew-Burke-Enzerhof (PBE) parameterization [8]. In VASP, wavefunctions were expanded in plane-wave basis sets and projector augmented wave (PAW) pseudopotentials replaced the core electrons. Single k-point ($\Gamma$-point) sampling was performed and was found to be sufficient as the molecules were not too closely packed. The [2]rotaxane molecule and its four accompanying counter-ions, a total of 174 atoms, were centered in a 20Å×20Å×45Å cell that periodically repeated in all three dimensions. The repeating cells allowed the inclusion of lateral inter-cell interactions, as would be expected to be present in a monolayer structure.

With an interpolated trajectory of the CBPQT-ring along the backbone, an energy landscape could be mapped out by calculating the total energy of the different configurations. In addition to the OFF- and ON-states, five intermediate conformations were created and allowed to relax. This led to figure 4.4.

To calculate the ionization potential, it required the total energy of the 1+ state. As the size of [2]rotaxane was too large, a cubic cell could not be implemented due to software limits. Hence, the charged molecule was placed in rectangular boxes with 3 different dimensions, 20Å×20Å×45Å, 20Å×20Å×50Å and 20Å×20Å×55Å, so that an extrapolation to infinite isolation could be made. Furthermore, the center of charge was found by computing the differences in charge densities between the neutral and 1+ states. This parameter was necessary for appropriately evaluating the ionization potential.

By applying an electric field across the unit cell, the dielectric constant was found from the ratio of the external field to the screened field. Plots of dielectric constant as a function of position along the long axis of the [2]rotaxane molecule were generated and the effective dielectric constant was found from equation 4.3. Since these calculated values corresponded to a loosely packed monolayer film, an extrapolation to the experimentally reported surface density was made.

# 4.3 The physical properties

To facilitate the estimation of the switching performance of the [2]rotaxane molecule, some of the physical properties were calculated. In particular, the total energies of this molecule at different configurations were calculated and were used to map out the energy landscape of the “shuttling” reaction of the CBPQT-ring. In light of the previously proposed switching mechanism, which will be elaborated later, the ionization potentials of the [2]rotaxane molecule were also computed. The dielectric constants of the [2]rotaxane molecule at its OFF- and ON-states were also evaluated.

## 4.3.1 The energy landscape

One could view the shuttling of the CBPQT-ring from the TTF to the DNP site as a reaction, in which the OFF-state configuration was the “reactant” and the ON-state was the “product”.

$$\text{OFF-state} \xleftrightarrow{E_a \text{ for ring shuttling}} \text{ON-state}$$

Then, there exists an activation energy, $E_a$, to be overcome before the reaction can go in the forward direction.

To evaluate $E_a$, the overall energy landscape of this “reaction” needed to be mapped. To simplify the analysis, a likely reaction pathway, as shown in figure 4.3 was hypothesized based on the geometry of the backbone and the CBPQT-ring. The intermediate configurations were interpolated from the known atomic coordinates of the OFF- and ON-states. In the first half of this trajectory, the ring traveled from the TTF site to about halfway between the TTF and the DNP sites without any rotation. In the second half, the ring was rotated by 90° about the long axis of the backbone and another 50° about another axis as shown in figure 4.3.

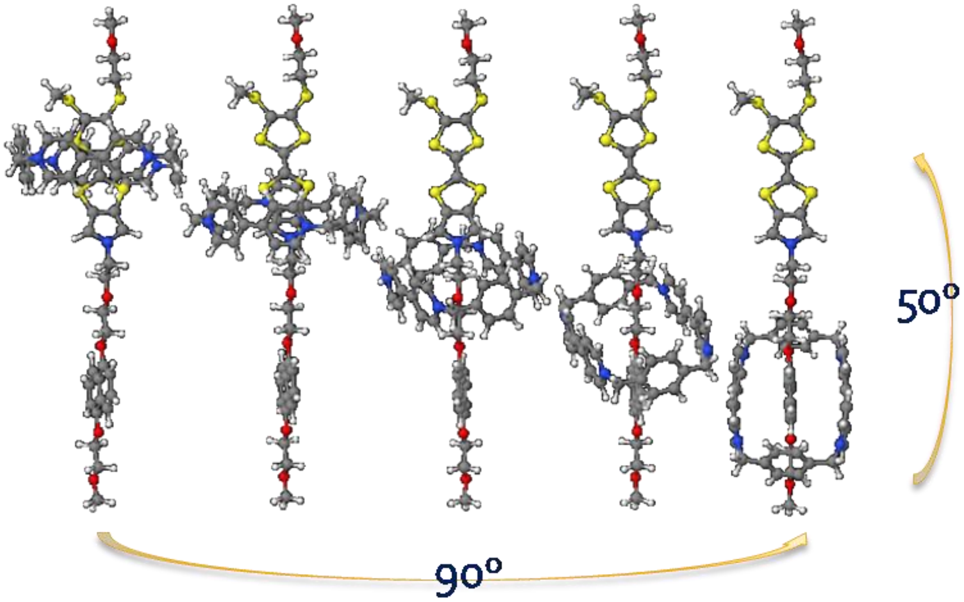

Figure 4.3, the hypothetic trajectory for shuttling of the CBPQT-ring. The ring is rotated by 90° and 50° as shown in the figure while it traverses from the TTF site to the DNP site.

Figure 4.4 shows the energy landscape of the “shuttling” reaction when the CBPQT-ring was traversing from the TTF site to the DNP site as the molecule switched its state. A barrier of about 600meV was separating the two stable states. In addition, the OFF-state had a lower energy than the ON-state, in agreement with experimental reports. Figure 4.5 testifies that these calculations were converged in terms of the total energy, as its inset shows the changes in total energy were on the order of 0.1meV at the end of the ion-relaxation process.

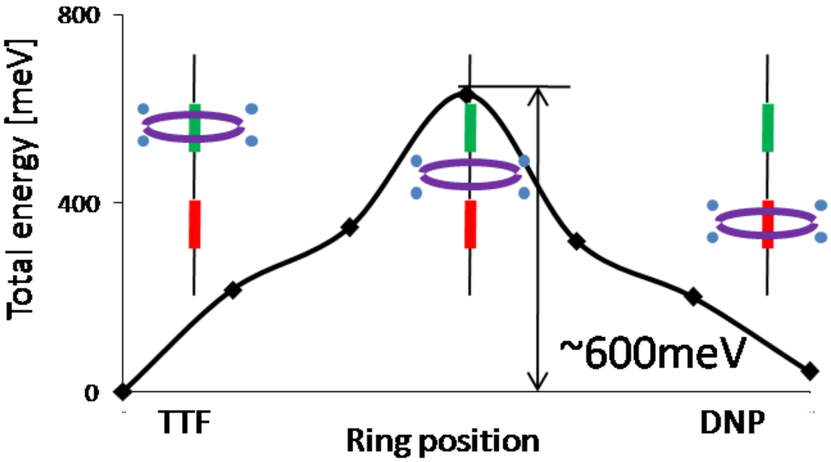

Figure 4.4, the calculated energy landscape of the "shuttling" reaction based on the trajectory displayed in figure 4.3. An activation of about 600meV separates the OFF- and ON-states.

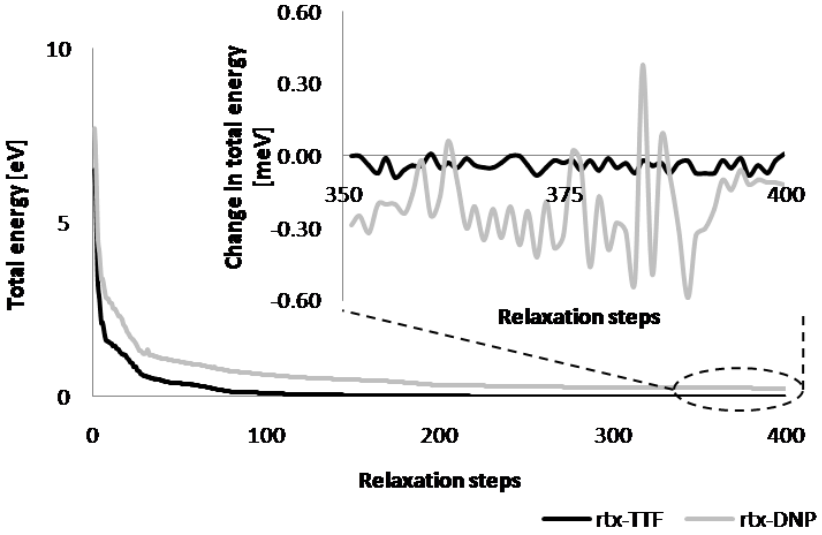

Figure 4.5, total energy of OFF- (black) and ON-state (grey) vs. relaxation steps. Inset shows the changes in total energy at the end of the relaxation process are negligible.

These calculations were performed on a system that included the backbone of the [2]rotaxane molecule, the CBPQT-ring, and four hexafluorophosphate ($PF_6^-$) counter-ions. It was claimed that the CBPQT-ring was in a 4+ charged state and these anions were drafted towards the vicinity of the CBPQT-ring during the synthesis. However, when the [2]rotaxane molecule formed a monolayer, the presence of these counter-ions was uncertain. Firstly, while reference [1] stated that the footprint of the molecule was 140Å$^2$, DeIonno et al. reported that the surface density of the [2]rotaxane molecule in the studied monolayer was as dense as 54Å$^2$/molecule [9]. The high density was hard to reconcile with the size of the molecule itself, even without the counter-ions residing at the corners of the CBPQT-ring. Moreover, strong electrostatic repulsion from neighbor molecules inevitably led to an energetically unfavorable condition. These issues prompted a study of the [2]rotaxane molecule without the presence of the $PF_6^-$.

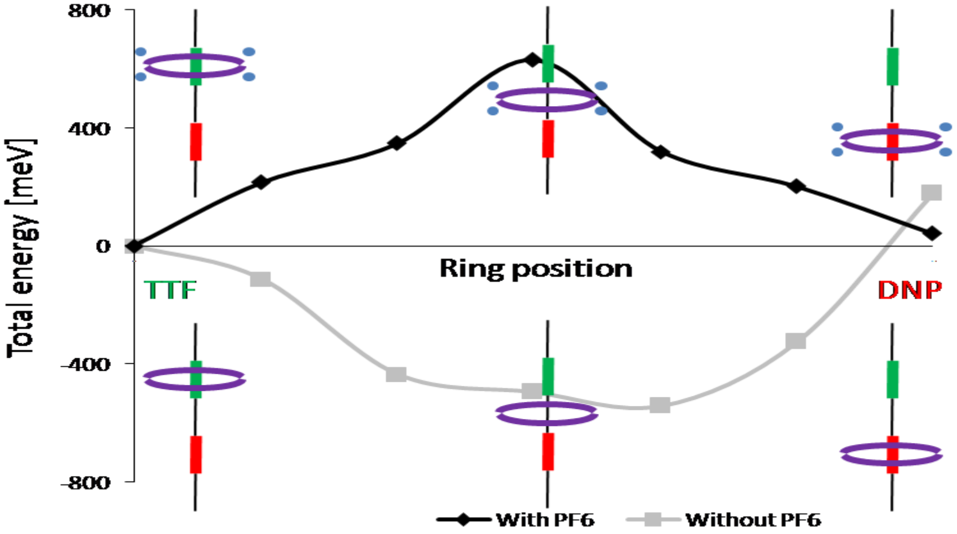

Figure 4.6, energy landscape of the “shuttling” reaction for the [2]rotaxane molecule with and without the $PF_6^-$ counter-ions. It can be readily seen that if the counter-ions are absent, the most stable configuration will have the CBPQT-ring sitting somewhere in the middle and the molecule will not switch at all.

Figure 4.6 shows how the energy landscape was modified should the counter-ions be removed from the system. Although the OFF-state remained lower in energy than the ON-state, obviously, neither of them was not the most stable configuration the molecule could attain. In fact, the lowest energy arrangement would have the CBPQT-ring at about midway between the TTF and the DNP sites and there would be significant barrier to the motions in either direction. In order for the [2]rotaxane molecule to behave as claimed, these counter-ions were needed in the vicinity of the molecule.

However, this did not solve the mystery of how the counter-ions survive the strong electrostatic repulsions among themselves. Further calculations revealed that as the number of counter-ions included increased, the energy barrier got larger. In fact, only one counter-ion per [2]rotaxane molecule would be enough to result in a small energy barrier separating the two states. Nevertheless, the following calculations were still performed with four counter-ions surrounding the [2]rotaxane molecule as specified previously so that the results could be compared to experimental claims.

### 4.3.2 Ionization potentials

According to the previously proposed switching mechanism, the [2]rotaxane molecule, more precisely the TTF unit, was oxidized to 1+ state by an external bias. The positively charged site then repelled the CBPQT-ring to the DNP site. In this picture, the 600meV barrier computed earlier only partially described the activation energy of the "shuttling" reaction. To better capture the role played by charging in the shuttling process, the ionization potentials (IP) of the OFF- and ON-states were computed.

It was well-known that the total energy calculated for a molecule in any given cell size would be different from that for an isolated molecule. Although there existed methods that corrected the total energy for cubic cells, setting up a cubic cell for the [2]rotaxane molecule was impossible due to software limitations. Consequently, a delta self-consistent field (ΔSCF) method [10] with different box size was used to determine the gas phase first and second IPs of the [2]rotaxane molecule.

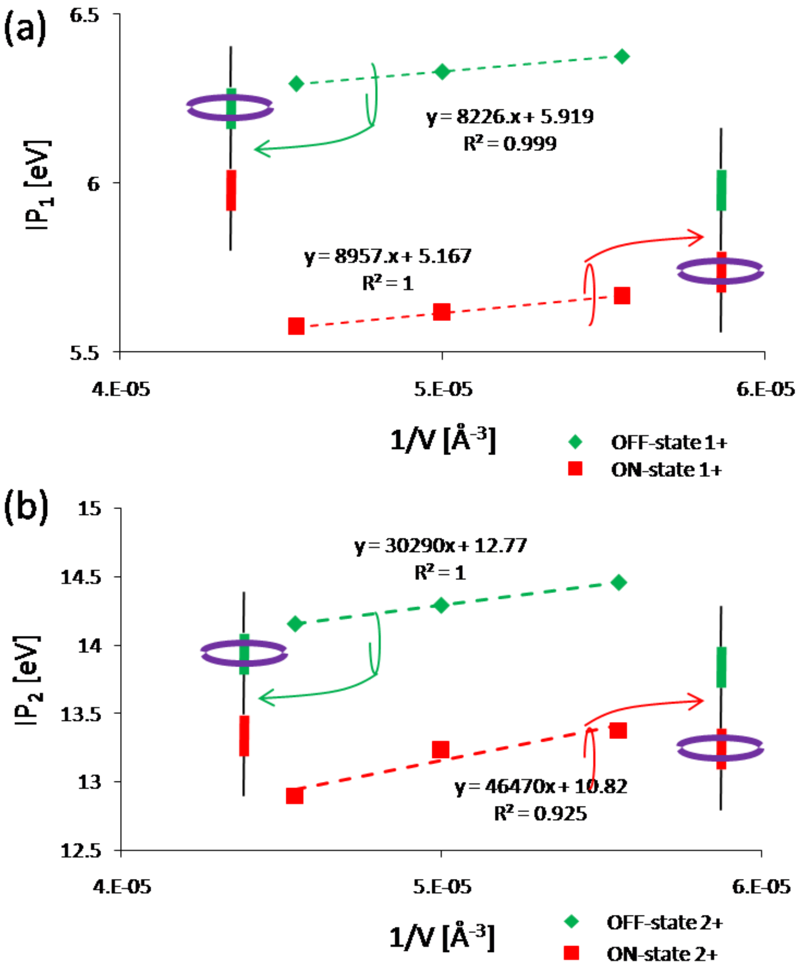

Figure 4.7, the extrapolation of the (a) first IP and (b) second IP of the OFF- and ON-state of the [2]rotaxane molecule.

Figure 4.7 shows the results of the calculations. Extrapolating these trends to an infinitely large box, the IPs were found to be

$IP_1(OFF) = 5.9eV$ $IP_1(ON) = 5.2eV$

$IP_2(OFF) = 12.8eV$ $IP_2(ON) = 10.8eV$

Note that this method was also applied to calculate the IP of benzene and resulted in about 9.6eV, agreeing with the experimental value very well [11]. This is detailed in the supplemental information section of this chapter.

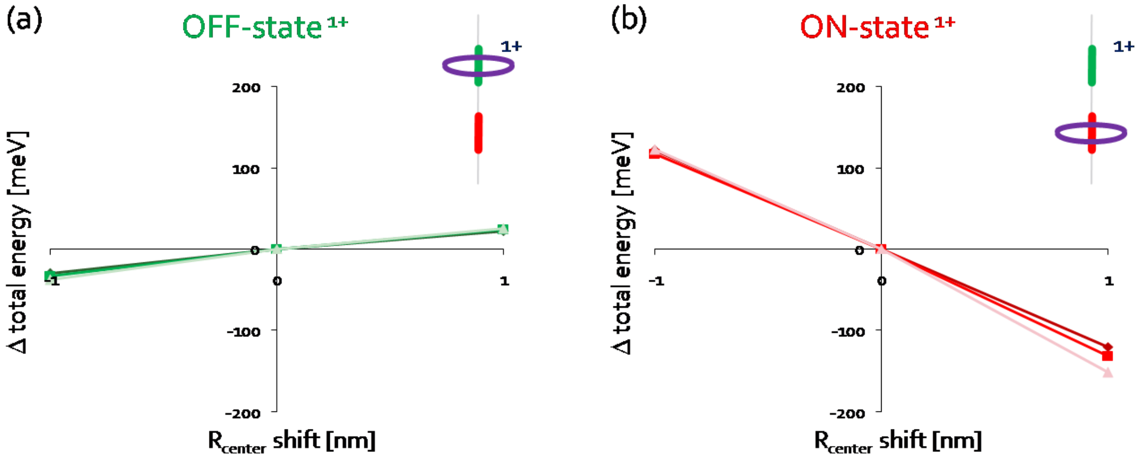

Figure 4.8, dependence of calculated IP on position of the center of charge in (a) the OFF-state configuration and (b) the ON-state configuration.

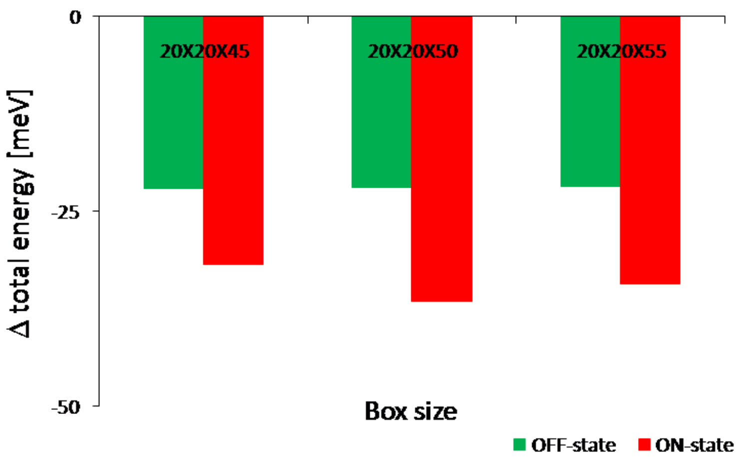

Figure 4.9, effect on calculated IP due to the inclusion of spin-polarization.

It was also known that the position of the center of charge could affect the calculated IP in this method. In the [2]rotaxane system, the center of charge was determined from the difference in charge distribution between the neutral state and the charged state. Due to the finite mesh size in the implementation, there could be finite error in the position determined. However, figure 4.8 shows that the errors in the calculated IP due to this cause were minute. By moving the center of charge away from the calculated ones for as much as 1Å, the changes in total energies for the charged OFF- and ON-states were about 100meV, which were insignificant to the IP calculated.

Similarly, inclusion of spin-polarization was found to have an insignificant effect, as shown in figure 4.9. Also, image charge interaction between the charged molecule and the electrodes, which were about 3nm away from the 1+ charge, was only about 100meV and thus could also be ignored.

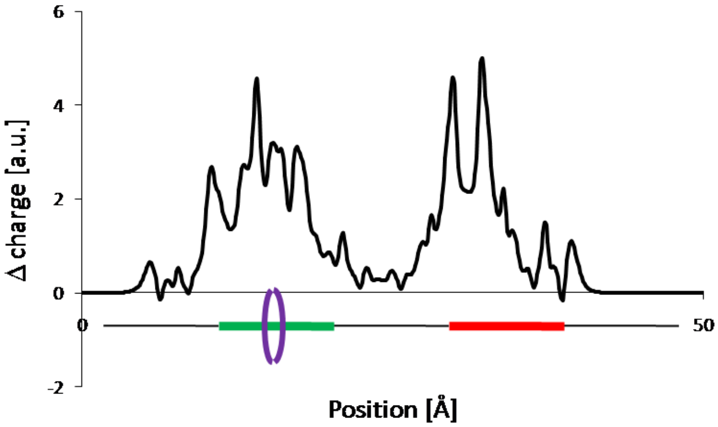

Figure 4.10, the difference in charge distribution, as a function of position in the direction of the long axis of the molecule, between a neutral [2]rotaxane molecule and one that is charged to 1+ state. The atoms are frozen in both calculation and thus the difference seen at both the TTF and the DNP site means that the charging is taking electron away from both sites.

The results presented here differed from those of reference [5], which was computed for each component separately and assumed that the TTF and DNP were weakly interacting. Although this assumption could be valid for other calculations, figure 4.10 shows that it was not appropriate when evaluating IP. This was because when the [2]rotaxane molecule was charged, the electron was not simply taken away from the TTF unit, but a redistribution of the charge density took place over the entire molecule. The consequence of this discrepancy would be discussed below.

### 4.3.3 Dielectric constants

By applying an electric field across a unit cell containing the [2]rotaxane molecule, the "local" dielectric constant, $\varepsilon_r$, could be obtained from the ratio of the external field to the screened field inside the molecule, i.e.

$$\varepsilon_r = \frac{E_{\text{external}}}{E_{\text{screened}}} \qquad \text{(Eq 4.1)}$$

For reference, a 21-atomic-layer thick silicon slab was placed in a unit cell to benchmark this method and an $\varepsilon_r \approx 10$ was obtained. More detail will be presented in the supplemental section.

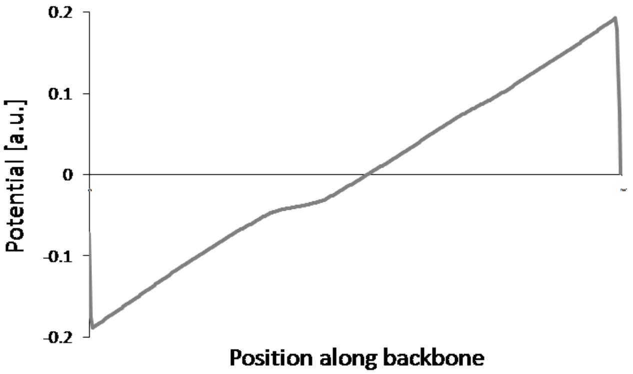

Figure 4.11, local potential as a function of the position along the backbone of the [2]rotaxane molecule.

Figure 4.11 shows a plot of local potential of a [2]rotaxane molecule placed inside a 20Å×20Å cell. In spite of the apparent smoothness of the curve, as shown in figure 4.12, the extracted $\varepsilon_r$ varied with position along the long axis of the [2]rotaxane molecule. The variations in $\varepsilon_r$ could be understood from the different species along the backbone reacting differently to the applied external electric field. Given this fact, the [2]rotaxane molecule could be viewed as many capacitors of different $\varepsilon_r$ connected in series. The equivalent capacitance is then given by the harmonic mean, or

$$C_{eq} = \left(\sum \frac{1}{C_i}\right)^{-1} \qquad \text{(Eq 4.2)}$$

which yields an effective dielectric constant, $\varepsilon_r^{\text{eff}}$,

$$\varepsilon_r^{\text{eff}} = \frac{T}{t_i}\left(\sum \frac{1}{\varepsilon_r}\right)^{-1} \qquad \text{(Eq 4.3)}$$

Where T was the total thickness of the dielectric, $t_i$ was thickness of each slice of the dielectric with a local dielectric constant of $\varepsilon_r$. Using the above equation, $\varepsilon_r^{\text{eff}}$ of the [2]rotaxane in its OFF- and ON-state were found to be 1.8 and 2.0, respectively.

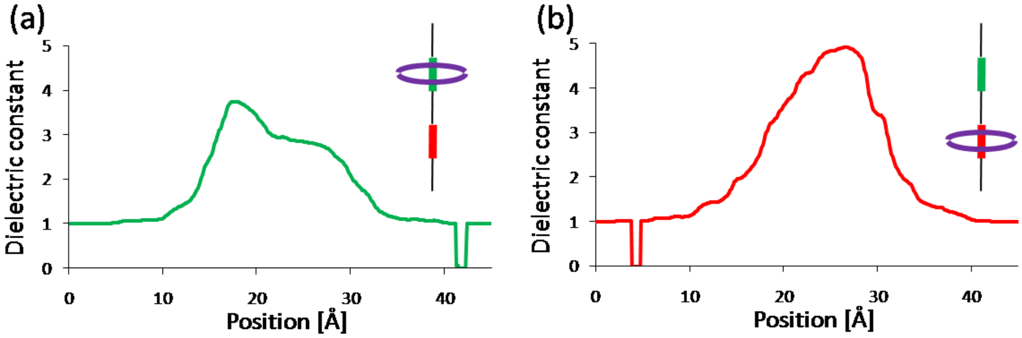

Figure 4.12, the extracted dielectric constant as a function of position along the backbone. The dielectric constant varies with position because of the different responses to external field from the different species along the backbone. The effective dielectric constant, $\varepsilon_r^{\text{eff}}$, for (a) the OFF-state is 1.8 while that of (b) the ON-state is 2.0. These results are obtained from the 20Å×20Å×45Å cells.

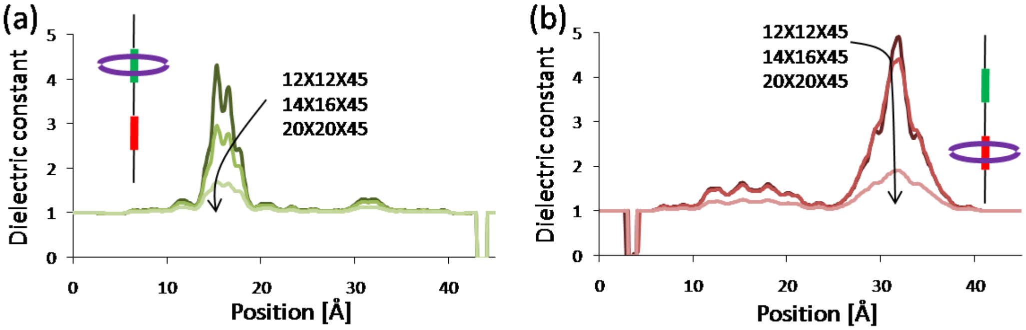

Figure 4.13, the extracted dielectric constant as a function of position along the backbone, for the system where the counter-ions are missing. The dielectric constant of the (a) OFF- and (b) ON-state are calculated with 3 different cell size, 12Å×14 Å×45Å, 14Å×16Å×45Å, and 20Å×20Å×45Å. As the cell size decreases, $\varepsilon_r^{eff}$ increases due to increased interaction between neighboring cells.

As previously mentioned, the experimentally reported surface density of the [2]rotaxane molecule was substantially smaller than 20Å×20Å = 400Å$^2$. However, shrinking the cell size while retaining the counter-ions in the system resulted in convergence problems, probably due to the increased interaction between the anions with its neighbors. An early study on the dielectric constant of the [2]rotaxane molecule without the counter-ions did converge for the smaller cell size and the findings are shown in figure 4.13. In addition to guaranteeing the proper functioning of the [2]rotaxane molecule, the counter-ions also substantially affected the dielectric constant. This was because the presence of these negatively charged ions altered the electrostatic interaction between the CBPQT-ring and the backbone. For both the OFF- and ON-state, the dielectric constant showed a strong dependence on the packing density. Figure 4.14 shows $\varepsilon_r^{eff}$ of the [2]rotaxane molecule without the counter-ions as a function of cell size. The calculated $\varepsilon_r^{eff}$ of the [2]rotaxane molecule with counter-ions was placed on the same figure. By following the same trend, a rough estimate on the $\varepsilon_r^{eff}$ was made for the latter cases and

$\varepsilon_r^{eff}$ = 1.8 for OFF-state, and

$\varepsilon_r^{eff}$ = 2.2 for ON-state

will be used in the following analysis.

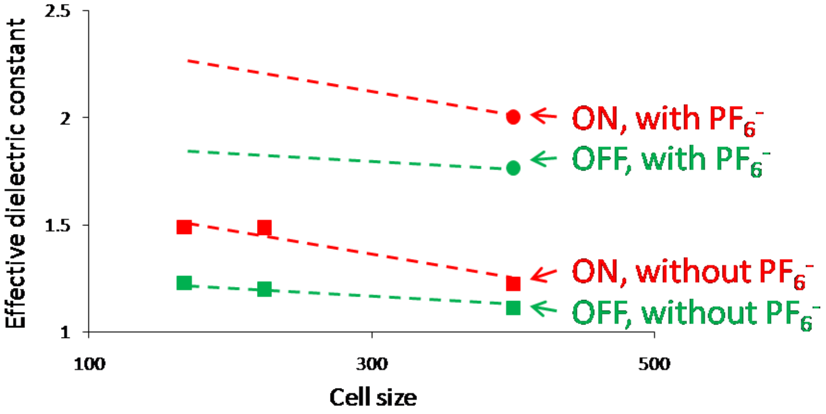

Figure 4.14, the dependence of the dielectric constant on cell size. The results from the calculations where the counter-ions are included are placed on the same plot. An estimation on the effective dielectric constants of the [2]rotaxane molecule with its four counter-ions in a closely packed monolayer are 1.8 and 2.2 for the OFF- and ON-states, respectively.

## 4.4 An alternative switching mechanism

The findings presented in the previous section raised questions regarding how the [2]rotaxane molecule switched. While it was proposed that [5]

$$\text{[2]rotaxane} \rightarrow \text{[2]rotaxane}^{1+} \xrightarrow{\text{repel}} \text{CBPQT-ring shuttles} \xrightarrow{\text{reduction}} \text{[2]rotaxane}$$

the result shown in figure 4.10 challenged its validity. Figure 4.10 shows the difference in charge density between a neutral and a 1+ charged [2]rotaxane molecule. It clearly illustrates that upon removing an electron from the system, the charge re-distributed throughout the entire molecule. As a result, the oxidation did not happen only at the TTF unit as suggested in reference [5]. Hence, the claim that the CBPQT-ring experienced an electrostatic repulsion from the charged TTF unit would not hold.

Furthermore, figure 4.15 shows the energy level diagram of the OFF-state of the [2]rotaxane molecule in contact with the top titanium electrode and the bottom n-type silicon electrode. It displays how the energy levels were positioned with respected to each other. For simplicity, the n-type silicon was assumed to be degenerately doped that the Fermi-level was at the conduction band minimum. Note that the broadening of the energy levels was not captured in this simple picture.

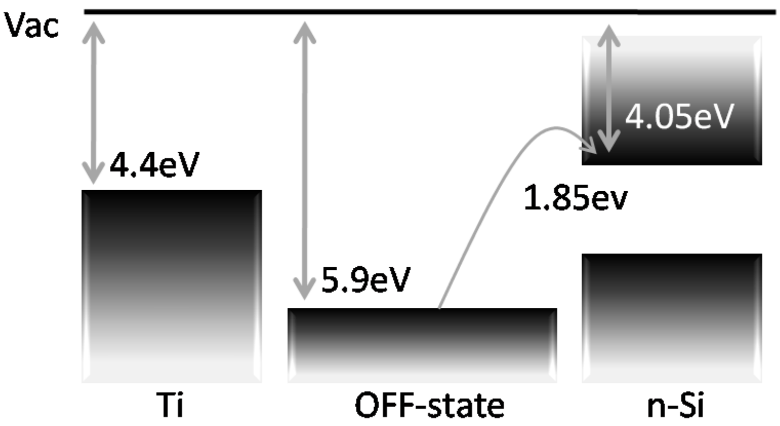

Figure 4.15, energy level diagram displaying how the energy levels of each component are positioned with respect to each other in the system where the OFF-state of [2]rotaxane molecule is sandwiched between the top titanium and bottom n-type silicon electrodes.

According to figure 4.15, at equilibrium, it would require about 1.5eV for the [2]rotaxane molecule to be charged to 1+, where 1.5eV was the difference between the work function of titanium and the first IP of the OFF-state of [2]rotaxane. It would cost even more energy, 1.85eV, to have the electron escape to the n-type silicon bottom electrode. Considering that the activation energy that separated the OFF- and ON-state was merely 600meV, removing an electron from the [2]rotaxane molecule required a much higher energy to take place. In light of these new evidences, an alternative switching mechanism was proposed as follow,

$$\text{[2]rotaxane} \xrightarrow{\text{supply energy to get over } E_\text{a}} \text{CBPQT-ring shuttles}$$

Even though the mechanism proposed in this thesis provided a more favorable pathway for the [2]rotaxane molecule, the above depiction could change when bias was applied. Figure 4.16 shows the energy level diagram with a +2V applied to the silicon electrode, as implemented in the reported experiments [1]. In this figure, the potential was assumed to have dropped evenly over the less conductive sacrificial layer and binding moieties at the two ends of the molecule. This pushed the molecule 1eV upwards with respect to the silicon electrode. However, to charge the [2]rotaxane molecule to 1+ state, another 0.85eV would be required. Hence, the previously proposed mechanism would not be able to appropriately describe the monolayer system being sandwiched between the electrodes in the crossbar memory experiment.

To test the validity of the newly proposed mechanism, i.e. the [2]rotaxane molecule switched from the OFF- to the ON-state simply because the applied bias supplied enough energy to get over the energy barrier, instead of looking at the energy level diagram, it would be more useful to investigate how the applied bias would affect the energy landscape. By assuming that the potential dropped uniformly across the entire molecule, to the first order, the energy landscape would have been tilted as shown in figure 4.17. This resulted in lowering the activation energy to only 400meV.

Comparing with the 600meV barrier height at equilibrium, the rate of the "shuttling" reaction was enhanced as expected. It would be illustrated in more detail later that in the $E_a$ = 600meV and $E_a$ = 400meV cases, the switching would happen in fractions of a second and microseconds, respectively.

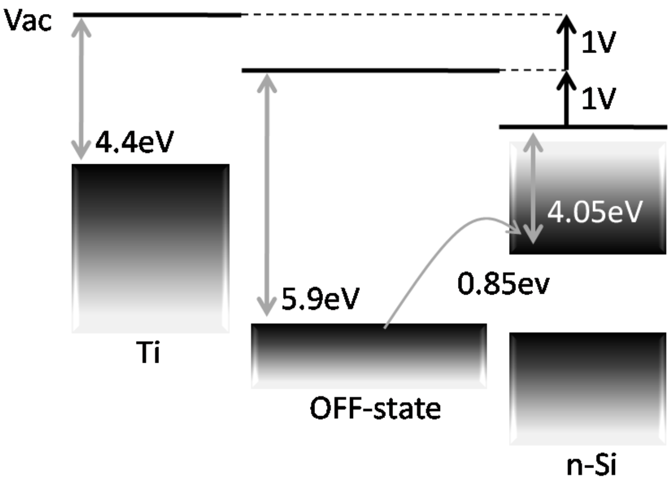

Figure 4.16, energy level diagram displaying how the energy levels of each component are positioned with respect to each other under a +2V bias applied on the silicon electrode. The potential is assumed to have evenly dropped over the sacrificial layer and the binding moiety at the two ends of the molecule.

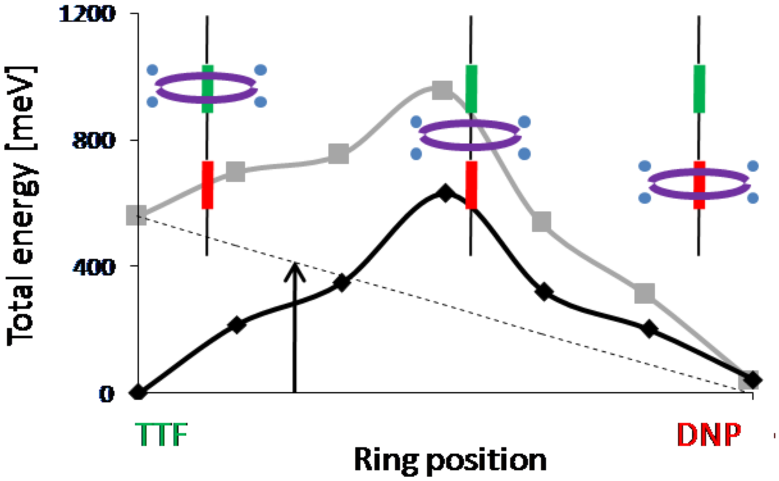

Figure 4.17, energy landscape of the "shuttling" reaction at equilibrium (black line) and under +2V bias, applied on the silicon electrode (grey line). The activation energy is reduced in the latter case.

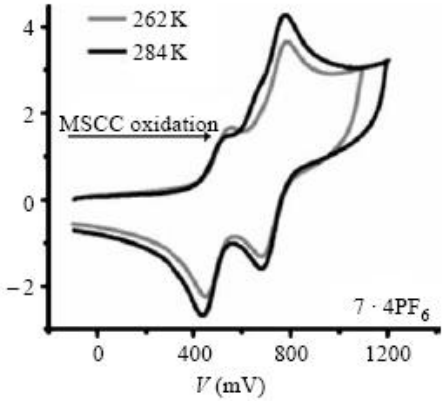

Figure 4.18, cyclic voltametry measurement of the [2]rotaxane on gold, after [12].

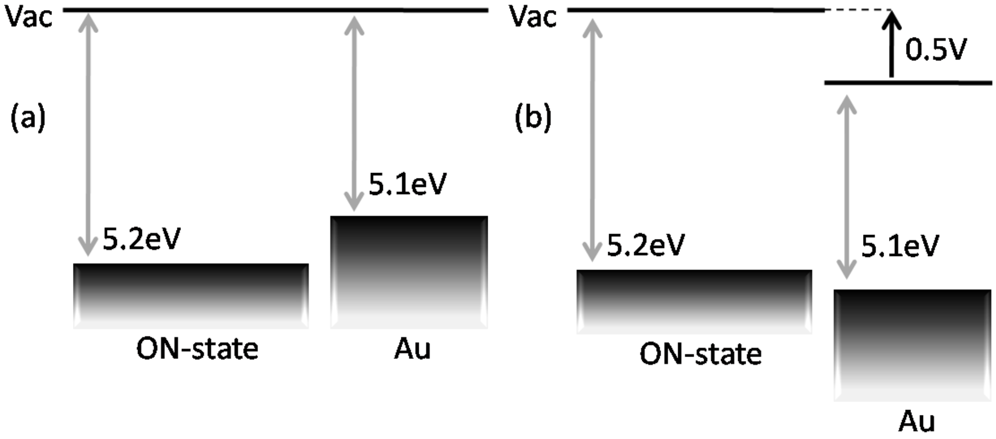

Figure 4.19, energy level diagrams that show that the mechanism proposed in this thesis explained the cyclic voltametry measurement shown in figure 4.16, (a) at equilibrium, and (b) when 0.5V was applied at the gold electrode.

Additionally, figure 4.18 shows one of the cyclic voltametry (CV) measurements reported in the review by Dichtel et al. [12]. In this case, a monolayer of the [2]rotaxane molecule was deposited on top of a gold substrate and was not sandwiched with another metal electrode on top. The energy level diagram of this scenario is shown in figure 4.19a. Figure 4.19b shows how the energy levels are positioned as a 0.5V bias is applied. The CV measurements were taken with a ramp rate of the applied voltage on the order 10mV/s to 100mV/s. The slow ramp rate ensured that the [2]rotaxane molecule would be switched to the ON-state upon applied bias. Therefore, figure 4.19 shows the IP of the ON-state of the [2]rotaxane molecule instead that of its OFF-state. This again suggested that the switching mechanism proposed in this work could also explain the CV measurements taken experimentally.

## 4.5 The switching performance

Table 4.1 summarizes the findings in the above studies on the [2]rotaxane molecule. The entitlement of the switching speed could then be estimated. The switching time, $t_{switch}$, was partitioned as the sum of two time factors:

1) $t_{shuttle}$: the time the CBPQT-ring takes to shuttle between the TTF and the DNP site, and
2) $t_{RC}$: the RC time constant associated with the circuit.

| | OFF-state | ON-state |
|---|---|---|
| IP | 5.9eV (first)<br>12.8eV (second) | 5.2eV (first)<br>10.8 (second) |
| $\varepsilon_r^{eff}$ | 1.2 (without $PF_6^-$)<br>1.8 (with $PF_6^-$) | 1.5 (without $PF_6^-$)<br>2.2 (with $PF_6^-$) |
| $E_a$ | 631meV (equilibrium)<br>400meV (2V bias) | |

Table 4.1, a summary of the physical properties calculated in section 4.2.

### 4.5.1 $t_{shuttle}$ – pre-factor and activation energy

As introduced above, the “shuttling” of the CBPQT-ring could be viewed as a “reaction,” and its dynamics could be captured by a rate constant, k, where

$$k = Ae^{-E_a/kT} \qquad \text{(Eq 4.4)}$$

The inverse of k would roughly equal $t_{shuttle}$. To estimate this figure, two parameters were needed. One was the activation energy, $E_a$, computed above, and the other was the pre-factor, A.

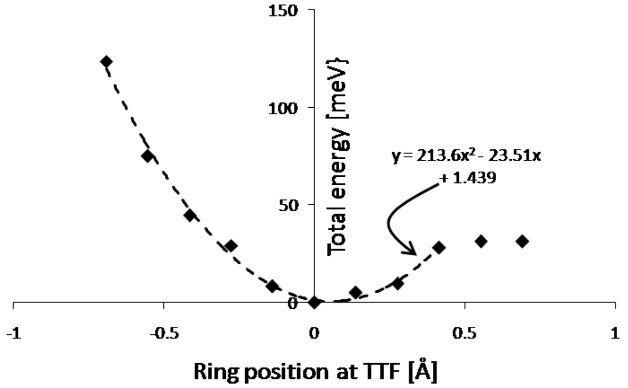

Figure 4.20, a finer mapping of the energy landscape about the OFF-state to obtain the curvature of this valley.

The pre-factor, or the attempt frequency, A, could be estimated from a simple transition state calculation. Reference [13] stated that this parameter was given by the product of all the n vibrational frequencies at the energy minimum divided by the (n-1) real vibrational frequencies at the saddle point. In the [2]rotaxane molecule system, the only relevant frequency to be determined was the frequency of the CBPQT-ring vibrating along the backbone at the OFF-state. A finer mapping of the energy landscape about the OFF-state is shown in figure 4.20. Fitting this portion of the energy landscape with

$$E = \frac{1}{2}kx^2 \qquad \text{(Eq 4.5)}$$

where k was the spring constant, the frequency, f, could be calculated from

$$f = \sqrt{\frac{k}{m}} \qquad \text{(Eq 4.6)}$$

where m was the mass of the CBPQT-ring and the four $PF_6^-$ counter-ions. This yielded an estimation of A to be $1.4\times10^{12}s^{-1}$.

Substituting these values into the Arrhenius equation, $t_{shuttle}$ was estimated to be 0.17s, at equilibrium, and $3.7\times10^{-6}$s, when a 2V bias is applied across the electrodes. While $t_{shuttle} = 3.7\times10^{-6}$s under 2V bias was not a spectacular switching speed already, the equilibrium switching time of 0.17s meant that the memory was somewhat volatile and thus this technology could only be used as a non-volatile memory, with a refreshing rate of about 10Hz.

### 4.5.2 $t_{RC}$ – resistance and dielectric constant

Since a crossbar memory network could be modeled as a transmission line, as shown in figure 4.21, the delay associated with the critical path was given by the Elmore delay model:

$$t_{RC} = C_1R_1 + C_2(R_1 + R_2) + \cdots + C_n(R_1 + R_2 + \cdots + R_n) \quad \text{(Eq 4.7)}$$

With the knowledge of the dielectric constant, the bulk resistivity of the electrodes, and the dimensions of the crossbar array specified in reference [14] (also listed in table 4.2), one could easily arrive at a RC delay of 7ns for the recently demonstrated 160k-bit [2]rotaxane crossbar memory arrays. This was about 3-order of magnitudes shorter than $t_{shuttle}$ and insignificantly added to the total switching time.

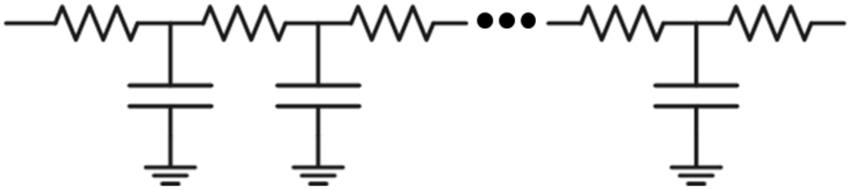

Figure 4.21, a transmission line model.

| | Top electrode (titanium) | Bottom electrode ($5\times10^{-19}$cm$^{-3}$ Phosphorus-doped silicon) |
|---|---|---|
| ρ [Ω-cm] | $40\times10^{-3}$ | $1.2\times10^{-3}$ |
| Thickness [nm] | 20 | 33 |
| Pitch [nm] | 33 | |
| Width [nm] | 16 | |

Table 4.2, specifications of the 160k-bit [2]rotaxane crossbar memory demonstrated in reference [14].

### 4.5.3 $t_{switch}$ – a circuit level study

While a 160k-bit crossbar memory array was demonstrated, the switching speed was still largely limited by the intrinsic switching time of the [2]rotaxane molecule itself. On the good side, this meant that a larger array could possibly be made without compromising the switching time. It would then be interesting to know what the maximum size of the array could be before the $t_{RC}$ started dominating the switching time. More importantly, at equilibrium, $t_{shuttle} = 0.17s$ posed an upper limit on how large an array could be. In addition, for researchers who did not have access to the special superlattice nanowire pattern transfer (SNAP) technique used in reference [14], knowing how $t_{switch}$ depended on the patterning technology would be useful. This section would address all these questions.

Figure 4.22 shows the switching time as a function of array size in a log-log plot. The red dot corresponds to the RC delay of the circuit in the 160k-bit memory demonstrated [14], which contributed insignificantly to the total switching time. It also shows that with the SNAP technique, an array as big as 16M-bit could still fully exploit the 3.7μs shuttling time intrinsic to the molecule. Furthermore, a 1T-bit array would not function properly anymore as any given bit could flip by itself randomly.

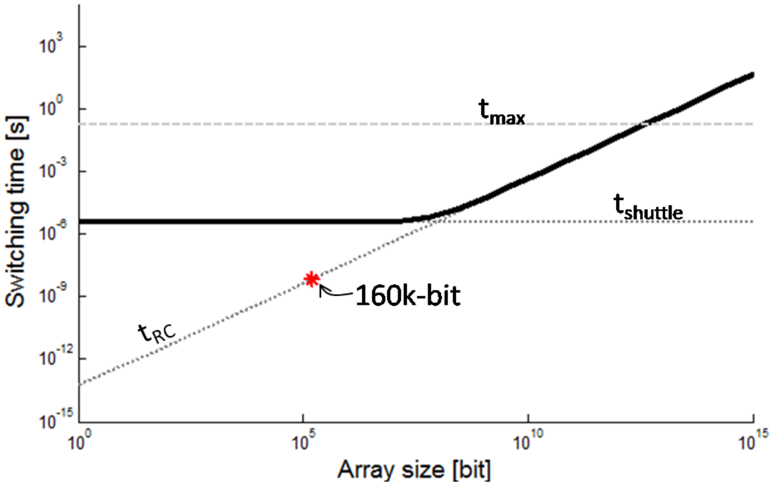

Figure 4.22, plot of switching time against array size, based on the specification listed in table 4.2. The red dot corresponds to the 160k-bit memory demonstrated in reference [14].

Figure 4.23 investigates how $t_{RC}$ varies as a function of the patterning technology in terms of pitch. Several common technologies (90nm, 0.25μm and 1μm) were chosen. As expected, the older the technology, i.e. larger pitch, the larger the RC time constant. As a result, the optimal array size shrank from 16M-bit, with SNAP, to 16k-bit in 1μm technology. Similarly, with the 1μm technology, the maximum size of a functioning array decreased to 1G-bit.

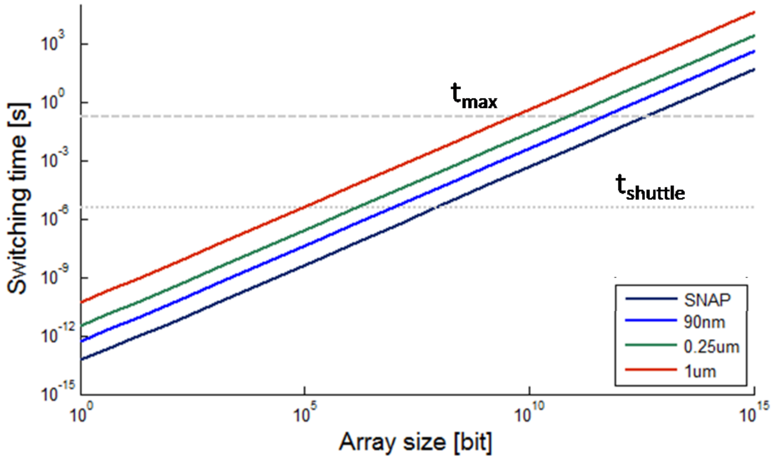

Figure 4.23, plot of switching time against array size for several different pitches to compare against the SNAP technique.

## 4.6 Summary

To conclude, the [2]rotaxane molecule had been thoroughly studied in this work through first principles calculations. The equilibrium energy landscape had been mapped out. An energy barrier of about 600meV separating the OFF- and ON-states was calculated. It was further shown that the counter-ions were essential to the proper functioning of the [2]rotaxane molecule. Additionally the ionization potentials of the [2]rotaxane molecule at the OFF- and ON-states were computed. They were 5.9eV and 5.2eV. Based on these new findings, an alternative switching mechanism that did not involve charging the molecule was proposed.

Moreover, the effective dielectric constants of the [2]rotaxane molecule at its OFF- and ON-states were computed. They were 1.8 and 2.0 when the cells were 20Å×20Å. After reviewing the trend of how the dielectric constant varies with cell sizes in the case where the counter-ions were absent, the effective dielectric constants were estimated to be 1.8 and 2.2 for the OFF- and ON-states respectively.

Additionally, by carefully mapping the energy landscape of the [2]rotaxane molecule at its OFF-state, the pre-factor in the Arrhenius equation was estimated to be $1.4\times10^{12}s^{-1}$, based on simple transition state calculations. Together with the calculated activation energy, $t_{shuttle}$ was estimated to be 0.17s at equilibrium and 3.7μs under 2V bias. Furthermore, using the computed dielectric constant, the bulk resistivity of the electrodes and the dimensions of the crossbar memory array reported [14], the $t_{RC}$ for the 160k-bit crossbar demonstrated was found to be 7ns, which did not significantly affect total switching time.

Lastly, using Elmore delay model, the optimal size of an array fabricated with the SNAP technique was found to be 16M-bit and any array larger than 1T-bit would not function properly due to the 0.17s shuttling time at equilibrium. The dependence on patterning technology of the switching time was also investigated.

# Supplemental information

The supplemental information provided in this section includes the benchmarking of the method of computing the ionization potential with benzene and dielectric constant with silicon slab, detail in calculation of the pre-factor, and a short derivation of the equation used to plot figure 4.22 and figure 4.23 from Elmore delay model. In addition, the atomic configuration of the [2]rotaxane molecule is briefly presented. A sample VASP input file is also attached.

## S4.1 Benchmarking with benzene

Due to the presence of a monopole, the total energy of a charged system in repeating unit cells was known to be a function of the volume of the cell [15], i.e.

$$E_{total} = A + \frac{B}{V} \qquad \text{(Eq 4.8)}$$

Figure 4.24 shows the calculated total energy of a 1+ charged benzene placed in a box with the dimensions of 10Å×10Å×z, where z = 10Å, 20Å, 30Å, 40Å, 50Å and 100Å. A straight line was fitted to these points, revealing that the total energy of an isolated benzene molecule charged to 1+ was -66.41eV. By definition, the ionization potential was the difference in the total energy between 1+ state and neutral state, which was found to be -76eV, independent of the size of the cell. This yields

$$IP_1(benzene) = (-66.41) - (-76) = 9.6eV$$

This reasonably agreed with the experimentally obtained ionization potential [11].

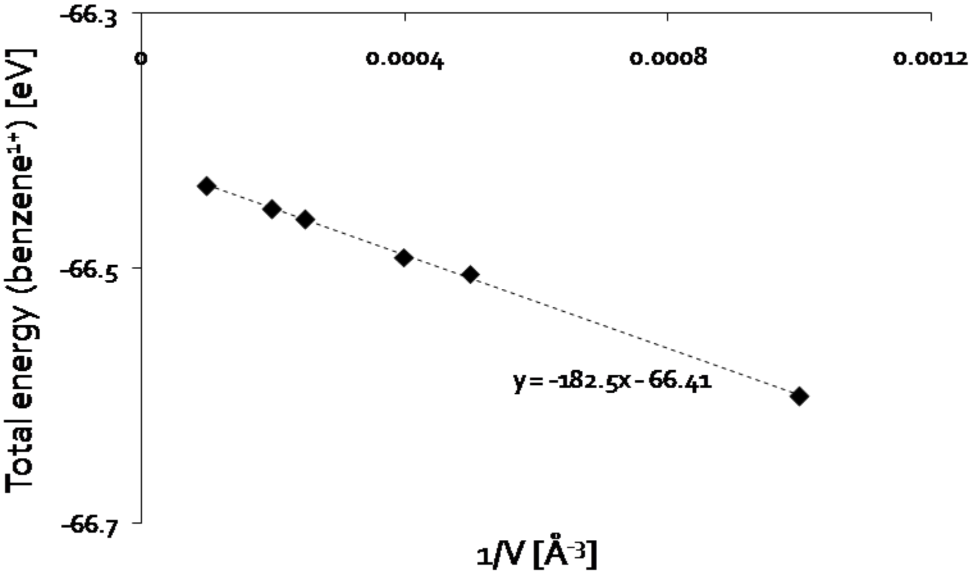

Figure 4.24, total energy of benzene$^{1+}$ versus the inverse of the volume of the cell. The total energy of an isolated benzene$^{1+}$ is determined to be -66.41eV.

## S4.2 Benchmarking with silicon slab

A 21-atomic-layer thick silicon slab was placed inside a unit cell. Sufficient empty space was given to separate the slabs due to periodic boundary condition. Potential profiles of the system with and without applied electric field were obtained. The difference between the two profiles was taken to eliminate the background potential due to the presence of the silicon ions. This resulted in figure 4.25. By definition, the dielectric constant was the ratio of the external field to the screened field inside the slab. This was found to be 10, and was agreed reasonably with the experimental value of 11.8.

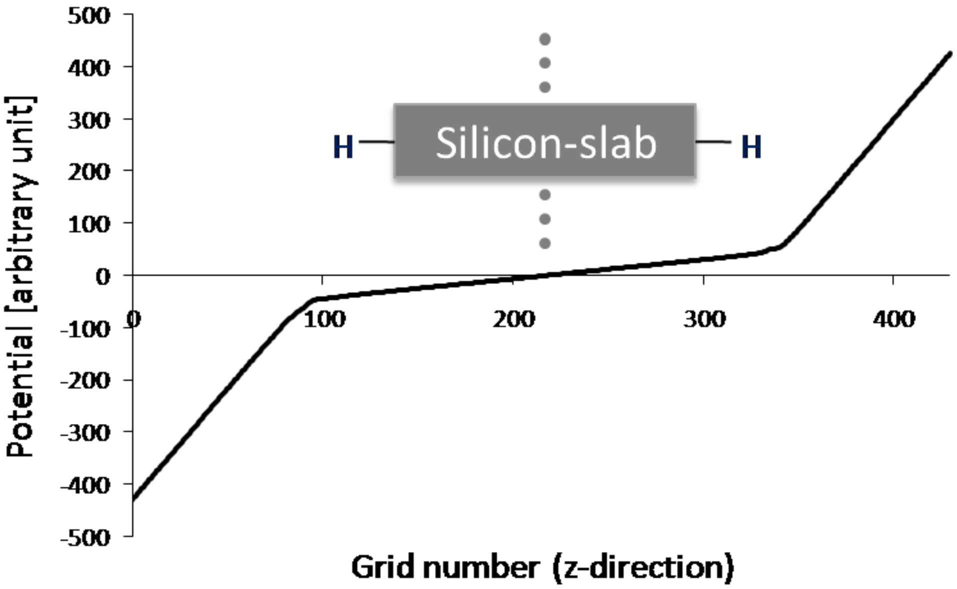

Figure 4.25, total potential versus position along the direction perpendicular to the surfaces of the silicon slab. The inset cartoon shows hydrogen terminated silicon-slab is repeating in the other two directions. A dielectric constant of 10 for silicon is obtained from this exercise.

## S4.3 Pre-factor calculation detail

By fitting the valley of the OFF-state minimum with a quadratic polynomial, a spring constant could be obtained. This allowed a first-order estimation of the pre-factor by the simple relation

$$A = \sqrt{\frac{k}{m}} \qquad \text{(Eq 4.9)}$$

with m being the mass of movable part, including the CBPQT-ring and the counter-ions, thus

$$m = 32H + 36C + 4N + 24F + 4P = 1100.5 \text{ atomic mass unit}$$

Putting in k = 213.6meV/Å$^2$, A = 1.36×10$^{12}$s$^{-1}$.

## S4.4 Derivation from Elmore delay model

Assuming the dimensions to be n×n, the square crossbar array has n top electrodes (bit lines) and n bottom electrodes (word lines). Thus, along the critical path, the signal will see 2n cells. The delay time is then

$$t_{delay} = R_{bot}C + 2R_{bot}C + \cdots + nR_{bot}C + \\ (nR_{bot} + R_{top})C + (nR_{bot} + 2R_{top})C + \cdots (nR_{bot} + nR_{top})C \qquad \text{(Eq 4.10)}$$

As $\sum_{i=1}^{n} i = \frac{n(n+1)}{2}$,

$$t_{delay} = \frac{3n^2+n}{2}R_{bot}C + \frac{n(n+1)}{2}R_{top}C \qquad \text{(Eq 4.11)}$$

## S4.5 Atomic configuration of the [2]rotaxane molecule

Figure 4.26 shows the [2]rotaxane molecule from different viewing angles. The bond lengths and some specific angles extracted from this model are presented in table 4.3 and 4.4. Well-established bond lengths from literature are also displayed for comparison.

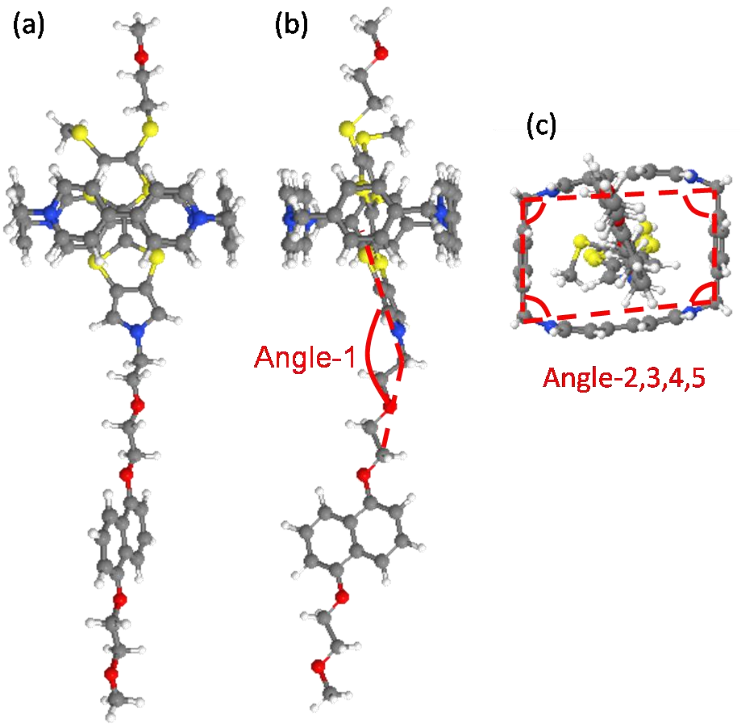

Figure 4.26, atomic model of the [2]rotaxane molecule, without the PF6- counter-ions. (a) Front view, (b) side view and (c) looking from the bottom.

| | Literature [pm] | This work [pm] |
|---|---|---|
| C-C | 154 | 152 |
| C=C | 134 | 136 |
| C=C (benzene) | 140 | 141 |
| C-O | 143 | 142 |
| C-H | 109 | 111 |

Table 4.3, comparisons between the common bond length found in the [2]rotaxane molecule in this work and the literature.

| | |
|---|---|
| Angle-1 | 152.2° |
| Angle-2 | 85.2° |
| Angle-3 | 94.6° |
| Angle-4 | 85.4° |
| Angle-5 | 94.5° |

Table 4.4, measurements of angles specified in figure 4.26

## S4.6 Sample VASP input file (INCAR)

This sample input file is slightly modified from an INCAR file. The job was to calculate the ionization potential of the [2]rotaxane molecule, carried out on February 6, 2008, for a 20Å×20Å×50Å cell. The atomic coordinates and the dimensions of the cell were specified in POSCAR placed in the same folder. Additionally, a POTCAR file tabulated the pseudopotentials and a KPOINTS file listed the k-point grid, which in this case was simply the $\Gamma$ point.

```
SYSTEM=R
PREC=Medium
ISMEAR=0
SIGMA=0.05
GGA=PE
LWAVE=.FALSE.
LVTOT=.FALSE.
LCHARG=.FALSE.

######
#Enable this block for computing the IP
######
#NELECT=603                           #number of electrons
#IDIPOL=4                             #4 for isolated molecule
#LDIPOL=.TRUE.                        #dipole/monopole correction
#DIPOL= 0.0270 0.9993 0.4538          #center of charge

######
#Enable this block to apply electric field
######
#EFIELD=-0.01                         #magnitude of E-field
#IDIPOL=3                             #along the 3RD axis

######
#This block is for projected density of state (PDOS)
######
#RWIGS = 0.7642 1.0426 1.0055 1.0314 1.1120 1.3159 1.4808
#NPAR = 1

ISIF=2                                #ion relaxation in fix cell
IBRION=2                              #conjugate gradient
NELM=200                              #200 step max for SCF
NSW=100                               #100 ion relaxation step
EDIFFG=-1e-4                          #stop condition (force)
```

Note: the comments on the right hand side were added to the original input file for clarification purpose. One may also need to delete the “tab” characters for VASP to run properly in UNIX environment. More detail can be found at the VASP official website:

http://cms.mpi.univie.ac.at/vasp/vasp/vasp.htm

# References

[1] Luo, Y.; Collier, C. P.; Jeppesen, J. O.; Nielsen, K. A.; DeIonno, E.; Ho, G.; Perkins, J.; Tseng, H. R.; Yamamoto, T.; Stoddart, J. F.; Heath, J. R., "Two-dimensional molecular electronics circuits," *ChemPhysChem*, *3*, **2002**, 519-525

[2] Deng, W. Q.; Muller, R. P.; Goddard, W. A., "Mechanism of the Stoddart-Heath bistable rotaxane molecular switch," *J. Am. Chem. Soc.*, *126*, **2004**, 13562-13563

[3] Jang, S. S.; Jang, Y. H.; Kim, Y. H.; Goddard, W. A.; Choi, J. W.; Heath, J. R.; Laursen, B. W.; Flood, A. H.; Stoddart, J. F.; Norgaard, K.; Bjornholm, T., "Molecular dynamics simulation of amphiphilic bistable [2]rotaxane Langmuir monolayers at the air/water interface," *J. Am. Chem. Soc.*, *127*, **2005**, 14804-14816

[4] Jang, S. S.; Jang, Y. H.; Kim, Y. H.; Goddard, W. A.; Flood, A. H.; Laursen, B. W.; Tseng, H. R.; Stoddart, J. F.; Jeppesen, J. O.; Choi, J. W.; Steueman, D. W.; DeIonno, E.; Heath, J. R., "Structures and properties of self-assembled monolayers of bistable [2]rotaxanes on Au (111) surfaces from molecular dynamics simulations validated with experiment," *J. Am. Chem. Soc.*, *127*, **2005**, 1563-1575

[5] Jang, Y. H.; Goddard, W. A., "Mechanism of oxidative shuttling for [2]rotaxane in a Stoddart-Heath molecular switch: Density functional theory study with continuum-solvation model," *J. Phys. Chem. B*, *110*, **2006**, 7660-7665

[6] Kresse, G.; Furthmuller, J., "Efficiency of ab-initio total energy calculations for metals and semiconductors using a plane-wave basis set," *Comput. Mater. Sci., 6*, **1996**, 15

[7] Kresse, G.; Furthmuller, J., "Efficient iterative schemes for ab initio total-energy calculations using a plane-wave basis set," *Phys. Rev. B*, *54*, **1996**, 11169

[8] Perdew, J. P.; Burke, K.; Wang, Y., "Generalized gradient approximation for the exchange-correlation hole of a many-electron system," *Phys. Rev. B*, *54*, **1996**, 16533-16539

[9] DeIonno, E.; Tseng, H. R.; Harvey, D. D.; Stoddart, J. F.; Heath, J. R., "Infrared spectroscopic characterization of [2]rotaxane molecular switch tunnel junction devices," *J. Phys. Chem. B.*, *110*, **2006**, 7609-7612

[10] Martin, R. M., Electronic structure: basic theory and practical methods, Cambridge University Press, **2004**

[11] Grubb, S. G.; Whetten, R. L.; Albrecht, A. C.; Grant, E. R., "A precise determination of the 1st ionization-potential of benzene," *Chem. Phys. Lett.*, *108*, **1984**, 420-424

[12] Dichtel, W. R.; Heath, J. R.; Stoddart, J. F.; "Designing bistable [2]rotaxanes for molecular electronic devices," *Philos. T. R. Soc. A*, *365*, **2007**, 1607-1625

[12] Vineyard, G. H., "Frequency factors and isotope effects in solid state rate processes," *J. Phys. Chem. Solids*, *3*, **1957**, 121

[13] Green, J. E.; Choi, J. W.; Boukai, A.; Bunimovich, Y.; Johnston-Halperin, E.; DeIonno, E.; Luo, Y.; Sheriff, B. A.; Xu, K.; Shin, Y. S.; Tseng, H. R.; Stoddart, J. F.;

Heath, J. R., “A 160-kilobit molecular electronic memory patterned at $10^{11}$ bits per square centimetre,” *Nature*, *445*, **2007**, 414-417

[14] Makov, G.; Payne, M. C., “Periodic boundary conditions in ab initio calculations,” *Phys. Rev. B*, *51*, **1995**, 4014-4022

# Chapter 5

# Molecular engineering

Physicists have been predicting natural phenomenon with theories for centuries. The development of quantum mechanics in the early 20th century opened up new frontiers for exploration, and the efforts by Hartree and Fock, and Hohenberg, Kohn and Sham to solve the Schrodinger equation for large systems allowed some of the most accurate predictions and verifications. In this chapter, total energy calculations based on density functional theory (DFT) are performed to scrutinize various molecules and to search for the most suitable ones for future experimental studies.

## 5.1 Motivations

In spite of the exhilarating demonstration of the dielectric integrated monolayer field effect transistor (DI-mFET) in chapter 2, it has been an expensive and arduous experience. After the concept was conceived, it took months for the first batch of devices to be fabricated and debugged. A year flew by as the longer molecules were synthesized and additional months were consumed for the availability of e-beam writer.

The fact that experiments are expensive to run is well-known. Computer aided design (CAD) tools are developed to assist engineers in exploring new concepts in almost every single field of engineering. This drastically reduces the cost of product development and the lead-time. Similarly, in scientific research, such practices should also lead to more efficient investigations. Taking the work in chapter 2 as an example, a simulation of the leakage current through $T_4C_{11}$ would have pointed to the use of the longer $T_4C_{18}$ molecules in the first pass, saving possibly a year of research effort.

Furthermore, inspired by the successful modeling work in chapter 3 and theoretical study in chapter 4, the vision of computer-aided molecular engineering may not be intangible. Therefore, in this chapter, as science and engineering come together in the construction of better molecules, a protocol based on first principles calculations is developed to search for the next generation organic semiconductors possessing higher mobilities. This is done through the investigation of the packing structure. Experimental results of several known molecules are first benchmarked with the protocol, which is then used to extensively search among the many molecules for appropriate candidates. Preliminary results are presented and recommendations on future direction are made.

## 5.2 Methodology

The following first principles calculations were performed with Vienna Ab-initio Software Package (VASP) [1, 2]. The generalized gradient approximation (GGA) was used to better model the physics of molecular structure with the Perdew-Burke-Enzerhof (PBE) parameterization [3]. In VASP, wavefunctions were expanded in plane-wave basis setsplane-wave basis sets and projector augmented wave (PAW) pseudopotentials replaced the core electrons. As the interest in this chapter was not to accurately predict the physical properties, but rather to focus on the general trends, $\Gamma$-point sampling should be sufficient.

As the scope of this work was only to predict the packing structure, only ion relaxations were performed. Candidate molecules were first drawn in SPARTAN, available from the Molecular Graphics and Computation Facility, College of Chemistry, University of California, Berkeley, and relaxed in 20Å×20Å×20Å boxes. To construct the starting configuration, the molecules were oriented within the unit cells as specified in reference [4, 5]. Four molecules were included in a super-cell instead of two, so that the results between the edge-to-face (e2f) and the face-to-face (f2f) cases were comparable. In addition to relaxing the atomic coordinates, the dimensions of the super-cell were allowed to change at the same time. As a result, instead of running 100 ion relaxation steps continuously, the entire process was broken down into 10 consecutive sub-processes, in each of which 10 steps were run. This prevented the energy cut-off from going out of bound.

## 5.3 Engineering the molecules

Throughout the last several chapters, different classes of molecules were clearly demonstrated as probable workhorse for different purposes. There are the acenes and the thiophenes as semiconductors, the alkanes as dielectrics, and the [2]rotaxane as molecular machines for memories. It is obvious that the imaginations of the scientists and engineers were the limits on the functions of the molecules, at least within the simulations. Covering the engineering of all these aspects is beyond the scope of this work.

Therefore, among the three classes of molecules described, this thesis chooses only to tailor molecules for better semiconductors. One of the most important reasons is that the development of a successful protocol for determining the desirable face-to-face (f2f) packing structure will bring forth immediate breakthrough to the currently stagnant advancement in organic semiconductors. While carrier mobility on the order of 1cm$^2$/Vs is frequently attainable at present, there is still a considerable gap to bridge between what organic and inorganic semiconductors can achieve. Although a mobility as high as 10cm$^2$/Vs was reported for rubrene, it was not soluble in most solvents. To further organic thin film transistors, a high mobility and soluble material would be desirable.

On the other hand, while dielectrics are important, the commonly used materials nowadays are still mainly thin films of polymers, if not silicon dioxide. The properties of these gigantic structures may not be easily captured within the framework of DFT and the techniques employed in the previous chapters. Furthermore, monolayer dielectrics, though interesting, are plagued by multiple problems discussed before. Also, to study the properties of dielectrics, for example, the dielectric constant and the leakage current, one can simply follow the techniques outlined in the last chapters. Hence, such redundant and less fruitful work is avoided.

Although the class of molecular machines is a very interesting to study, the simulation of these large molecules thwarts a careful search for attractive subjects from a large pool of candidates. Similarly, the assorted species within these large molecules complicated the systematic tuning for this basic trend study. The engineering of this class of molecules is thus put off for future, more in-depth study.

### 5.3.1 Goal and scope

The goal of this work was to engineer semiconducting organic molecules to exhibit enhanced properties, mainly focusing on the carrier mobility, as mentioned. Figure 1.6 is shown again in figure 5.1. Schematically, it was clear that the interaction between neighboring π-orbitals in the f2f structure was stronger than that in the e2f structure. From this simple argument, f2f structure could theoretically enjoy higher carrier mobility than its e2f counterpart. Thus, to achieve the goal of boosting the carrier mobility, molecules that would naturally pack in f2f were sought.

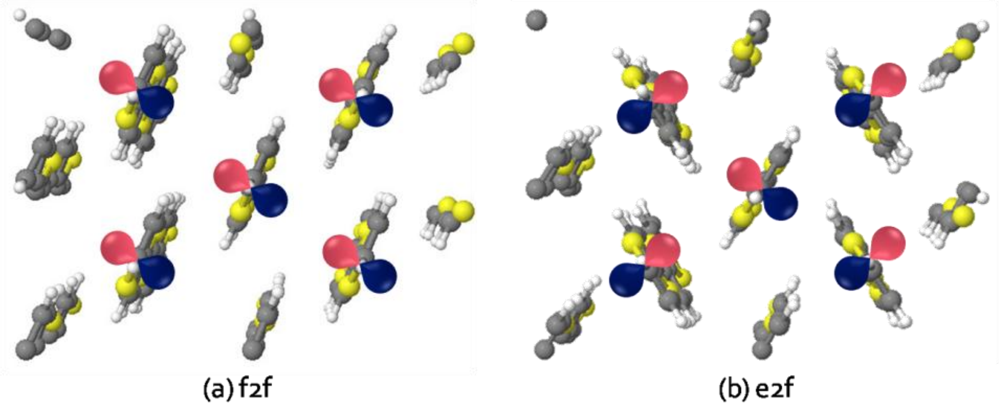
(a) f2f (b) e2f

Figure 5.1, top views of (a) f2f and (b) e2f packing schemes. Arbitrary π-orbitals are added to illustrate the enhanced interactions between neighboring molecules in the f2f scheme.

Instead of the thiophene family covered in chapter 3, the acene family had been chosen as the subject of investigation in this work for three major reasons:

1) while acenes are found to be e2f, there has been report evidencing that 5,11-dichlorotetracene (a4-5,11-cl) is f2f.
2) acenes are technologically important, since pentacene has been reported and demonstrated repeatedly to have one of the highest carrier mobility and mobility on the order of 0.1 – 1cm$^2$/Vs.
3) after synthesizing the appropriately functionalized pentacene, comparisons can be readily made as pentacene is commercially available.

In addition, it is known that graphene is f2f. Studying the acene family by expanding the molecules as shown in figure 5.2 may yield a tipping point from packing as e2f to f2f. The knowledge gained from this exercise can potentially help understanding the reason why many organic crystals are found packed as e2f. However, this investigation is deferred until the protocol developed in this work becomes well-defined.

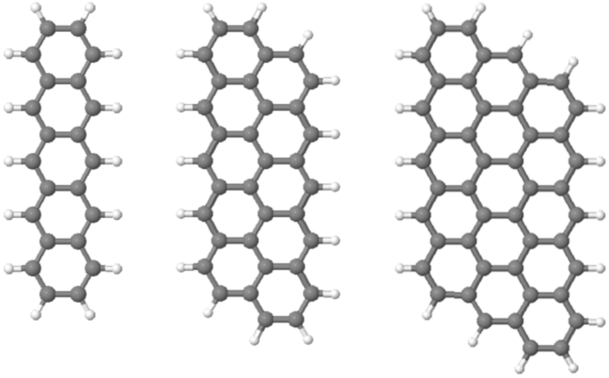

Figure 5.2, pentacene and graphene-like molecules expanded from pentacene.

The candidate molecules are shown in figure 5.3. They included anthracene (a3), tetracene (a4), pentacene (a5) and a number of halogenated derivatives of them.

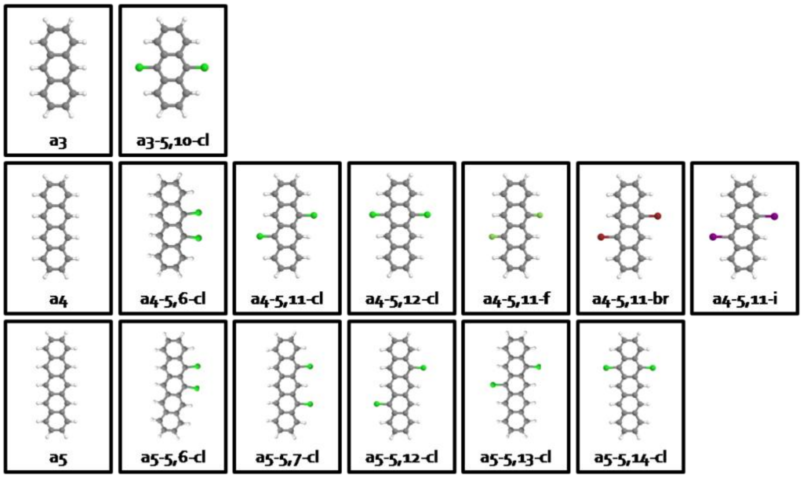

Figure 5.3, the list of candidate molecules being studied in this work. In each family, two of the hydrogen atoms are substituted by chlorine atoms and the positions of the substitution are varied systematically. For a4-5,11 structures, other halogens (F, Br, and I) are also tried to test for a trend down Group VII.

## 5.3.2 Results

Figure 5.4 summarizes the overall findings of this work. For each candidate molecule, it plots the difference in total energy between the e2f and the f2f configurations. A positive difference meant that the molecule was predicted to pack as e2f and a negative difference as f2f. Among the molecules put under test, the packing structure of a3, a4, a5, a4-5,11-cl and perfluoro-pentacene (a5-allF) were documented [4, 5, 6]. While it was encouraging that figure 5.4 shows agreement with literature for a4, a5 and a4-5,11-cl, the discrepancy in the case of a3 and a5-allF was troubling. However, the large negative difference of several tens of eV for a3 and a5-allF were alarmingly, hinting that the outcome of this protocol for these cases should be interpreted cautiously. It will be argued below that this work is on the right track and potential solutions to reconcile the disagreement are suggested.

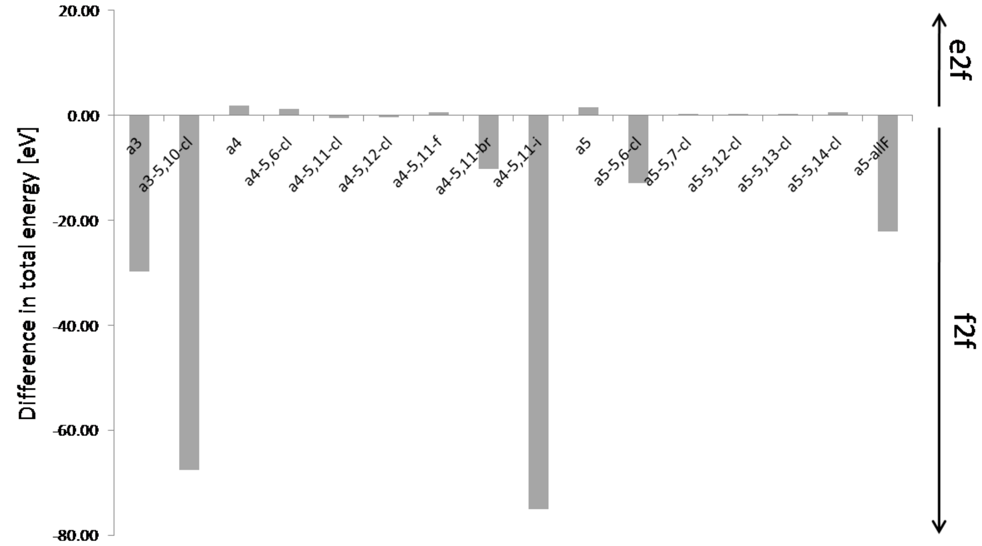

Figure 5.4, summary of the ion relaxation results of all the candidate molecules, plotting the difference between the total energies of the e2f and f2f configurations. Positive difference means that the calculation predicted an e2f packing is more energetically favorable and a negative difference means the opposite.

## 5.3.3 Discussions

One of the major concerns about predicting physical properties of organic crystals with DFT was the lack of Van der Waal's (VdW) force in the formalism [7]. Schroder et al. were developing Van der Waals density functional to overcome this deficiency [8]. However, such frontier work was not employed in this thesis, where the goal was to investigate if DFT alone was adequate for this prediction. It still seemed promising because simply from geometry, one would expect a larger VdW force holding the molecules together in the f2f case than in the e2f case. As a result, if DFT alone would already predict that f2f was a more energetically favorable structure, including VdW interactions would inevitably lead to an even more favorable condition for f2f.

While DFT was used in both the previous and this chapter, the successful modeling of the $T_4C_{11}SH$ monolayer accomplished strongly contrasted the ambiguous results presented in this section. A major difference in these two works was that the lattice parameters were constrained during the ion relaxation in previous chapter, while they were allowed to vary here. Unlike the $T_4C_{11}SH$ monolayer, the information on the lattice parameters was unavailable for most of the candidate molecules. Simply forcing all the candidate molecules into the fixed unit cells would lead to an unfair comparison due to the different side groups and shapes. Therefore, the lattice parameters provided in reference [4, 5] were only taken as references to construct the starting configuration. Despite, it was believed the adopted methodology could not have resulted in the observed discrepancies for a3 and a5-allF with such a large difference.

The construction of the starting configuration deserves further elaboration. Figure 5.5 shows the initial unit cells setup for the tetracene in the e2f and f2f packing motif in (a) and (b) respectively. There were four molecules in the unit cells, instead of two. The inclusion of the additional two molecules resulted from how reference [4, 5] specified their unit cells, as shown by the shaded region in figure 5.5. It was obvious that the tetracene at the top right in figure 5.5a did not correspond to the one at the bottom left in figure 5.5b. Therefore four-molecule unit cells were used to allow fair comparison between the total energies of two structures being investigated. And because there were quite a large number of atoms (96, 120 and 144 atoms for a3, a4 and a5 families, respectively) inside a reasonably large cell, $\Gamma$-point sampling was believed to be sufficient.

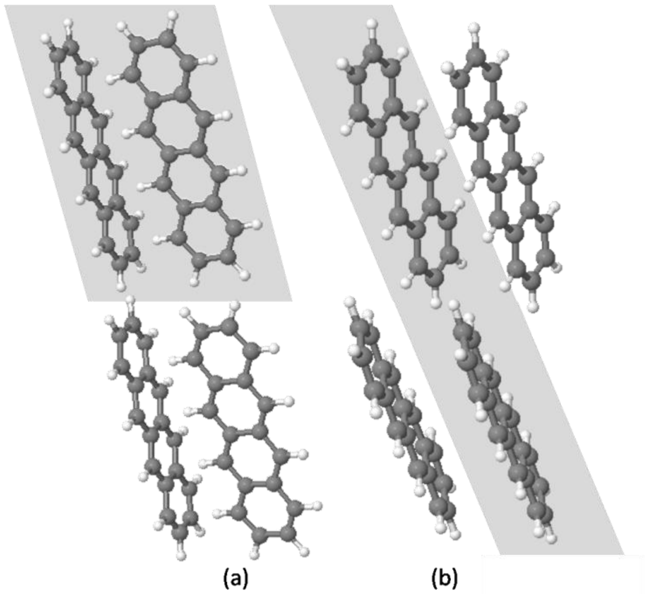

Figure 5.5, unit cells of tetracene setup as (a) e2f and (b) f2f for the calculations performed. The two molecules shaded in each case comprise the primitive unit cell specified in reference [4, 5]. The total energies calculated from these primitive unit cells cannot be compared directly because the second molecules in one structure are not an equivalent counterpart to the other. Therefore, these four-molecule super cells are constructed, but this leads to increased complexity.

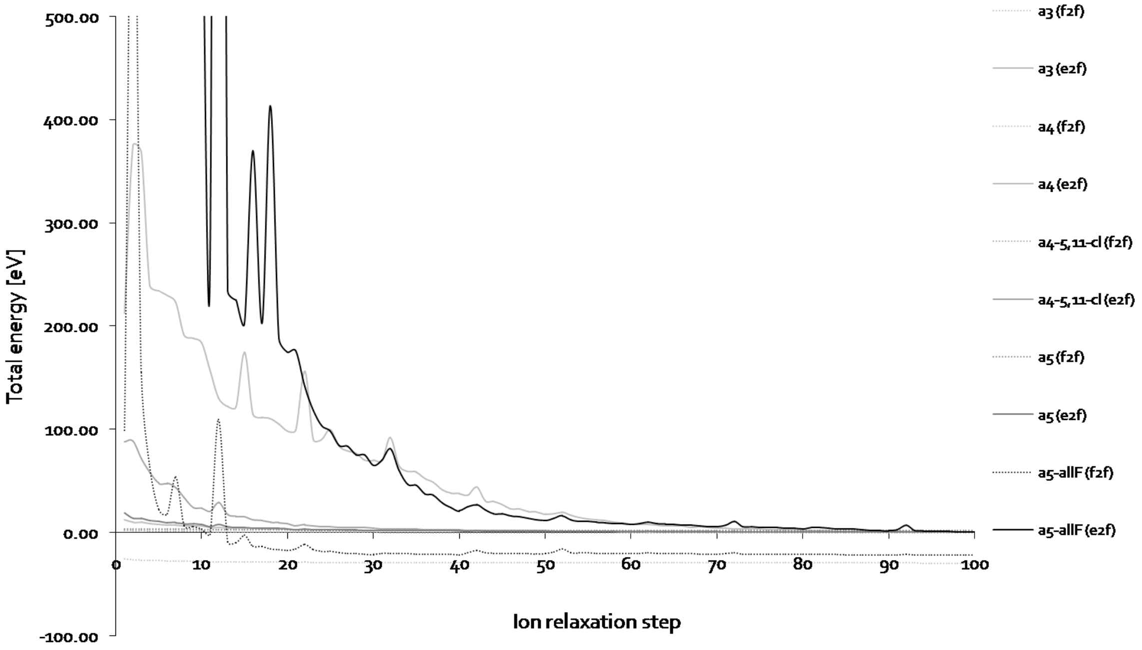

Figure 5.6, the evolution of the total energy of the benchmark molecules in the ion relaxation process. Extremely large positive energy are observed at the beginning of the process for a3 (e2f) and a5-allF (e2f).

As mentioned above, the negative difference in total energies for the a3 and a5-allF cases were alarmingly large, reaching 30eV and 20eV, respectively. This prompted a closer examination on the origin of these large differences. Figure 5.6 shows how the total energies of the benchmarks (a3, a4, a4-5,11-cl, a5 and a5-allF) evolve in the ion relaxation process. The total energies have been normalized to the final e2f total energies in the respective cases. It could be readily seen that the initial total energies of the a3 and a5-allF as e2f were significantly larger than the rest. This was probably due to an inappropriate setup of the starting configurations. This is believed to be the source of the large negative difference observed in figure 5.6. Another point worth mentioning is that the changes in total energy for the f2f cases were significantly smaller than those of the e2f cases. This probably suggests that the information adopted from reference [4] was not very suitable.

To correct the observed discrepancies in figure 5.4, the large positive energies associated with the starting configurations for the e2f cases must be minimized. One obvious solution would be to setup the starting configurations with another set of lattice parameters and internal orientations. However, the predictions would then be less convincing as they would depend on the initial structure!

Other possible ways to ameliorate this protocol for determining the packing structure are under investigation. These included increasing the number of k-points sampled, the use of local density approximation (LDA) pseudopotentials, relaxing the ions and the shape of the cell within a fixed volume, and constricting the tolerance level for the self-consistent field calculations.

## 5.4 Summary

Despite the ambiguous preliminary results presented, arguments were made to justify the rationale behind molecular engineering with DFT. Also, possible sources of error causing the ambiguity were identified.

In addition to the theoretical study, experimental verifications of the findings from this chapter must be pursued to complete this work. This includes the synthesis of the candidate molecules and characterization of the monolayer deposited. Interested readers can follow the work presented in chapter 3 to accomplish the latter, but as chemical synthesis was outside the area of expertise of the author, interested readers are referred to [9].

# References

[1] Kresse, G.; Furthmuller, J., “Efficiency of ab-initio total energy calculations for metals and semiconductors using a plane-wave basis set,” *Comput. Mater. Sci., 6*, **1996**, 15

[2] Kresse, G.; Furthmuller, J., “Efficient iterative schemes for ab initio total-energy calculations using a plane-wave basis set,” *Phys. Rev. B*, *54*, **1996**, 11169

[3] Perdew, J. P.; Burke, K.; Wang, Y., “Generalized gradient approximation for the exchange-correlation hole of a many-electron system,” *Phys. Rev. B*, *54*, **1996**, 16533-16539

[4] Campbell, R. B.; Trotter, J.; Monteath, J., “Crystal structure of hexacene, and a revision of crystallographic data for tetracene and pentacene,” *Acta. Cryst.*, *15*, **1962**, 289-290

[5] Moon, H.; Zeis, R.; Borkent, E. J.; Besnard, C.; Lovinger, A. J.; Siegrist, T.; Kloc, C.; Bao, Z. N., “Synthesis, crystal structure, and transistor performance of tetracene derivatives,” *J. Am. Chem. Soc.*, *126*, **2004**, 15322-15323

[6] Sakamoto, Y.; Suzuki, T.; Kobayashi, M.; Gao, Y.; Inoue, Y.; Tokito, S., “Perfluoropentacene and perfluorotetracene: synthesis, crystal structures and FET characteristics,” *Mol. Cryst. Liq. Cryst.*, *444*, **2006**, 225-232

[7] Dion, M.; Rydberg, H.; Schroder, E.; Langreth, D. C.; Lundqvist, B. I., “Van der Waals density functional for general geometries,” *Phys. Rev. Lett.*, *92*, **2004**, 246401

[8] Kleis, J.; Lundqvist, B. I.; Langreth, D. C.; Schroder, E., "Towards a working density-functional theory for polymers: first-principles determination of the polyethylene crystal structure," *Phys. Rev. B*, *76*, **2007**, 100201R

[9] Loudon, G. M., Organic chemistry 4th edition, Oxford University Press, **2001**

# Chapter 6

# Recommended future work and conclusions

Following previous work by Chang et al., this work continued research towards the ultimate goal of a single molecule transistor for the post-CMOS era. This chapter reviews the accomplishments made in this thesis and recommends promising future directions.

## 6.1 Recommended future work

As this thesis covered a broad amount of both experimental and theoretical work, this section is broken down into two parts, the experimental work and the theoretical work. Recommendations are made mainly focusing on near-term projects.

### 6.1.1 Experimental work

The first recommended future work is the demonstration of a more robust dielectric integrated monolayer field effect transistor (DI-mFET) that has a higher yield. Possible improvements upon the current fabrication process were mentioned in chapter 2. They include two-layer metal evaporation technique, the use of longer alkyl dielectric and a new device structure that resembles the conventional organic thin film transistor (OTFT).

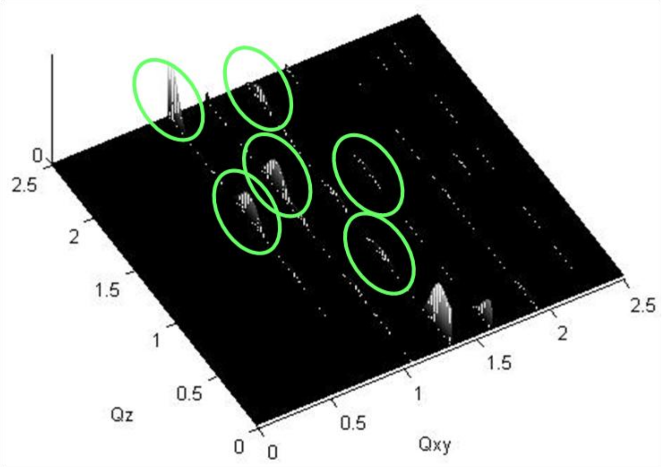

Figure 6.1, calculated XRD pattern predicting additional peaks not observed in the GIXD data experimentally obtained. The peaks encircled need further experimental measurement.

As a large portion of this thesis focused on theoretical predictions, experimental verifications of their claims will be essential. At the end of chapter 3, additional peaks were predicted in the calculated X-ray diffraction (XRD) pattern, as shown again in figure 6.1. If they are to be experimentally observed, the modeling made in this work will be reinforced.

The calculated switching time of the [2]rotaxane molecule in chapter 4 also needs verification. While $t_{shuttle}$ at equilibrium measured experimentally was on the order of 10 seconds, the calculated one yielded only 0.17s. The discrepancy likely came from the underestimation of the barrier height separating the OFF- and ON-state. An independent experimental confirmation would be very useful in further the understanding of the energy landscape of the "shuttling" reaction of the CBPQT-ring. Additionally, the switching time under bias should be characterized experimentally.

Given the slow switching time predicted in chapter 4, the rise time of the signal can be easily measured from a simple oscilloscope setup as shown in figure 6.2. Furthermore, the proposed switching mechanism can be validated experimentally as the shuttling time would strongly depend on the bias applied. Figure 6.3 shows how the calculated energy landscape evolves as the applied bias is increased from 0V to +10V on the silicon bottom electrode. The predicted shuttling times at different biases are listed in table 6.1.

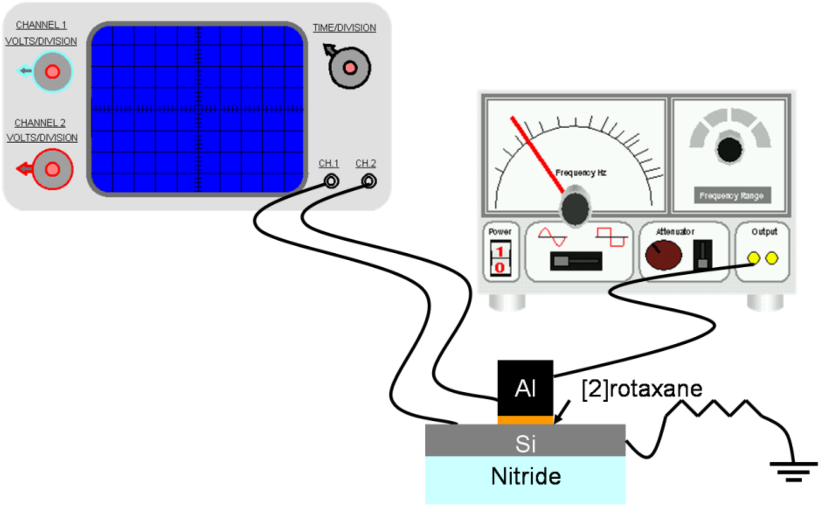

Figure 6.2, oscilloscope setup to measure the rise time of the [2]rotaxane molecule

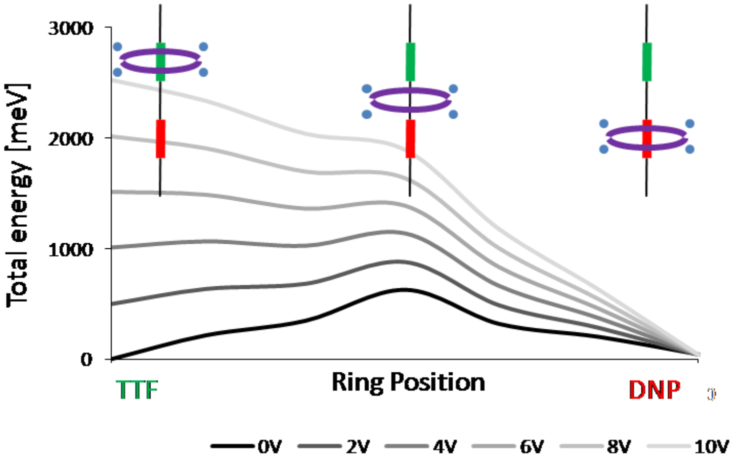

Figure 6.3, energy landscape of the [2]rotaxane molecule as a function of increasing bias

| Applied bias | Shuttling time |
|---|---|
| 0 | 0.17s |
| 2 | 3.7μs |
| 4 | 76ps |
| 6 | 2.3ps |

Table 6.1, shuttling time under different bias

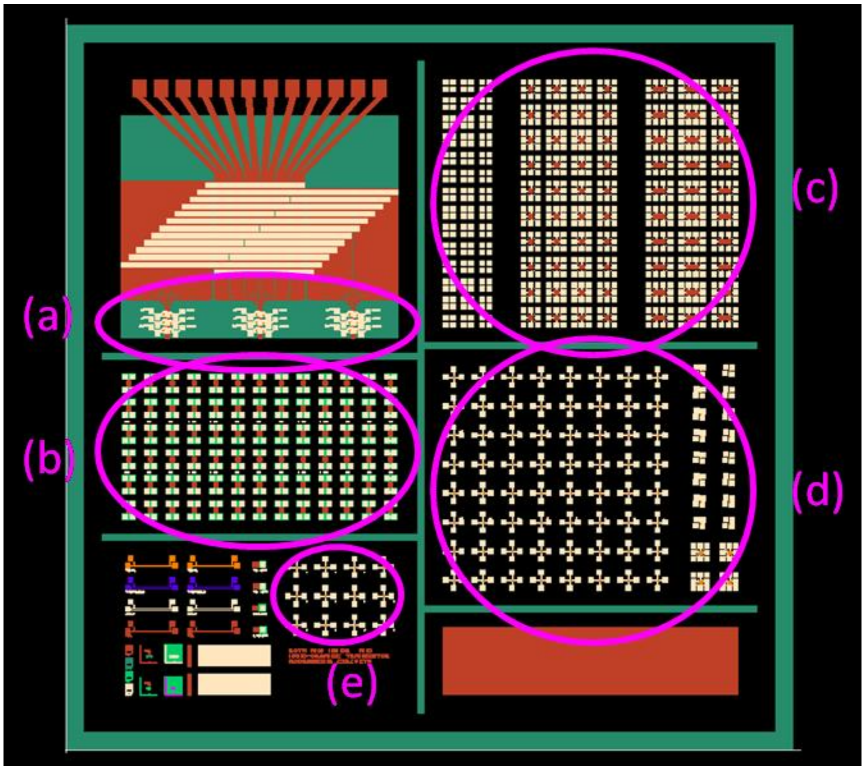

Figure 6.4, a mask layout for characterizing the [2]rotaxane molecular memory. The labeled regions serve different purposes as discussed.

Moreover, the rotaxane memory array requires a more complete characterization. Figure 6.4 shows a mask layout drawn for this purpose. In figure 6.4, region (a) contains 18 8×8 crossbar arrays. Region (b) is consisted of 156 bottom-gated bottom-contact OTFT layouts, with their gate length ranging from 50nm to 5μm. Region (c) has several more test structures with different number of probe pads to allow customized testings. Region (d) is made of structures with multiple lengths of transmissions lines, allowing testing of the RC delay ranging from 1 RC to 4096 RC. And finally in region (e), several test structures are placed for four point probe measurements. With this layout, in addition to the switching time of the arrays of different size, intrinsic resistance, endurance, and cross-talk can be studied. An all-organic memory system can also be realized.

The last suggested future experiment is the synthesis and characterization of the candidate molecules studied in chapter 5. For initial explorations, both experiments and first principles calculations should be carried out in parallel. This allows communications between the experimentalists and the theorists in terms of feasibility, ideas on novel molecules and validations of theoretical claims. Once the simulation work matures, its predictive power should be fully exploited so that the design of a molecule can rely heavily on the computational tool.

### 6.1.2 Theoretical work

With the successful theoretical modeling of the $T_4C_{11}SH$ monolayer in chapter 3 and the estimation of the switching time of the [2]rotaxane molecule in chapter 4, this work has demonstrated the fruitful utility of computational science to organic electronics.

While the main focus has been on molecular systems in general, low cost electronics research is branching out into inorganic materials, for example zinc oxide and metal core nanoparticles. Modeling these interesting systems will yield rewarding information in addition to the existing literature. In particular, as the primitive unit cell of a system as simple as zinc oxide consists of merely two atoms, each calculation computing its ground state property will be finished in hours, if not minutes. Such quick responses are not available to a system as large as those studied in this thesis. Eventually, a system of hundreds or even thousands of atoms comprising an entire nano-structure should be simulated because the properties of a nano-structure are well-known to be different from those of bulk.

The author would also like to perform transport calculations. As an electrical engineer, the author regrets that the short collaboration with theorists in the Molecular Foundry, Lawrence Berkeley National Laboratory, did not allow such calculations to be done. Therefore, a new student continuing this work is strongly encouraged to carry out these calculations. There are a number of systems that may be of mutual interest for both the scientists and the engineers, for example, zinc-oxide nano-structures, monolayers of $T_4C_{18}SH$, organic semiconducting crystals to be proposed in follow-up work of chapter 5 and ultimately the candidate molecules for a single-molecule transistor. All of these examples, except the last, can be investigated both experimentally and theoretically. This will yield a complete characterization of the system. Valuable knowledge and insight not otherwise available can be gained through these combined studies.

## 6.2 Conclusions

In this thesis, a combined experimental and theoretical work investigating nano-scale organic electronics was presented. This included experimental realization of the first dielectric integrated monolayer field effect transistor (DI-mFET), its characterization with grazing incidence X-ray diffraction (GIXD) and modeling from first principles. A careful density functional theory study on the [2]rotaxane molecule was also presented. Lastly, a protocol for predicting edge-to-face (e2f) and face-to-face (f2f) packing of organic molecules was being developed.

In chapter 2, the experimental realization of the first DI-mFET was detailed. This included the process flow for fabrication of a 2-terminal capacitor structure that allowed studying the gate leakage current, and the 3-terminal DI-mFET for field effect measurements. The $I_DV_D$ curve of one of the working DI-mFET was shown, revealing several non-idealities. The concavity observed in the low $V_{DS}$ region suggested a contact barrier. It was argued to have originated from air-gap between the source/drain electrode and the channel. The parasitic resistive path that prevented the channel from turning off was attributed to the presence of charged impurities or contaminants residing on or within the channel. The challenges of the fabrication were outlined, mainly the poor dielectrics and the roughness of the evaporated gold thin film. Several strategies were proposed to get around these problems.

In chapter 3, the monolayer forming the centerpiece of the DI-mFET was characterized with GIXD. The in-plane lattice parameters were extracted from the peak positions. However, due to the lack of higher order peaks, theoretical study was employed to corroborate the experimental findings. The $T_4C_{11}SH$ molecules were shown to pack in the so-called herringbone packing motif. Furthermore, the calculations enriched the physical understanding of this system by explaining the tilting of the molecule with an argument involving competing trends in total energy from the two segments of the molecule. The alkane layer was suggested to be amorphous. Finally, a simulated X-ray diffraction (XRD) pattern matched the experimentally obtained GIXD data. This implied that these atomic coordinates described the monolayer system very well. From this, the positions of several higher order peaks were predicted.

In chapter 4, the thesis shifted its focus to investigate another essential component of the electronics, namely memory. In particular, this work scrutinized the best-case switching performance of the [2]rotaxane memory under the condition described by the previous work. To facilitate this prediction, several important physical properties, including the energy landscape, the ionization potentials and the dielectric constants, were calculated or estimated. The shuttling time of the CBPQT-ring was found to be 3.7μs under a 2V bias, which was much slower than the 7ns RC delay for the 160k-bit array reported. It was commented that this molecule switched slowly comparing to DRAM, a traditional non-volatile memory, and therefore showed only limited application. Additionally, an alternative switching mechanism was proposed.

In chapter 5, a protocol for predicting the packing structure of organic molecules was being developed. Specifically, acenes and their derivatives were tested. Packing the candidate molecules within unit cells based on available literature, the molecule and the cell were computationally relaxed together. While the predictions on tetracene, 5,11-dichlorotetracene and pentacene agreed with experimental results, anthracene and perfluoropentacene did not show a e2f packing motif ground state. Further work was required to address these discrepancies and to refine the method.

Lastly, a number of future works were recommended in this chapter. On the experimental side, in addition to the demonstration of better DI-mFET and the experimental location of predicted higher order peaks, there was a strong emphasis on validating the theoretical claims made in chapter 4. On the theoretical side, besides a refinement of the preliminary results presented in chapter 5, future works were also recommended to focus on other material systems and to study their carrier transport.